Theoretical description of angle-resolved photoemission spectroscopy of low twist angle van der Waals multilayers

Miguel Sá
Mestrado em Física Teórica
Departamento de Física e Astronomia
2021

Orientador
Prof. Dr. Eduardo Castro, Universidade do Porto

Coorientador
Prof. Dr. Bruno Amorim, Universidade do Minho

U.PORTO

FACULDADE DE CIÊNCIAS
UNIVERSIDADE DO PORTO

Todas as correções determinadas pelo júri, e só essas, foram efetuadas.

O Presidente do Júri,

Porto, _____/_____/_____

UNIVERSIDADE DO PORTO

MASTERS THESIS

Theoretical description of angle-resolved photoemission spectroscopy of low twist angle van der Waals multilayers

Author:
Miguel SÁ

Supervisor:
Eduardo CASTRO

Co-supervisor:
Bruno AMORIM

A thesis submitted in fulfilment of the requirements
for the degree of MSc. Theoretical Physics

at the

Faculdade de Ciências da Universidade do Porto
Departamento de Física e Astronomia

March 16, 2022

Acknowledgements

In the year I wrote my thesis, I have become grateful to a lot of people.

First and foremost, I would like to thank my supervisors, Prof. Dr. Eduardo Castro and Prof. Dr. Bruno Amorim. Thank you for all your patience, guidance and dedication. I hope I have met your expectations and have not let you down!

I would also like to thank my friends Bruno Mota, João Silva, José Guilherme and Rafael Almeida, for you were always there to help me, without any hesitation, in any coming trouble I had in my work!

And last, but certainly not least, I would like to thank all my dear friends, but particularly Miguel Barbosa and Ricardo Oliveira, for putting up with me, not only throughout this year, but all our lives, and my family, namely my mom and my dad, who have always loved and supported me. Reluctantly, I also give my thanks to my sister Joana.

UNIVERSIDADE DO PORTO

Abstract

Faculdade de Ciências da Universidade do Porto
Departamento de Física e Astronomia

MSc. Theoretical Physics

Theoretical description of angle-resolved photoemission spectroscopy of low twist angle van der Waals multilayers

by Miguel SÁ

Based on the photoelectric effect, angle-resolved photoemission spectroscopy (ARPES) is an experimental technique that allows to probe the electronic band structure of a given crystalline solid. Very often, however, there is a weak or even inexistent experimental signal where band structure theory predicts energy levels to occur. Such disparity can be traced to a M matrix element, dependent on the experimental configuration, that is present in the theoretical expression for the intensity of the photoemitted beam. This affects the comparison between theory and experiment, and impairs model validation. Building on the previous work of one of us [1], we have developed computational tools to predict the visibility of different energy bands in an ARPES experiment. The method relies on tight-binding models of the electrons, ensuring its computational efficiency. As applications, we study the graphene monolayer, bilayer, and trilayer, AB stacked, the twisted bilayer and trilayer graphene for large, intermediate and small angles, and the molybdenum disulfide (MoS_2), a transition metal dichalcogenide. The product of our work should be helpful in experiments to come, namely in the experimental studies of these van der Waals heterostructures.

UNIVERSIDADE DO PORTO

Resumo

Faculdade de Ciências da Universidade do Porto
Departamento de Física e Astronomia

Mestrado Em Física Teórica

Descrição Teórica de Espectroscopia de Fotoemissão de Ângulo Resolvido em Multicamadas de van der Waals.

por Miguel SÁ

Baseada no efeito fotoelétrico, a espetroscopia de fotoemissão com resolução angular (ARPES) é uma técnica experimental que permite estudar a estrutura eletrónica de um dado sólido cristalino. Contudo, muitas vezes, a experiência mostra um fraco sinal ou até mesmo um sinal nulo em regiões em que a teoria prevê níveis de energia. Tal disparidade advém do elemento da matriz M presente na expressão teórica para a intensidade do feixe fotoemitido. Isto dificulta a comparação entre teoria e experiência, impossibilitando a validação experimental de modelos teóricos. Partindo do trabalho de um dos membros [1], desenvolvemos ferramentas computacionais para prever a visibilidade the diferentes bandas de energias numa experiência de ARPES. O método baseia-se em modelos tight-binding de eletrões, assegurando a sua eficiência computacional. Como aplicações, estudamos a monocamada, bicamada e tricamada de grafeno, em empilhamento AB, a dupla camada e a tripla camada rodada de grafeno para ângulos grandes, intermédios e pequenos, e o dissulfeto de molibdênio (MoS_2), um dicacogeneto metálico. O resultado do nosso trabalho deve ser útil para experiências futuras, nomeadamente em estudos experimentais destas heteroestruturas de van der Waals.

Contents

List of Figures

Chapter 1

Introduction

1.1 Motivation

The field of two-dimensional (2D) materials began in 2004, when Andre Geim and Konstantin Novoselov isolated graphene for the first time, using nothing but graphite and scotch tape [2]. To do so, they placed a graphite flake onto the tape, folded it in two, and then cleaved the flake in half (the scotch tape technique). Repeating this procedure a number of times, to their astonishment, they wound up with pieces that were only one atom thick. Such 2D structures were thought to be thermodynamically unstable, and therefore could not exist [3–5], and yet, through a method so straightforward and accessible that even schoolchildren could probably do it, a material so thin and strong emerged.

However, graphene is only one 2D material. Since then, other such solids, like boron nitride, MoS_2, $NbSe_2$, $Bi_2Sr_2CaCu_2O_x$, came along [6, 7]. The current progress in these 2D crystals isolation [6], and growth [8] leads to a new paradigm of 'complex materials on demand', by first identifying and constructing the key building blocks, and then combining them into complex architectures [9]. Its basic principle is simple: take a monolayer, put it on top of another mono-or few-layer crystal, add another 2D crystal and so on. The resulting stack is an artificial material assembled in a chosen sequence. Strong covalent bonds between in-plane sites, and weak van der Waals-like forces between the layers, are sufficient to keep the stack together [10].

The number of different structures one can obtain by means of this method is practically endless, and their physical properties are generally difficult to predict *a priori*. Nevertheless, by understanding the properties of the 2D components, and how these interact

with each other, one should be able to create materials with specific structural, electronic, optical, mechanical, and other properties, not displayed by the individual layers [9]. This makes van der Waals (vdW) heterostructures very appealing from an application point of view, and worthy of being researched. As examples, transistors based on graphene and hexagonal boron nitride or a semiconducting transition metal dichalcogenide (STMD) [11, 12] and photodetectors based on graphene and a STMD [13, 14] have already been realized.

To study these developments, experimental techniques like the angle-resolved photoemission spectroscopy (ARPES) play a crucial role, by characterizing the electronic degrees of freedom of the materials[15–18]. In a crystal, ARPES is generally understood as a direct probe of the electronic band structure. However, this picture might break down, as the ARPES response is weighted by matrix elements associated with the transition from a crystal bound state to a photoemitted electron state. These matrix elements typically contain a coherent superposition of amplitudes from the different sites in the solid. For bands that are well decoupled from the remaining band structure, though, the matrix elements are featureless, and ARPES can indeed be seen as a direct probe of the band structure [1]. In vdW, where competing periodicities naturally occur due to the lattice mismatch between different layers, a theory capable of predicting the ARPES signal is essential to interpret the data, and to provide a sense of direction in future experiments.

1.2 State Of The Art

Theoretical predictions of ARPES experiments in vdW have been made in the recent years [19–21] for low energy, continuous descriptions of the systems, which are only valid for small misalignment angles.

With the developing research in layered graphene with a twist, a rising interest has been created around these materials. In twisted bilayer graphene (tBLG), the misalignment between layers is responsible for the reduction of the Fermi velocity [22–24] and for the emergence of the van Hove singularities [22–25]. Varying the angle parameter yields different electronic properties, such as conductance [26]. For some very small twist angles, called the magic angles [27, 28], the van Hove singularities coalesce into one, forming a flat band. In this regime, the system shows both a strongly correlated Mott insulating phase [29–31] and superconductivity [32–34].

The flat band regimes have been found as well in twisted trilayer graphene (tTLG) [35–37].

To respond to these demands, there has been research dedicated to predicting the ARPES results of vdW heterostructures, either general [1], using tight-binding models, or graphene-based [38], namely, hexagonal boron nitride and tBLG.

1.3 Objectives

This present thesis has as its primordial objective the theoretical prediction of the results of an ARPES experiment in low twist angle vdW multilayers through the tight-binding method. More specifically, these predictions are aimed at the low angle regimes of the tBLG and the tTLG.

However, it has also other goals such as the theoretical description of the ARPES phenomena, a good review of the models considered and further understanding of the ARPES results and its correct interpretation, not only for these systems, but also for the less complex crystals.

So in general, this thesis aims to make theoretical predictions about the ARPES experimental technique in the low angle vdW multilayers while providing a good exposition of the base concepts that constitute the theory and insightful remarks concerning it.

1.4 Thesis Outline

This thesis is structured as follows: in chapter 2 we introduce ARPES, describing the experimental technique and developing its theory. Using perturbation theory to account for the effects of the incident beam, we reach an expression for the M matrix element. Closing the chapter, we discuss the pedagogical example of the diatomic chain.

In chapter 3 we develop and discuss the studied models. We start with the single layer graphene (SLG), continue to the bilayer graphene (BLG) and trilayer graphene (TLG), discussing their lattices, tight-binding models, band structures and densities of states, (DoS). Then we change from these graphene based systems to the transition metal dichalcogenides (TMDs) for which we also study its lattice, develop the tight-binding Hamiltonian using symmetry principles and discuss the band structure. Finally, we return to the graphene based systems and elaborate on the lattice, tight-binding model and discuss the consequent band structure for tBLG and tTLG. The last is split into large, intermediate

and small angles. To close the chapter, we provide a brief explanation of the used computational methods.

In chapter 4, we study our results for the studied models and further discuss some properties of the ARPES signal for each particular system. For the first graphene based models, a more insightful, yet descriptive, analysis is given, through the use of band structures with superimposed ARPES signal and constant energy plots (CEPs). In the TMDs, we discuss the resulting band structures with ARPES signal and emphasize the importance of the atomic form factor. Finally, we study the tBLG and tTLG systems for large, intermediate, and more importantly, low twist angles, namely the ARPES evolution through the larger angles until the flat band regime.

In chapter 5, we take a general outlook on the overall work, and make our last concluding remarks.

Thereafter, we include some appendices and supporting material, as well as the bibliography.

Chapter 2

Theory of ARPES applied to 2D materials

Angle-resolved photoemission spectroscopy (ARPES) is an experimental technique used to probe the allowed energies and momenta of the electrons in a material. Fundamentally, it is based on the photoelectric effect, where a light beam of frequency ν is directed at the material, exciting and, if the energy permits it, ionizing it. In this last scenario, the ejected electron with energy E_{e^-} is captured by a detector, with a measure of energy and momentum. From these data, we can infer the electron crystalline energy, $E_{\mathbf{k}} = h\nu - E_{e^-}$, and momentum, $\mathbf{k} = \mathbf{q}^{\parallel} - \mathbf{k}_{e^-}^{\parallel}$, where we denote by $\mathbf{q}^{\parallel}$ and $\mathbf{k}_{e^-}^{\parallel}$ the photon and ejected electron parallel to the material's surface momenta components. While the first condition is fairly straightforward and easy to grasp, the second is not so obvious, and we will further discuss it in the sections to come.

Therefore, in this chapter, we derive up to a multiplicative constant the expression for the intensity of the electronic beam when our incident photons have frequency ν. For that, we use time-dependent perturbation theory to model our photon beam as a perturbation, and compute, to first order, the transition rate between the crystalline states and the ejected electrons' final state. From there, it is easy to obtain an expression for the intensity of the electronic beam detected in ARPES. We notice that it depends on these M matrix elements, and that these elements determine how the bands are perceived by the experiment.

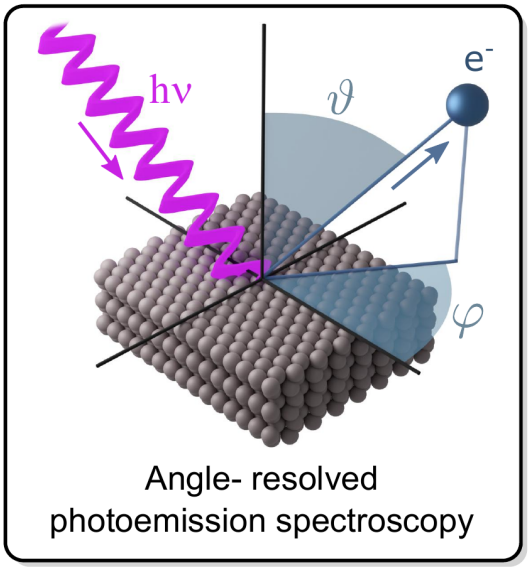

FIGURE 2.1: ARPES experiment scheme. In purple is schematized a photon with energy $h\nu$ that removes the electron from the solid. This free electron acquires a momentum in the direction specified by the angles θ and φ. Figure taken from [39].

2.1 Time-dependent Perturbation Theory

Consider a Hamiltonian H that we split in two terms, an unperturbed part, H_0, and a time-dependent perturbation with magnitude controlled by the parameter $\lambda < 1$,

$$H = H_0 + \lambda V(t). \tag{2.1}$$

Let us also consider a physical state, which we represent by

$$|\psi(t)\rangle = \sum_n c_n(t)\,|n\rangle\,, \tag{2.2}$$

where $\{|n\rangle\}$ are the eigenvalues of the unperturbed Hamiltonian, and $c_n(t)$ is the probability amplitude that the system is in state n at time t. If we know it to be initially in state $|i\rangle$, then we have $c_n(t_0) = \delta_{ni}$.

For very large bases, it is, in general, impossible to compute the exact solution to each coefficient. Therefore, we need to resort to approximated solutions. To accomplish this, we expand the coefficient $c_n(t)$ perturbatively, in a power series of increasing order in the parameter λ,

$$c_n(t) = c_n^{(0)}(t) + c_n^{(1)}(t) + c_n^{(2)}(t) + ..., \tag{2.3}$$

in which $c_n^{(i)}(t)$ is the term of order i, that is, $c_n^{(i)}(t) \propto \lambda^i$.

2.1.1 Dyson Series

Since we are treating a perturbative problem, we are interested in just the lower order terms. To obtain them at a time t, we look to the time evolution operator in the interaction picture, where the operators and kets relate to the usual Schrödinger representation (labeled here by an S) as

$$\left|\psi_I(t)\right\rangle = \mathcal{U}_0^\dagger(t,t_0)\left|\psi_S(t)\right\rangle \qquad A_I(t) = \mathcal{U}_0^\dagger(t,t_0)\, A_S\, \mathcal{U}_0(t,t_0), \tag{2.4}$$

with

$$\mathcal{U}_0(t,t_0) \equiv e^{-iH_0(t-t_0)/\hbar}. \tag{2.5}$$

This operator, as its Schrödinger picture counterpart, evolves to time t a state initially at t_0,

$$\left|\psi_I(t)\right\rangle = \mathcal{U}_I(t,t_0)\left|i\right\rangle. \tag{2.6}$$

Introducing the identity $\sum_n \left|n\right\rangle\left\langle n\right| = \mathbb{I}$ in this last equation yields an expression very alike to the one in equation (2.2),

$$\left|\psi_I(t)\right\rangle = \sum_n \left\langle n\right|\mathcal{U}_I(t,t_0)\left|i\right\rangle\left|n\right\rangle, \tag{2.7}$$

suggesting the identification of its coefficients as

$$c_n(t) = \left\langle n\right|\mathcal{U}_I(t,t_0)\left|i\right\rangle e^{-iE_n(t-t_0)/\hbar}, \tag{2.8}$$

or, to put it more simply,

$$b_n(t) = \left\langle n\right|\mathcal{U}_I(t,0)\left|i\right\rangle, \tag{2.9}$$

where

$$b_n(t) = c_n(t)e^{iE_n(t-t_0)/\hbar}. \tag{2.10}$$

Now, the Schrödinger equation in this picture writes differently,

$$i\hbar\frac{\partial}{\partial t}\left|\psi_I(t)\right\rangle = \lambda V_I(t)\left|\psi_I(t)\right\rangle, \tag{2.11}$$

and can be solved recursively,

$$\begin{aligned}\mathcal{U}_I(t,t_0) &= 1 - \frac{i\lambda}{\hbar}\int_{t_0}^{t} V_I(t')\mathcal{U}_I(t',t_0)dt' \\ &= 1 - \frac{i\lambda}{\hbar}\int_{t_0}^{t} V_I(t')dt' + \left(\frac{i\lambda}{\hbar}\right)^2 \int_{t_0}^{t}\int_{t_0}^{t'} V_I(t')V_I(t'')dt''dt' + \\ &\ldots + \left(\frac{-i\lambda}{\hbar}\right)^n \int_{t_0}^{t}\ldots\int_{t_0}^{t^{(n-1)}} V_I(t')\ldots V_I(t^{(n)})dt\ldots dt^n + \ldots .\end{aligned} \tag{2.12}$$

If we compare equation (2.12) with (2.3), having in mind equations (2.9) and (2.10), we obtain

$$b_n^{(0)}(t) = \delta_{ni}, \tag{2.13a}$$

$$b_n^{(1)}(t) = \frac{-i\lambda}{\hbar}\int_{t_0}^{t} e^{i\omega_{ni}t'}V_{ni}(t')dt' \tag{2.13b}$$

where we made $V_{ni}(t')e^{i\omega_{ni}t'} = \langle n|\, V_I(t')\,|i\rangle$ and $\omega_{ni} = (E_n - E_i)/\hbar$.

2.2 Beam Intensity In ARPES

Our system consists of a translation invariant infinite slab, rested on the xy plane, that is subjected to an outside photon beam, with the purpose of studying its electronic bands. To mimic the photon beam, we use as perturbation the electromagnetic field. More precisely, in the Hamiltonian of equation (2.1), we use the dot product of the vector potential operator and the momentum $\mathbf{p}$ for the perturbed part,

$$\lambda V(t) = -\frac{e}{m_e c}\mathbf{A}\cdot\mathbf{p}. \tag{2.14}$$

The vector potential, we choose to be in the Coulomb gauge, $\nabla\cdot\mathbf{A} = 0$. Considering that our beam can be described by a monochromatic plane wave,

$$\mathbf{A}(\mathbf{x},t) = 2A_0\hat{\boldsymbol{\varepsilon}}\cos\left(\frac{\omega}{c}\hat{\mathbf{n}}\cdot\mathbf{x} - \omega t\right), \tag{2.15}$$

where $\hat{\boldsymbol{\varepsilon}}$ and $\hat{\mathbf{n}}$ are the polarization and propagation directions, respectively, our perturbation can be split in two parts,

$$\lambda V(t) = \mathcal{V}e^{-i\omega t} + \mathcal{V}^\dagger e^{i\omega t}, \tag{2.16}$$

where

$$\mathcal{V} = -\frac{e}{m_e c}A_0 e^{i\mathbf{q}\cdot\mathbf{x}}\hat{\boldsymbol{\varepsilon}}\cdot\mathbf{p} \tag{2.17}$$

and $\mathbf{q} = \omega/c\ \hat{\mathbf{n}}$. Note that the perturbation parameter, λ, is included in the vector potential amplitude, A_0.

Inserting this in equation (2.13b), we have

$$\begin{aligned} b_n^{(1)} &= \frac{-i}{\hbar}\int_0^t (\mathcal{V}_{ni}e^{-i\omega t'} + \mathcal{V}_{ni}^{\dagger}e^{i\omega t'})e^{i\omega_{ni}t'}dt' \\ &= \frac{1}{\hbar}\left[\frac{1-e^{i(\omega_{ni}-\omega)t}}{\omega_{ni}-\omega}\mathcal{V}_{ni} + \frac{1-e^{i(\omega_{ni}+\omega)t}}{\omega_{ni}+\omega}\mathcal{V}_{ni}^{\dagger}\right]. \end{aligned} \tag{2.18}$$

As we see in the next section, these two terms represent two distinct scenarios when we take the limit $t \to +\infty$.

2.2.1 Transition Rate

The probability that the system evolves from an initial state $|i\rangle$, at $t = t_i$, to a final state $|f\rangle$, at $t = t_f$, is

$$P(t_f)_{i\to f} = |c_f(t_f)|^2. \tag{2.19}$$

To compute this absolute value, we use equation (2.18), since $|c_n(t)| = |b_n(t)|$. This is the sum of the first and second terms squared absolute values, that, after integration, yield

$$\frac{1}{\hbar^2}\left|\frac{1-e^{i(\omega_{fi}-\omega)t}}{\omega_{fi}-\omega}\mathcal{V}_{fi}\right|^2 = \frac{4|\mathcal{V}_{fi}|^2}{\hbar^2(\omega_{fi}-\omega)^2}\sin^2\left[\frac{(\omega_{fi}-\omega)}{2}t_f\right], \tag{2.20a}$$

$$\frac{1}{\hbar^2}\left|\frac{1-e^{i(\omega_{fi}+\omega)t}}{\omega_{fi}+\omega}\mathcal{V}_{fi}^{\dagger}\right|^2 = \frac{4|\mathcal{V}_{fi}^{\dagger}|^2}{\hbar^2(\omega_{fi}+\omega)^2}\sin^2\left[\frac{(\omega_{fi}+\omega)}{2}t_f\right] \tag{2.20b}$$

and of an interference term resulting of these terms product.

In the limit $t_f \to +\infty$, due to the result,

$$\lim_{\alpha\to\infty}\frac{1}{\pi}\frac{\sin^2(\alpha x)}{\alpha x^2} = \delta(x), \tag{2.21}$$

two scenarios become appreciable,

$$\begin{cases} \omega_{fi}-\omega \simeq 0 \text{ or } E_f \simeq E_i + \hbar\omega \\ \omega_{fi}+\omega \simeq 0 \text{ or } E_f \simeq E_i - \hbar\omega \end{cases}. \tag{2.22}$$

The first refers to a photon absorption, with frequency ω, and the second to emission. Thus, when one case is relevant, we can neglect the other. In our case, we want to study

absorption though, so we maintain only the term in equation (2.20a), and use it to compute the probability that the system is left in state $|f\rangle$,

$$P(t_f)_{i\to f} = \frac{2\pi}{\hbar} t_f |\mathcal{V}_{fi}|^2 \delta(E_f - E_i - \hbar\omega). \tag{2.23}$$

Differentiating it, we obtain the transition rate from a state $|i\rangle$ to a final state $|f\rangle$,

$$w_{i\to f} \equiv \dot{P}(t_f)_{i\to f} = \frac{2\pi}{\hbar} |\mathcal{V}_{fi}|^2 \delta(E_f - E_i - \hbar\omega). \tag{2.24}$$

2.2.2 Beam Intensity

Up to here, we reached the transition rate of a system initially in the state $|i\rangle$, evolving to a state $|f\rangle$, in equation (2.24). In ARPES though, we know the electron final state when it reaches the detector. What is unknown to us is its electronic state in the material. Therefore, the probability, and transition rate, we have to look for is one that considers the evolution from every state in crystalline states set, Λ, to the final state $|f\rangle$. Since the Λ states are orthogonal, this probability is just the sum of the probabilities of transitioning from a crystal state $n' \in \Lambda$ to the state $|f\rangle$. As the transition rate is the time derivative of the probability, its expression is given by

$$w_{\Lambda\to f} = \sum_{n'\in\Lambda} w_{n'\to f} = \sum_{n'\in\Lambda} \frac{2\pi}{\hbar} |\mathcal{V}_{fn'}|^2 \delta(E_f - E_{n'} - \hbar\omega). \tag{2.25}$$

Now, in order to obtain the ARPES beam intensity, we multiply the transition rate, to which the intensity must be proportional, by the Fermi-Dirac distribution,

$$f(\varepsilon - \mu) = \frac{1}{e^{(\varepsilon-\mu)/k_B T} + 1}. \tag{2.26}$$

By doing this, we establish the weight of electrons with energy $E_{n'}$ (given by the Fermi-Dirac distribution) that is removed and reaches the detector, per unit time (given by the transition rate).

Thus, we end up with an expression for the electronic beam intensity,

$$I_{ARPES}(E_f, \mathbf{x}) \propto \sum_{n'\in\Lambda} f(E_{n'} - \mu) |M_{fn'}|^2 \delta(E_f - E_{n'} - \hbar\omega), \tag{2.27}$$

where μ is the chemical energy, and we wrote $\mathcal{V}_{fn'}$ as the element $M_{fn'}$ of a M matrix. The Dirac delta is assuring energy conservation. In the next section we discuss the M matrix elements.

2.2.3 M Matrix

In equation (2.27), if $|M_{fn'}|^2$ was always a constant, we could probe the material and see every band, for every $\mathbf{k}$. However, that is not the case. On the contrary, the matrix element $M_{fn'}$ is not, in general, constant, and it is inside it that lie the conditions that determine the bands seen in the experiment.

To make further progress, we need to identify what labels these crystalline and final states. The states in the crystal are written as a linear combination of atomic orbitals (LCAO), denoted by α, with coefficient a_α^n, n being the band, and are labeled by their crystal momentum $\mathbf{k}$, as they are Bloch states. Thus, in real space,

$$\psi_{\mathbf{k},n}(\mathbf{x}) = \frac{1}{\sqrt{N}} \sum_{\mathbf{R},\alpha} e^{i\mathbf{k}\cdot(\mathbf{R}+\delta_\alpha)} a_\alpha^n(\mathbf{k}) \phi_\alpha(\mathbf{x}-\mathbf{R}), \tag{2.28}$$

where $\mathbf{R}+\delta_\alpha$ is the orbital α position, and $\phi_\alpha(\mathbf{x}-\mathbf{R})$ is its Wannier function. As our material is a two-dimensional slab, its lattice, reciprocal lattice, and therefore $\mathbf{k}$ points lie also in the plane.

For the removed electron, which we consider our final state, we write its wave function as a plane wave, and label it solely by its momentum, $\mathbf{p}$. Thus, recalling our perturbation in equation (2.17), an element $M_{fn'}$ is of the kind,

$$M_{\mathbf{pk}}^{(n)} = \langle \mathbf{p} | \left(-\frac{eA_0}{m_e c} \int d^3x \, |\mathbf{x}\rangle \, e^{i\mathbf{q}\cdot\mathbf{x}} \hat{\boldsymbol{\varepsilon}} \cdot (-i\hbar\boldsymbol{\nabla}) \, \langle \mathbf{x}| \right) |\psi_{\mathbf{k},n}\rangle \,, \tag{2.29}$$

making $f \to \mathbf{p}$ and $n' \to \mathbf{k}$, expressing M in terms of the energy band n, and inserting the identity $\int d^3x \, |\mathbf{x}\rangle \langle \mathbf{x}| = \mathbb{I}$. (Note that the $\mathbf{x}$ in the exponential refers to a position vector, not an operator as we had before).

We can rearrange the last equation to read

$$M_{\mathbf{pk}}^{(n)} = -\frac{e\hbar A_0 \, \hat{\boldsymbol{\varepsilon}} \cdot \mathbf{p}}{m_e c \sqrt{NV}} \sum_{\mathbf{R},\alpha} e^{i\mathbf{k}\cdot(\mathbf{R}+\delta_\alpha)} e^{-i(\mathbf{p}-\mathbf{q})\cdot(\mathbf{R}+\delta_\alpha)} a_\alpha^n(\mathbf{k}) f_\alpha(\mathbf{q}-\mathbf{p}), \tag{2.30}$$

after making the change of variable $\mathbf{x} \to \mathbf{x} - (\mathbf{R}+\delta_\alpha)$ and defining

$$f_\alpha(\mathbf{p}) = \int d^3x \, \phi_\alpha(\mathbf{x}) e^{-i\mathbf{p}\cdot\mathbf{x}}, \tag{2.31}$$

the atomic form factor. From this expression, we promptly see that the beam intensity depends on alignment between the directions of the emitted electron and vector potential

polarization. Using the results

$$\sum_{\mathbf{R}} e^{i\mathbf{k}\cdot\mathbf{R}} = N\sum_{\mathbf{G}}\delta_{\mathbf{k},\mathbf{G}} \quad \text{and} \quad a^n_\alpha(\mathbf{k}) = e^{i\mathbf{G}\cdot\delta_\alpha}a^n_\alpha(\mathbf{k}+\mathbf{G}) \tag{2.32}$$

where $\mathbf{G}$ is a reciprocal lattice in-plane vector, and splitting the momenta's parallel and perpendicular components, in relation to the material's surface, we can write this last equation as

$$M^{(n)}_{\mathbf{pk}} = -\frac{e\hbar A_0\ \hat{\boldsymbol{\varepsilon}}\cdot\mathbf{p}}{m_e c}\sqrt{\frac{N}{V}}\sum_{\mathbf{G},\alpha} e^{-i(\mathbf{p}^\perp-\mathbf{q}^\perp)\cdot\delta_\alpha}a^n_\alpha(\mathbf{p}^\parallel-\mathbf{q}^\parallel)f_\alpha(\mathbf{p}-\mathbf{q})\delta_{\mathbf{p}^\parallel-\mathbf{q}^\parallel,\mathbf{k}+\mathbf{G}}. \tag{2.33}$$

Since in equation (2.27) we have the squared absolute value, we square the last equation to obtain

$$|M^{(n)}_{\mathbf{pk}}|^2 = \left(\frac{e\hbar A_0\ \hat{\boldsymbol{\varepsilon}}\cdot\mathbf{p}}{m_e c}\right)^2\frac{N}{V}\sum_{\mathbf{G}}\left|\sum_\alpha e^{-i(\mathbf{p}^\perp-\mathbf{q}^\perp)\cdot\delta_\alpha}a^n_\alpha(\mathbf{p}^\parallel-\mathbf{q}^\parallel)f_\alpha(\mathbf{p}-\mathbf{q})\right|^2\delta_{\mathbf{p}^\parallel-\mathbf{q}^\parallel,\mathbf{k}+\mathbf{G}}. \tag{2.34}$$

From the last equation, we see that only free electrons with parallel momentum $\mathbf{p}^\parallel$ differing from the parallel component of the photon beam momentum, $\mathbf{q}^\parallel$, by $\mathbf{k}$, its crystal momentum, and a reciprocal lattice vector, $\mathbf{G}$, contribute to the ARPES visibility.

2.3 A Pedagogical Example: the Monatomic Chain

Before closing this chapter, we approach the simple and yet instructive one-dimensional model of the monatomic chain. Having only an atom per unit cell, the atoms' positions are given by

$$\mathbf{R} = n\mathbf{a} \tag{2.35}$$

where the Bravais vector is

$$\mathbf{a} = a\hat{\mathbf{x}}, \tag{2.36}$$

and $n \in \mathbb{Z}$. Letting $\boldsymbol{\zeta}$ assume the values $\boldsymbol{\zeta} = \mathbf{0}, \pm a\hat{\mathbf{x}}$, the following Hamiltonian sums, at each site $\mathbf{R}$, the onsite energies and the nearest-neighbors hoppings,

$$H = \sum_{\mathbf{R},\boldsymbol{\zeta}} c^\dagger(\mathbf{R})\ t(\boldsymbol{\zeta})\ c(\mathbf{R}+\boldsymbol{\zeta}), \tag{2.37}$$

where $t(\boldsymbol{\zeta})$ is the matrix element $t(\boldsymbol{\zeta}) = \langle\mathbf{R}|\,H\,|\mathbf{R}+\boldsymbol{\zeta}\rangle$. Due to the system translational invariance, this hopping function is expressed only in terms of the distance between atoms

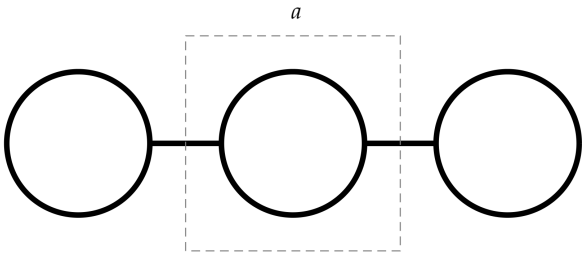

FIGURE 2.2: Monatomic chain scheme with unit cell specification and lattice parameter a.

ζ,

$$t(\zeta) = \begin{cases} \varepsilon \text{ if } \zeta = \mathbf{0} \\ -t \text{ if } \zeta = \pm a\hat{\mathbf{x}} \\ 0 \text{ otherwise,} \end{cases} \tag{2.38}$$

where ε are the onsite energies and $-t$ the nearest-neighbor hoppings.

In reciprocal space, it is simply

$$H = \sum_{\mathbf{k}} c^{\dagger}(\mathbf{k}) t(\mathbf{k}) c(\mathbf{k}), \tag{2.39}$$

with $t(\mathbf{k}) = \sum_{\zeta} e^{i\mathbf{k}\cdot\zeta} t(\zeta)$, meaning the energy is the $\mathbf{k} = k\hat{\mathbf{x}}$ dependent function

$$E(k) = \varepsilon - 2t\cos(ka). \tag{2.40}$$

Since there is just a one-dimensional eigenvalue, there is also only one term being summed inside the absolute value brackets, in equation (2.34), for a single energy band. Having no sites with component perpendicular to the material's surface, and using a Dirac's Delta for the Wannier functions, this term is simply 1. Thus, all spectrum is equally seen by ARPES. In Figure 2.3 we show this, plotting in yellow the energies seen by the experiment.

However, an equally valid parametrization of this system is considering a diatomic chain with the same onsite energies for both orbitals. Making $a \to a/2$ so that the lattice parameter is still a, we now study this system. Its lattice is sketched in Figure 2.4.

In real space, the Hamiltonian is

$$H = \sum_{\mathbf{R},\zeta} \sum_{\alpha,\beta} c_{\alpha}^{\dagger}(\mathbf{R})\; t^{\alpha\beta}(\zeta)\; c_{\beta}(\mathbf{R}+\zeta), \tag{2.41}$$

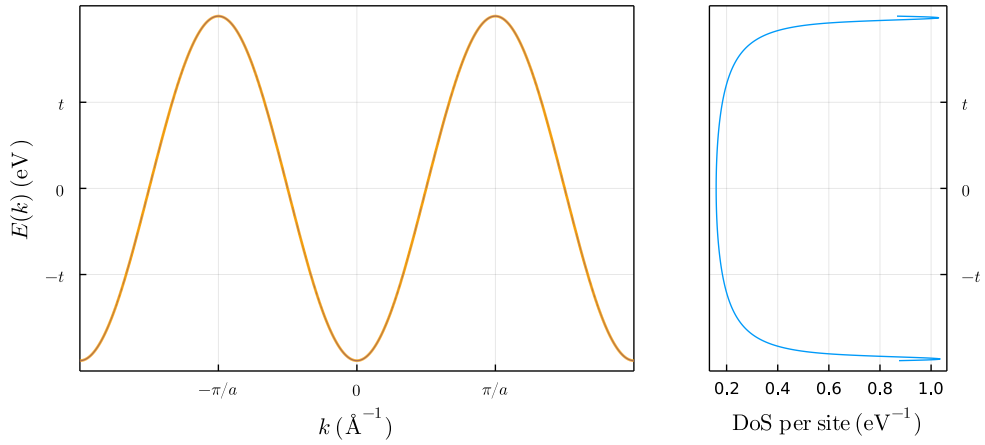

FIGURE 2.3: Monatomic chain's band structure and DoS.

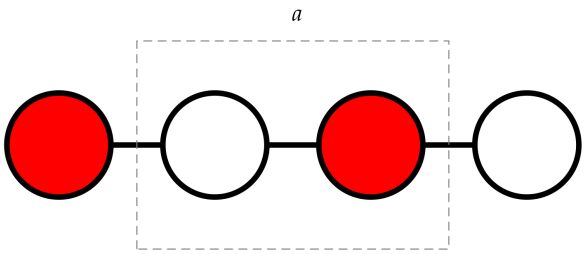

FIGURE 2.4: Diatomic chain scheme with unit cell specification and lattice parameter a.

where now we need to take in consideration the orbitals A and B by summing in α and β. The hopping is the matrix element $t^{\alpha\beta}(\boldsymbol{\zeta}) = \langle \mathbf{R}, \alpha | H | \mathbf{R} + \boldsymbol{\zeta}, \beta \rangle$ given by

$$t^{\alpha\beta}(\boldsymbol{\zeta}) = \begin{cases} \varepsilon\delta_{\alpha\beta} - t(1-\delta_{\alpha\beta}) \text{ if } \boldsymbol{\zeta} = \mathbf{0} \\ -t(1-\delta_{\alpha\beta}) \text{ if } \boldsymbol{\zeta} = \pm a\hat{\mathbf{x}} \\ 0 \text{ otherwise.} \end{cases} \tag{2.42}$$

The reciprocal space Hamiltonian is also very alike, having now a sum in the orbitals as well,

$$H = \sum_{\mathbf{k}} \sum_{\alpha,\beta} c_\alpha^\dagger(\mathbf{k}) t^{\alpha\beta}(\mathbf{k}) c_\beta(\mathbf{k}). \tag{2.43}$$

This yields the dispersion

$$E_\pm(k) = \varepsilon \pm 2t\cos(ka/2). \tag{2.44}$$

Because we have two atoms per unit cell, the dispersion has two energy bands, $\pm$, meaning that for the same k there are two possible energies.

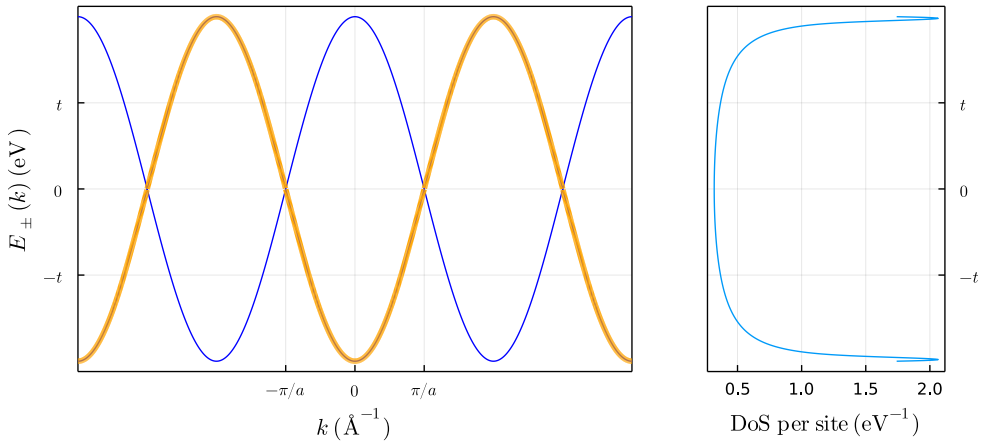

FIGURE 2.5: Diatomic chain's band structure (in blue) and ARPES visibility (in yellow) for symbolic parameters $\varepsilon_A = \varepsilon_B = 0$ eV and DoS.

Nevertheless, the ARPES visibility remains exactly the same. This is seen in Figure 2.5, where in blue are plotted the energy bands and the ARPES visibility is shown in yellow, matching the observed band structure in Figure 2.3. As there are twice many orbitals, the sum in equation (2.34) counts with a sublattice interference and the seen bands alternate between valence and conduction bands, showing the same values for k spaced by $4\pi/a$. This periodicity is determined by the path taken and the relation between the Bloch coefficients,

$$a_\alpha^n(\mathbf{k}) = e^{i\mathbf{G}\cdot\delta_\alpha} a_\alpha^n(\mathbf{k}+\mathbf{G}). \tag{2.45}$$

as seen in Appendix A.

The reason behind the same seen spectrum is because, in truth, the system is the same. The only difference is the approach taken in each case. But, as ARPES is an experimental technique, its results cannot be dependent on our parametrization, and the M matrix elements need to compensate for the larger unit cell.

In the following chapters, we study how this M matrix element behaves in more complex systems.

Chapter 3

Models and Methods

In this chapter the SLG, BLG and TLG are initially considered. For each of them, we present the lattice and develop the tight-binding Hamiltonian. Furthermore, we comment on the consequent band structure and DoS.

Then we present the TMDs. We discuss their lattice and build the tight-binding Hamiltonian, taking advantage of the rotational symmetry and the Slater-Koster parameters (SKp). The resulting bands are plotted for two models, [40, 41], using three set of parameters [40–42], and are compared.

Finally, we develop the tBLG and tTLG systems for commensurate angles, discussing its lattice and tight-binding Hamiltonian, and show the resulting band structures for large, intermediate and small angles.

3.1 Single Layer Graphene

Since 2004, graphene has received extensive research attention due to its fascinating properties, which are still a matter of fundamental studies, [43]. Making our way towards more complex structures, in this brief section, we present its lattice, tight-binding model, and discuss the subsequent band structure and DoS. To that end, we follow [44], using for our model the parameters in [1, 44, 45].

3.1.1 Lattice

Graphene is an isolated two-dimensional, atomically thin sheet of graphite. Its lattice is arranged in a honeycomb structure, with two carbon atoms per unit cell in orbitals A and B, that repeats itself throughout the entirety of the crystal. Its unit cells, shown in

Figure 3.1.1b, sit at lattice points **R**,

$$\mathbf{R} = n_1\mathbf{a}_1 + n_2\mathbf{a}_2, \tag{3.1.1}$$

given by the linear combination of the Bravais vectors,

$$\mathbf{a}_1 = \frac{a}{2}\left(1, \sqrt{3}\right) \tag{3.1.2a}$$

$$\mathbf{a}_2 = \frac{a}{2}\left(-1, \sqrt{3}\right), \tag{3.1.2b}$$

where $a \simeq 2.46$ Å is the lattice parameter, [44]. A depiction of the honeycomb structure and its Bravais vectors is shown in Figure 3.1.1a.

As for the orbitals, while the site A is parametrized by the same vector as its unit cell, for the site B we need to introduce a sublattice vector,

$$\delta = \frac{\mathbf{a}_1 + \mathbf{a}_2}{3}, \tag{3.1.3}$$

as seen in Figure 3.1.1b. Taking this vector absolute value, we see that the carbon-carbon distance is $d = a/\sqrt{3} \simeq 1.42$ Å, [44].

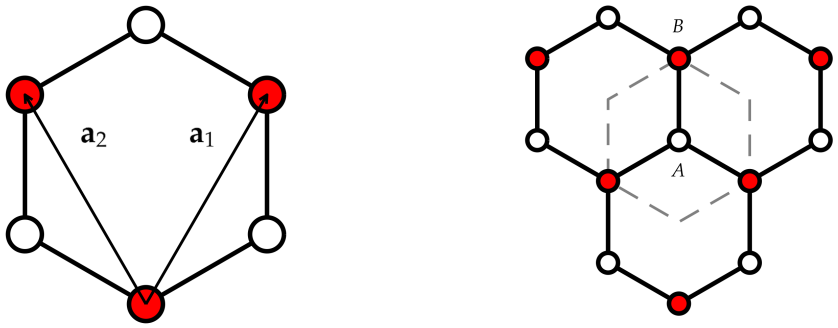

(a) (b)

FIGURE 3.1.1: Graphene honeycomb structure, and Bravais vectors in (a) and Wigner-Seitz unit cell, plotted in gray, with A and B orbitals specification in white and red, respectively, in (b).

Reciprocal Lattice

Graphene's reciprocal lattice is also triangular, as is each lattice composing the honeycomb structure, with basis vectors

$$\mathbf{b}_1 = \frac{2\pi}{3a}\left(1, \sqrt{3}\right) \tag{3.1.4a}$$

$$\mathbf{b}_2 = \frac{2\pi}{3a}\left(-1, \sqrt{3}\right). \tag{3.1.4b}$$

The Brillouin Zone (BZ) is limited according to these, forming a hexagon, rotated 30° in relation to the real space unit cell, as can be seen comparing Figures 3.1.1b and 3.1.2c.

Of particular importance are the two points K and K', at the vertices of the BZ. Their positions are given by

$$\mathbf{K} = \frac{\mathbf{b}_1 - \mathbf{b}_2}{3}, \qquad \mathbf{K}' = -\mathbf{K}, \tag{3.1.5}$$

and the equivalent vectors separated a reciprocal lattice vector.

Besides those, we will also mention the Γ and M points,

$$\mathbf{\Gamma} = \mathbf{0}, \qquad \mathbf{M} = \frac{\mathbf{b}_1}{2}, \tag{3.1.6}$$

in the upcoming plots.

3.1.2 Tight-Binding Model

Of the four valence electrons in a carbon atom, three form σ covalent bonds with the three nearest neighbor atoms in a sp_2 hybridization, [43, 44]. These are represented by the hexagon black lines in Figures 3.1.1a and 3.1.1b. The remaining electron is delocalized in a p_z orbital, traveling through lattice sites, and is responsible for most of the graphene's electronic properties. It is this last electron that we study in the single orbital tight-binding model, [43, 44, 46]. This consists in considering a basis with the isolated atoms' orbitals and positions (in the present case two p_z orbitals at points $\mathbf{R}$), and assuming that the electron's state may be expressed as a linear combination of these orbitals.

Thus, in real space, the second quantization tight-binding Hamiltonian is

$$H_{SLG} = \sum_{\mathbf{R},\boldsymbol{\zeta}} \sum_{\alpha,\beta} c_\alpha^\dagger(\mathbf{R}) t^{\alpha\beta}(\boldsymbol{\zeta}) c_\beta(\mathbf{R}+\boldsymbol{\zeta}), \tag{3.1.7}$$

where we sum over every unit cell at $\mathbf{R}$, its neighbors at $\boldsymbol{\zeta}$, and their orbitals α and β. Furthermore, each term has a hopping, that we write as a function of the distance between sites ($t^{\alpha\beta}(\boldsymbol{\zeta})$ is for two orbitals distanced $\boldsymbol{\delta}_\beta + \boldsymbol{\zeta} - \boldsymbol{\delta}_\alpha$), taking advantage of the translation invariance. For our purposes, though, taking into account only the nearest-neighbors hoppings will suffice, due to the spatial localization of the atomic orbitals functions. The

$t^{\alpha\beta}(\boldsymbol{\zeta})$ hoppings take the form

$$t^{\alpha\beta}(\boldsymbol{\zeta}) = \begin{cases} \varepsilon_{p_z}\delta_{\alpha\beta} - t(1-\delta_{\alpha\beta}) \ \text{ if } \ |\boldsymbol{\zeta}| = 0, \\ -t \ \text{ if } \ |\boldsymbol{\zeta}| = a \ \text{ and } \ |\mathbf{r}_\alpha - \mathbf{r}_\beta| = |\boldsymbol{\delta}| = a/\sqrt{3}, \\ 0 \ \text{ otherwise,} \end{cases} \tag{3.1.8}$$

ε_{p_z} being the orbital energy and $t \simeq 2.7$ eV the hopping parameter, [1, 45]. Inserting this in equation (3.1.7) yields

$$H_{SLG} = \sum_{\mathbf{R}_l,\alpha} c^\dagger_\alpha(\mathbf{R}_l)\varepsilon_{p_z}c_\alpha(\mathbf{R}_l) - \sum_{\mathbf{R}_l,\alpha}\sum_{\boldsymbol{\zeta}} c^\dagger_\alpha(\mathbf{R}_l)\ t\ c_{\bar{\alpha}}(\mathbf{R}_l+\boldsymbol{\zeta}), \tag{3.1.9}$$

where $\bar{\alpha}$ means the orbital that is not α.

In order to diagonalize the Hamiltonian, we make use of Bloch's theorem, yielding a block diagonal matrix,

$$H_{SLG} = \sum_{\mathbf{k}} c^\dagger(\mathbf{k}) H_{\mathbf{k}} c(\mathbf{k}) \tag{3.1.10}$$

where $c^\dagger(\mathbf{k}) = (c^\dagger_A(\mathbf{k}), c^\dagger_B(\mathbf{k}))$ and

$$H_{\mathbf{k}} = \begin{pmatrix} \varepsilon_{p_z} & t^{BA}(\mathbf{k}) \\ t^{AB}(\mathbf{k}) & \varepsilon_{p_z} \end{pmatrix} \tag{3.1.11}$$

where $t^{\alpha\bar{\alpha}}(\mathbf{k}) = -te^{-i\mathbf{k}\cdot(\delta_\alpha - \delta_{\bar{\alpha}})}\sum_{\boldsymbol{\zeta}} e^{i\mathbf{k}\cdot\boldsymbol{\zeta}}$ and, for the matrix to be hermitian, we have $t^{AB}(\mathbf{k}) = t^{BA*}(\mathbf{k})$. Making $\varepsilon_{p_z} = 0$ eV, which we can do since adding a constant to the energy does not change the physics, and evaluating the eigenvalues, we obtain the two-band dispersion

$$E_\pm(\mathbf{k}) = \pm|t^{AB}(\mathbf{k})|. \tag{3.1.12}$$

With the aid of Figure 3.1.2a, we note that the energy spectrum is symmetric around $E_n(\mathbf{k}) = 0$ eV (where the n denotes the energy band). This can be traced to the sublattice symmetry, i.e., $(\psi_A, \psi_B)^T \to (\psi_A, -\psi_B)^T \Rightarrow E_n(\mathbf{k}) \to -E_n(\mathbf{k})$, a property of a tight-binding model coupling only orbitals of the same type.

Also, since we are assuming periodic boundary conditions (PBC), and the number of $\mathbf{k}$ states is given by the number of cells in the crystal, N, [47], for each $\mathbf{k}$ state there are four configurations of spins and bands, there are $4N$ allowed states in the BZ. Since every unit cell contributes with two electrons, only the $2N$ lowest energy levels are filled, i.e., the lower band is completely filled and the upper band empty. Moreover, using Figure 3.1.2b for further insight, we observe that the bands only touch in a set of vectors known as Dirac

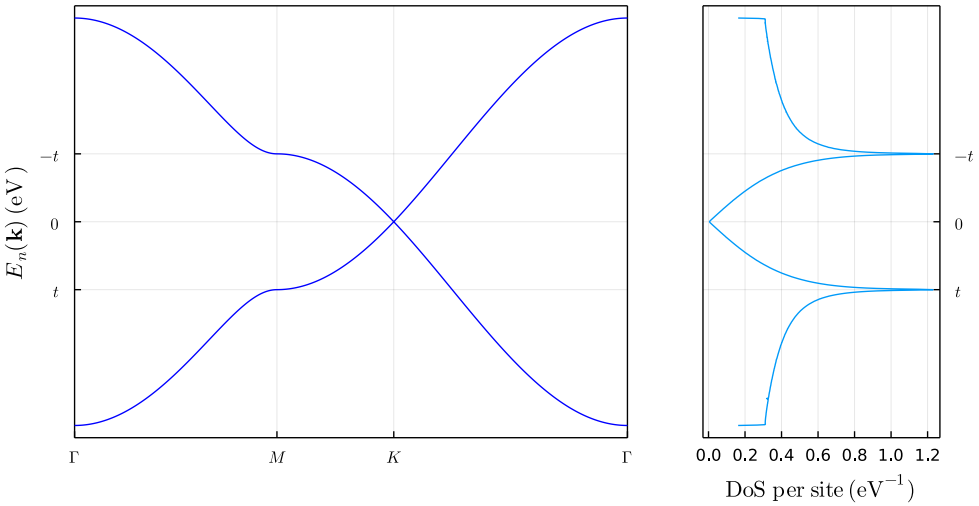

(a)

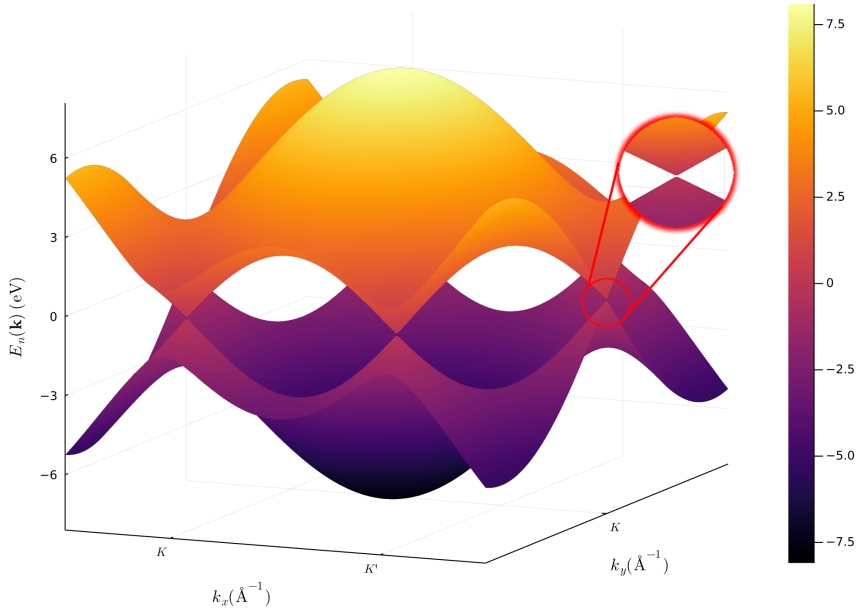

(b)

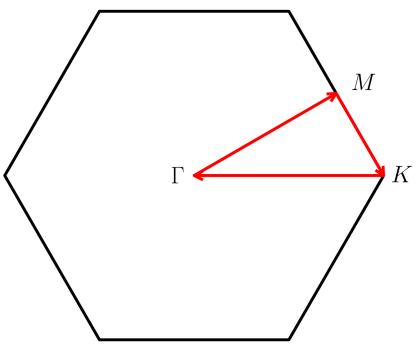

(c)

FIGURE 3.1.2: SLG's band structure along the path $\Gamma - M - K - \Gamma$ for lattice parameter $a = 2.46$ Å, [44], and intralayer hopping parameter $t = -2.7$ eV, [1, 45], in (a), on the left; on the left we plot the respective DoS. In (b) we plot the band structure plot in two dimensions with a close-up, showing the upper and lower bands connecting in the Dirac point. In (c) we show the BZ and the path for which we plot the bands in (a).

points, K and K', represented as the vertices in Figure 3.1.2c. Because the lower band is completely filled, the Fermi surface consists of just these two points. Thus, a bounded electron with energy close to the Fermi energy is easily freed to roam around the lattice with just a small energy boost.

Expanding (3.1.12) near one of these points, we see that its dispersion is linear and that the velocity does not depend on the momentum, in opposition to the usual parabolic case [48],

$$E_n(\mathbf{K}+\mathbf{q}) \simeq \pm\frac{\sqrt{3}ta}{2}|\mathbf{q}|, \tag{3.1.13}$$

having the same kind of energy-momentum relation that we meet in relativistic physics for massless particles, [46]. The velocity at which the excitations propagate is therefore constant, regardless of the crystal momentum, and given by

$$\mathbf{v}_F = \frac{1}{\hbar}\boldsymbol{\nabla}_{\mathbf{k}}E_n(\mathbf{k})\Big|_{\mathbf{k}=\mathbf{K}+\mathbf{q}} \simeq \pm\frac{\sqrt{3}ta}{2\hbar}\hat{\mathbf{q}}, \tag{3.1.14}$$

which, in absolute value, is about 300 times smaller than the speed of light, [46, 48]. Moreover, from the DoS in Figure 3.1.2a, we observe an accumulation of states near M, centered at $\pm t$. This is due to the null energy slope, that shows whenever the velocity goes to zero, and gives rise to the van Hove singularities, [47].

3.2 Bilayer Graphene

Not surprisingly, the BLG shares many features with the monolayer. However, there are some properties that make them distinct. For instance, the low-energy band structure is different; as in the SLG, there is no band gap between valence and conduction bands, but here, the low-energy dispersion is quadratic, and its particles massive, [48]. Another example is the number of van Hove singularities, which is doubled.

In the next section, we explore these differences. For that, we continue closely following the tight-binding approach of [44] and borrowing the parameters from [1, 44, 45].

3.2.1 Lattice

Stacking another graphene sheet atop this one, in such a way that the A orbital of the new layer matches the in-plane position of the B orbital of the former layer, we arrive to a bilayer system disposed in a Bernal stacking (see Figure 3.2.1). As the SLG case, the periodicity of this system is given by the Bravais vectors in equations (3.1.2), and the

Wigner-Seitz unit cell is also the same. However, instead of just two orbitals, here we define four; two for the bottom layer (or layer 1) and two for the top (or layer 2). Thus, we write our orbitals as A_1 and B_1 for the bottom layer and A_2 and B_2 for the top layer. Its sublattice vectors are

$$\boldsymbol{\delta}_{A_1} = \mathbf{0}, \quad \boldsymbol{\delta}_{B_1} = \boldsymbol{\delta}, \quad \boldsymbol{\delta}_{A_2} = \boldsymbol{\delta} + d_\perp \hat{\mathbf{z}} \quad \text{and} \quad \boldsymbol{\delta}_{B_2} = (\boldsymbol{\delta} + d_\perp \hat{\mathbf{z}}) + \boldsymbol{\delta}, \tag{3.2.1}$$

where $d_\perp \simeq 3.35$ Å is the distance between layers, [44].

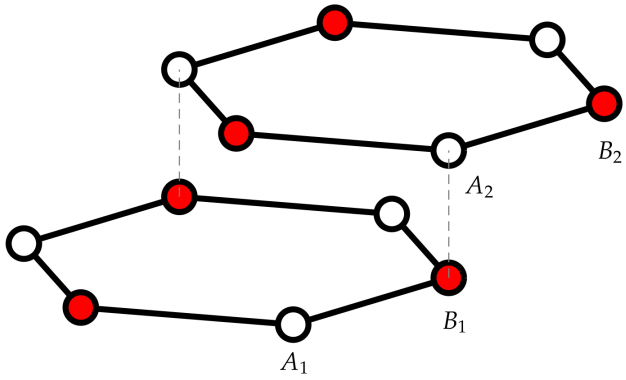

FIGURE 3.2.1: Two graphene layers in a Bernal stacking scheme.

3.2.2 Tight-Binding Model

To account for the above-mentioned composition, one has to consider not only the hoppings in the same graphene sheet, as in SLG, but also the coupling of different layers. Therefore, the Hamiltonian is split in two smaller operators, one referring to the intralayer couplings, and the other to the interlayer couplings,

$$H_{BLG} = H_{intra} + H_{inter}. \tag{3.2.2}$$

The intralayer is, for each layer, the same as the SLG Hamiltonian, studied in the previous section. On the other hand, the interlayer Hamiltonian is

$$H_{inter} = \sum_{\mathbf{R},\boldsymbol{\zeta}_\perp} \sum_{\alpha,\beta} c_\alpha^\dagger(\mathbf{R}) t_\perp^{\alpha\beta}(\boldsymbol{\zeta}_\perp) c_\beta(\mathbf{R} + \boldsymbol{\zeta}_\perp), \tag{3.2.3}$$

and couples both layers, with $\boldsymbol{\zeta}_\perp$ representing the other-layer neighbors, and α and β summing over A_1, B_1, A_2 and B_2.

We will consider two interlayer hopping models:(i) one where only nearest neighbors are coupled, that is B_1 and A_2; and other (ii) where we included more hoppings, which decay with distance.

Nearest Neighbor Interlayer Hoppings

Therefore, considering only hoppings distanced $d_\perp$ in the perpendicular direction, we obtain the following interlayer Hamiltonian,

$$H_{inter} = \sum_{\mathbf{R}} t_\perp \left[c^\dagger_{B_1}(\mathbf{R}) c_{A_2}(\mathbf{R}) + c^\dagger_{A_2}(\mathbf{R}) c_{B_1}(\mathbf{R}) \right], \tag{3.2.4}$$

with $t_\perp \simeq 0.48$ eV, [1, 45], which couples only the sites B_1 and A_2.

In reciprocal space, the block for each $\mathbf{k}$ vector reads

$$H_{BLG} = \sum_{\mathbf{k}} c^\dagger(\mathbf{k}) H_{\mathbf{k}} c(\mathbf{k}), \tag{3.2.5}$$

where

$$H_{\mathbf{k}} = \begin{pmatrix} 0 & t^*(\mathbf{k}) & 0 & 0 \\ t(\mathbf{k}) & 0 & t_\perp(\mathbf{k}) & 0 \\ 0 & t^*_\perp(\mathbf{k}) & 0 & t^*(\mathbf{k}) \\ 0 & 0 & t(\mathbf{k}) & 0 \end{pmatrix}, \tag{3.2.6}$$

and, as before, we took advantage of $t^{A_1B_1}(\mathbf{k}) = t^{A_2B_2}(\mathbf{k}) = t^{B_1A_1*}(\mathbf{k}) = t^{B_2A_2*}(\mathbf{k})$ and $t_\perp^{A_2B_1}(\mathbf{k}) = t_\perp^{B_1A_2*}(\mathbf{k})$, with $t_\perp^{\alpha\beta}(\mathbf{k}) = t_\perp e^{-i\mathbf{k}\cdot(\delta_\alpha - \delta_\beta)} \sum_{\zeta_\perp} e^{i\mathbf{k}\cdot\zeta_\perp}$. Notice that this matrix consists of two SLG Hamiltonians in the diagonal, coupled by $t_\perp(\mathbf{k})$.

The resultant dispersion is

$$E_n(\mathbf{k}) = \begin{cases} \pm\frac{|t_\perp(\mathbf{k})|}{2} + \sqrt{\left(\frac{|t_\perp(\mathbf{k})|}{2}\right)^2 + |t(\mathbf{k})|^2}, \text{ for bands with } E_n(\mathbf{k}) > 0 \\ \pm\frac{|t_\perp(\mathbf{k})|}{2} - \sqrt{\left(\frac{|t_\perp(\mathbf{k})|}{2}\right)^2 + |t(\mathbf{k})|^2} \text{ for bands with } E_n(\mathbf{k}) < 0 \end{cases}, \tag{3.2.7}$$

symmetric about zero energy, as we can see from Figure 3.2.2. Furthermore, at half-filling, the lower energy bands are once again completely filled, and the upper bands empty, as they are joined in the Dirac points, K and K'. The Fermi surface still is just these two points, but the dispersion is no longer linear. Near the Dirac point, for small $\mathbf{q}$, the energy is approximately

$$E_n(\mathbf{K}+\mathbf{q}) \simeq \begin{cases} \pm\frac{9t^2a^2}{2t_\perp}|\mathbf{q}|^2 \\ \pm|t_\perp(\mathbf{k})| \pm \frac{9t^2a^2}{2t_\perp}|\mathbf{q}|^2 \end{cases}, \tag{3.2.8}$$

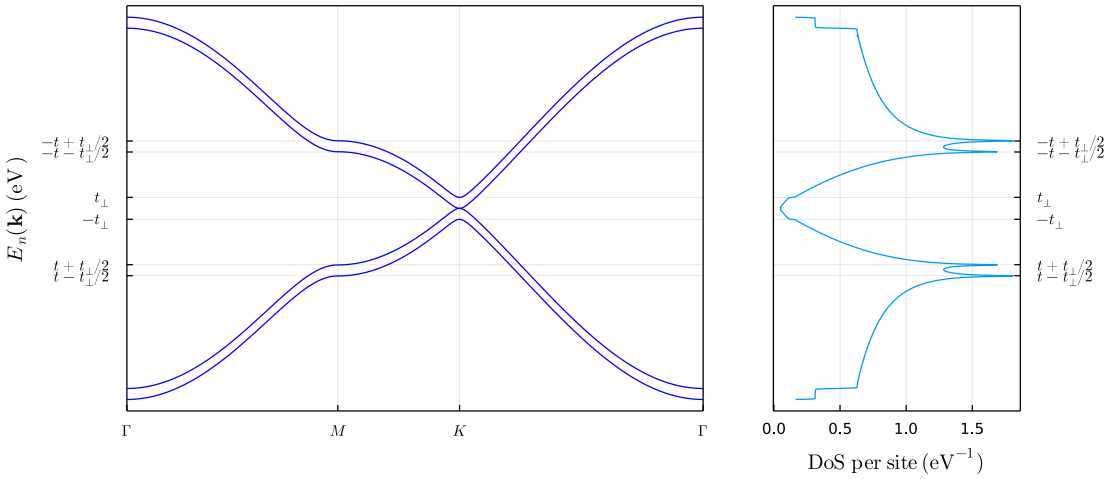

FIGURE 3.2.2: BLG's band structure along the path $\Gamma - M - K - \Gamma$ for lattice parameter $a = 2.46$ Å and layers distanced $d_\perp = 3.35$ Å, [44], intralayer hopping parameter $t = -2.7$ eV, and interlayer hopping parameter $t_\perp = 0.48$, [1, 45] on the left. On the right, we plot the respective DoS.

showing a parabolic relation, contrary to SLG, and linear velocity in $|\mathbf{q}| = |\mathbf{k} - \mathbf{K}|$,

$$\mathbf{v}_F = \frac{1}{\hbar}\boldsymbol{\nabla}_{\mathbf{k}} E_n(\mathbf{k})\Big|_{\mathbf{k}=\mathbf{K}+\mathbf{q}} \simeq \pm\frac{9t^2a^2}{\hbar t_\perp}\mathbf{q}, \tag{3.2.9}$$

characteristic of a free particle with effective mass $m_* = \frac{\hbar^2 t_\perp}{9t^2a^2}$.

Looking at the DoS, we see that now we have not two, but four van Hove singularities, indicating an accumulation of states in the proximity of M, where the velocity goes to zero. These are found centered in $-t \pm t_\perp/2$ for positive energy, and in $t \pm t_\perp/2$ for negative energy. Besides that, we observe an abrupt change in the DoS in $\pm t_\perp$, that may be explained by the presence (or absence) of the outer bands.

In the non-coupling limit, $t_\perp(\mathbf{k}) \to 0$, we recover the SLG profile, where the bands merge into the same degenerate values.

Distance Dependent Interlayer Hopping

Following [44], we adopt a more realistic approach, where the couplings between layers are a function of the distance. In terms of the SKp, the interlayer hopping function is,

$$t_\perp(\mathbf{r}) = \cos^2(\gamma)V_{pp\sigma}(\mathbf{r}) + \sin^2(\gamma)V_{pp\pi}(\mathbf{r}), \tag{3.2.10}$$

with γ being defined as the angle between the z axis and the line connecting both sites,

$$\begin{aligned}\cos(\gamma) &= \frac{d_\perp}{|\mathbf{r}|} \\ \sin(\gamma) &= \frac{\sqrt{|\mathbf{r}|^2 - d_\perp^2}}{|\mathbf{r}|}.\end{aligned} \tag{3.2.11}$$

To model the separation dependence of the SKp, we shall adopt the model explored in [49] and used in [44],

$$\begin{aligned}V_{pp\sigma}(r) &= t_\perp \exp\left[q_\sigma(1 - r/d_\perp)\right] \\ V_{pp\sigma}(r) &= -t \exp\left[q_\pi(1 - r/d)\right],\end{aligned} \tag{3.2.12}$$

in terms of the parameters q_σ and q_π. For q_π, the authors took advantage of $V_{pp\pi}(d) = -t$ and $V_{pp\pi}(a) = -t' = -0.1t$ (the second neighbor hopping, [50]) and obtained

$$\frac{V_{pp\pi}(d)}{V_{pp\pi}(a)} = \frac{t}{t'} \Leftrightarrow q_\pi \simeq 3.15. \tag{3.2.13}$$

The remaining parameter, q_σ, was fixed assuming an equal spatial decay,

$$\frac{q_\pi}{d} = \frac{q_\sigma}{d_\perp} \Leftrightarrow q_\sigma \simeq 7.42. \tag{3.2.14}$$

Diagonalizing the interlayer Hamiltonian, we obtain

$$H_{inter} = \sum_{\mathbf{k}} \sum_{\alpha,\beta} c_\alpha^\dagger(\mathbf{k}) t_\perp^{\alpha\beta}(\mathbf{k}) c_\beta(\mathbf{k}) \tag{3.2.15}$$

with $t_\perp^{\alpha\beta}(\mathbf{k}) = e^{-i\mathbf{k}\cdot(\delta_\alpha - \delta_\beta)} \sum_{\zeta_\perp} t_\perp(\zeta_\perp) e^{i\mathbf{k}\cdot\zeta_\perp}$. Its band structure is plotted in Figure 3.2.3.

The major difference to the simpler prior case is that the symmetry about the zero energy is broken. The upper bands almost superimpose one another as the energy increases, and the lower bands follow the opposite trend. This is because the considered hoppings are not just the first neighbors anymore. Now we are keeping every hopping, but the farther they are, the less impactful they seem (for the purpose of our plots, we imposed a cutoff for the hoppings at distance $\sqrt{d_\perp^2 + 16d^2}$. Notice that we even omit the Hamiltonian matrix in the origin of these bands. When we started considering the second nearest-neighbors, we threw away our chances of a symmetric dispersion. The only way we could avoid this, is by considering only hoppings between A and B orbitals, but due to the nonsensical nature of such a statement for larger distances, we willingly abdicate from the electron-hole.

The non-symmetric band structure inevitably manifests itself in the DoS, in which the

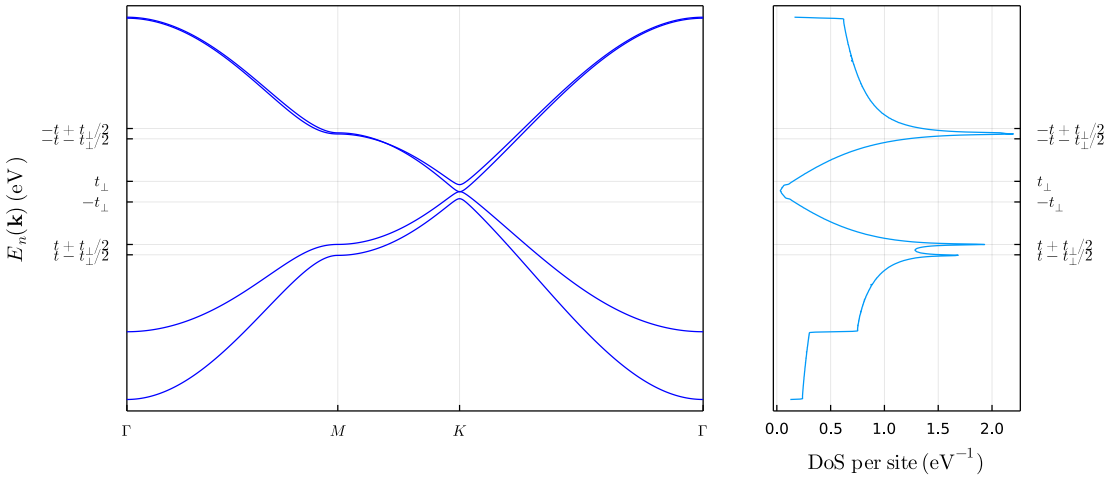

FIGURE 3.2.3: BLG's band structure, without sublattice symmetry, along the path $\Gamma - M - K - \Gamma$ for lattice parameter $a = 2.46$ Å and layers distanced $d_\perp = 3.35$ Å, [44], intralayer hopping parameter $t = -2.7$ eV, and interlayer hopping parameter $t_\perp = 0.48$, [1, 45] on the left. A cutoff in the interlayer hopping was imposed at $\sqrt{d_\perp^2 + 16d^2}$. On the right, we plot the respective DoS.

two positive energy van Hove singularities merge into a much more pronounced one (or at least they get much closer) in $-t$. Nevertheless, for the valence band states the singularities stay roughly in the same place, although the most predominant is now closer to zero.

3.3 Trilayer Graphene

The TLG shows traits of both the SLG and BLG. For instance, its dispersion around the Dirac point demonstrates linear and quadratic slopes, depending on the band, admitting massive and massless particles.

In the section that follows, we study these properties of the TLG building on the treatment of [44] and using the parameters of [1, 44, 45].

3.3.1 Lattice

Stacking yet another layer atop the BLG structure, we reach the TLG system in ABA or Bernal stacking. As we can see in Figure 3.3.1, the B_1 orbital aligns with A_2 that, in turn, aligns with B_3. As the multi-layer before and the SLG, the periodicity is given by the Bravais vectors in equations (3.1.2), sharing the same Wigner-Seitz cell as well. Keeping the two orbitals per sheet, the TLG has six orbitals per unit cell. The positions of the A_1,

B_1, A_2 and B_2 orbitals we discussed already in equation (3.2.1). The third layer's sublattice vectors are

$$\delta_{A_3} = 2d_\perp \hat{\mathbf{z}} \quad \text{and} \quad \delta_{B_3} = \delta + 2d_\perp \hat{\mathbf{z}}. \tag{3.3.1}$$

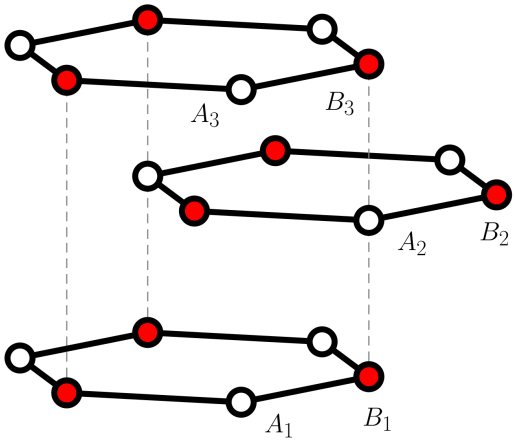

FIGURE 3.3.1: Three graphene layers in a Bernal stacking scheme.

3.3.2 Tight-Binding Model

Once again, the Hamiltonian is split into intralayer and interlayer operators, being the intralayer the SLG Hamiltonian, and the interlayer the one in equation (3.2.2), also summing in the orbitals A_3 and B_3 now.

This interlayer Hamiltonian may again be studied in the same two scenarios above, first the most pedagogical, where we maintain only the nearest-neighbors, directly atop or below the orbitals, and then the more realistic one, where the hoppings are a function of the distance between the orbitals.

Nearest Neighbor Interlayer Hopping

Starting with the most pedagogical case, the interlayer Hamiltonian is

$$H_{inter} = \sum_{\mathbf{R}} t_\perp \left[c^\dagger_{B_1}(\mathbf{R}) c_{A_2}(\mathbf{R}) + c^\dagger_{A_2}(\mathbf{R}) c_{B_1}(\mathbf{R}) + c^\dagger_{A_2}(\mathbf{R}) c_{B_3}(\mathbf{R}) + c^\dagger_{B_3}(\mathbf{R}) c_{A_2}(\mathbf{R}) \right], \tag{3.3.2}$$

coupling just the nearest-neighbors directly atop or below each other, i.e., $B_1 \leftrightarrow A_2$, $A_2 \leftrightarrow B_3$, as we may observe in Figure 3.3.1.

Once diagonalized, in reciprocal space, it writes

$$H_{TLG} = \sum_{\mathbf{k}} c^{\dagger}(\mathbf{k}) H_{\mathbf{k}} c(\mathbf{k}), \tag{3.3.3}$$

where

$$H_{\mathbf{k}} = \begin{pmatrix} 0 & t^*(\mathbf{k}) & 0 & 0 & 0 & 0 \\ t(\mathbf{k}) & 0 & t_\perp(\mathbf{k}) & 0 & 0 & 0 \\ 0 & t_\perp^*(\mathbf{k}) & 0 & t^*(\mathbf{k}) & 0 & t_\perp^*(\mathbf{k}) \\ 0 & 0 & t(\mathbf{k}) & 0 & 0 & 0 \\ 0 & 0 & 0 & 0 & 0 & t^*(\mathbf{k}) \\ 0 & 0 & t_\perp(\mathbf{k}) & 0 & t(\mathbf{k}) & 0 \end{pmatrix}. \tag{3.3.4}$$

As before, in the main diagonal we have three SLG Hamiltonians (one per each layer) coupled by the interlayer hoppings. The intralayer and interlayer hoppings are again all equivalent.

The energy eigenvalues, for a single $\mathbf{k}$, are six,

$$E_n(\mathbf{k}) = \begin{cases} \pm\frac{\sqrt{2}|t_\perp(\mathbf{k})|}{2} + \sqrt{\frac{|t_\perp(\mathbf{k})|^2}{2} + |t(\mathbf{k})|^2}, \text{ for the higher bands with } E_n(\mathbf{k}) > 0 \\ \pm\frac{\sqrt{2}|t_\perp(\mathbf{k})|}{2} - \sqrt{\frac{|t_\perp(\mathbf{k})|^2}{2} + |t(\mathbf{k})|^2}, \text{ for lower bands with } E_n(\mathbf{k}) < 0 \\ \pm|t(\mathbf{k})| \text{ for the remaining, more central bands} \end{cases}. \tag{3.3.5}$$

The band structure is represented in Figure 3.3.2, along the path $\Gamma - M - K - \Gamma$, where we observe the return of the symmetry around 0. The Fermi surface is again in the K and K' points, where the bands meet in linear and parabolic fashions, joining both SLG and BLG dispersions. This is clear when we expand around $\mathbf{K}$. Due to the dispersion's similarity with the SLG and BLG, we are able to rewrite $|t_\perp| \to \sqrt{2}|t_\perp|$, and use the prior results. Thus, for small $|\mathbf{q}|$, we have,

$$E_n(\mathbf{K}+\mathbf{q}) \simeq \begin{cases} \pm\frac{9t^2a^2}{\sqrt{2}t_\perp}|\mathbf{q}|^2 \\ \pm|t_\perp(\mathbf{k})| \pm \frac{9t^2a^2}{\sqrt{2}t_\perp}|\mathbf{q}|^2 \\ \pm\frac{\sqrt{3}ta}{2}|\mathbf{q}| \end{cases}, \tag{3.3.6}$$

confirming the slopes claimed before. The same can be said for the velocity near these points,

$$\mathbf{v}_F = \frac{1}{\hbar}\nabla_{\mathbf{k}} E_n(\mathbf{k})\Big|_{\mathbf{k}=\mathbf{K}+\mathbf{q}} \simeq \begin{cases} \pm\frac{\sqrt{3}ta}{2\hbar}\hat{\mathbf{q}} \\ \pm\frac{9t^2a^2}{\sqrt{2}\hbar t_\perp}\mathbf{q} \end{cases}, \tag{3.3.7}$$

where the constant velocities are respective to the linear bands and the linear velocities to the parabolic bands. Thus, the TLG has both massless and massive particles, of mass $m_* = \frac{\sqrt{2}\hbar^2 t_\perp}{9t^2a^2}$.

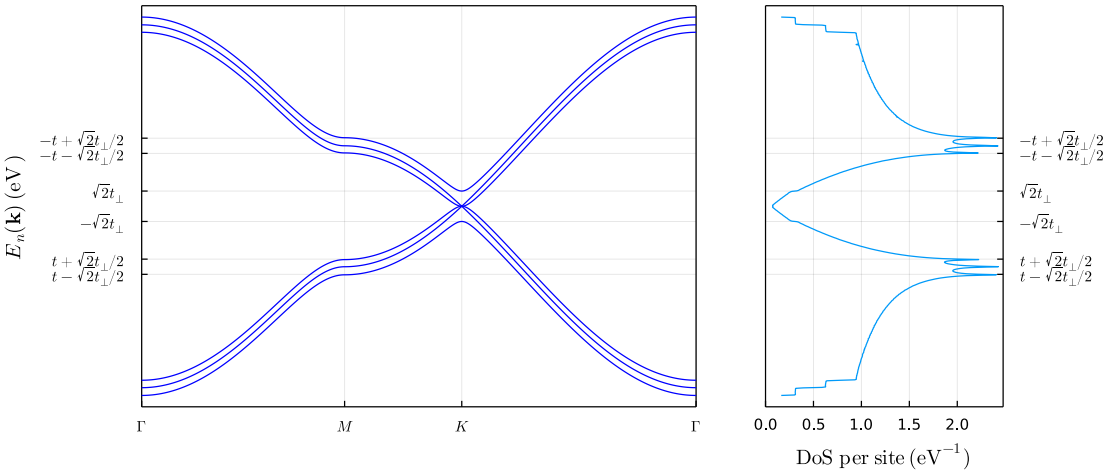

FIGURE 3.3.2: TLG's band structure along the path $\Gamma - M - K - \Gamma$ for lattice parameter $a = 2.46$ Å and layers distanced $d_\perp = 3.35$ Å, [44], intralayer hopping parameter $t = -2.7$ eV, and interlayer hopping parameter $t_\perp = 0.48$, [1, 45] on the left. On the right, we plot the respective DoS.

The DoS looks like a superposition of the SLG and BLG densities, having three van Hove singularities at $\pm t$, $\pm t + \sqrt{2}t_\perp/2$ and $\pm t - \sqrt{2}t_\perp/2$, which are the same places as the prior individual cases, if we remember to make $|t_\perp| \to \sqrt{2}|t_\perp|$. Moreover, around $\pm\sqrt{2}t_\perp$ there is an abrupt change in the DoS, that is explained by the presence (or absence) of the outer bands. Between these energies, the DoS seem linear, having, nevertheless, the contribution of the parabolic bands as well.

Distance Dependent Interlayer Hopping

As before, now we discuss and stick with the more realistic scenario, in which the hoppings are functions of a distance. With this condition, the energy symmetry is out of the window, as seen in Figure 3.3.3. Once again, the positive energy bands seem to superimpose with each other, while the negative bands diverge from one another.

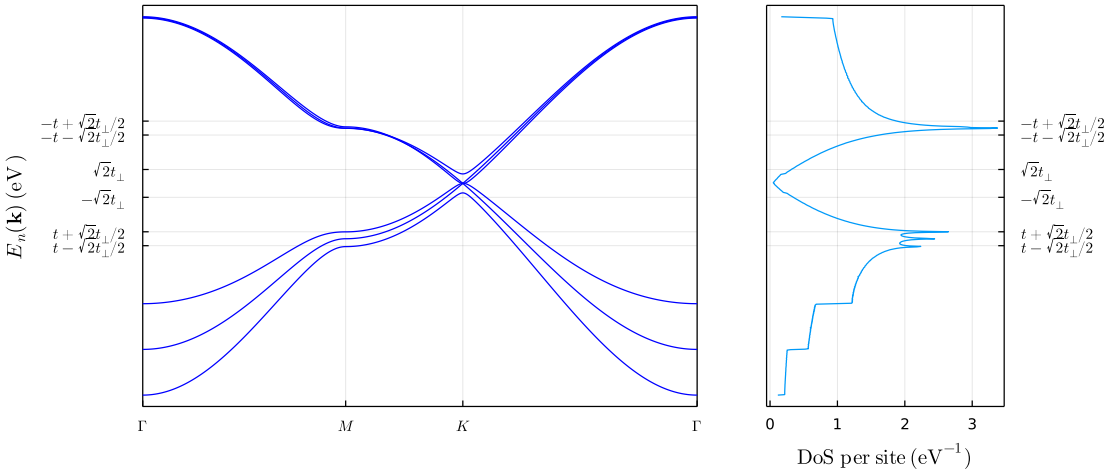

FIGURE 3.3.3: TLG's band structure, without sublattice symmetry, along the path $\Gamma - M - K - \Gamma$ for lattice parameter $a = 2.46$ Å and layers distanced $d_\perp = 3.35$ Å, [44], intralayer hopping parameter $t = -2.7$ eV, and interlayer hopping parameter $t_\perp = 0.48$, [1, 45] on the left. A cutoff in the interlayer hopping was imposed at $\sqrt{d_\perp^2 + 16d^2}$. On the right, we plot the respective DoS.

The DoS seemingly has only four singularities, but, as discussed in the previous section, three are tightly compacted in $-t$, while the remaining three maintain their energies.

3.4 Transition Metal Dichalcogenide Monolayers

The study of two-dimensional materials was greatly propelled by the successful isolation of graphene. Even so, its gapless band structure can be inconvenient to certain applications to electronic devices. On the opposite hand, layered transition metal dichalcogenides (TMDs), with chemical formula MX_2, are semiconductors with direct or indirect band gaps dependent on the number of layers and in the range of visible light (1-2eV), [41]. Such materials also display phenomena as superconductivity, [51], magnetism, [52], charge density waves (in TaS_2) observed by experiment, [53, 54], and topological insulator phases predicted by theory, [55, 56]. When isolated in monolayers, they show phenomena as optical control of valley degrees of freedom enabled by the broken inversion symmetry, [57], and can be combined with other materials to fabricate hetero structures with tailored properties, [58].

In order to address this more complex phenomena, it is crucial to have an understanding of its building blocks. That is why in this section we study the TMD monolayer. Taking the case of molybdenum disulfide, MoS_2, we build a Hamiltonian for 11 orbitals, using the system symmetry and the SKp to mimic each bond.

3.4.1 Lattice

Just like graphene, MoS_2 is arranged in a honeycomb structure, with the Bravais vectors

$$\begin{aligned} \mathbf{a}_1 &= \frac{a}{2}\left(1, \sqrt{3}\right) \\ \mathbf{a}_2 &= \frac{a}{2}\left(-1, \sqrt{3}\right). \end{aligned} \tag{3.4.1}$$

Its sublattices are composed of a triangular lattice with the Mo atoms, sandwiched between two other symmetric triangular lattices, with the S atoms, as shown in Figures 3.4.1a and 3.4.1b. Also, instead of a p_z orbital in each site as before, 5 d-orbitals sit in the Mo sites, d_{z^2}, $d_{x^2-z^2}$, d_{xy}, d_{xz} and d_{yz}, and 6 p-orbitals in the S sites, p_x, p_y, p_z, three in each layer. The same-type nearest neighbor is parameterized by

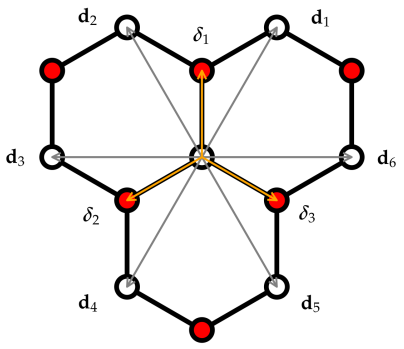

(a)

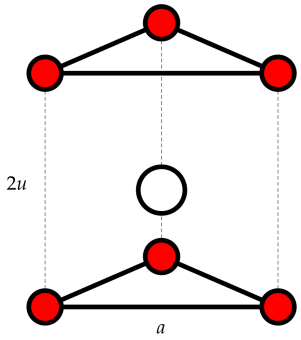

(b)

FIGURE 3.4.1: Lattice structure of MoS_2 in (a) viewed from a top perspective and from a side view perspective in (b). White circles indicate Mo atoms and red circles S atoms. In (a) we also show the vectors for the neighbors with considered hoppings.

$$\mathbf{d}_n = a\left(\cos\left(\frac{n\pi}{3}\right), \sin\left(\frac{n\pi}{3}\right)\right) \tag{3.4.2}$$

with $n = 1, 2, ..., 6$, since there are six equally spaced neighbors around each atom. On the other hand, for different-type nearest neighbors, we write the position vectors as

$$\delta_{n,s} = \frac{a}{\sqrt{3}}\left(\cos\left(\frac{2n\pi}{3} - \frac{\pi}{6}\right), \sin\left(\frac{2n\pi}{3} - \frac{\pi}{6}\right), s\frac{\sqrt{3}u}{a}\right) \tag{3.4.3}$$

in relation to the Mo atom, where $u = 1.586$ Å $\simeq a/2$ is the layers' height, n ranges from $n = 1, 2, 3$, since there are only three neighbors of this type, and $s = \pm 1$, $+$ for the top layer and $-$ for the bottom. Writing the Mo atoms position vectors in the S referential is

equivalent, and these vectors are

$$\boldsymbol{\tau}_{n,s} = \frac{a}{\sqrt{3}}\left(\cos\left(\frac{2n\pi}{3}+\frac{\pi}{6}\right), \sin\left(\frac{2n\pi}{3}+\frac{\pi}{6}\right), -s\frac{\sqrt{3}u}{a}\right). \tag{3.4.4}$$

This can also be written as

$$\begin{aligned}\boldsymbol{\delta}_{n,s} &= b\left(\cos\left(\frac{2n\pi}{3}-\frac{\pi}{6}\right)\cos(\phi), \sin\left(\frac{2n\pi}{3}-\frac{\pi}{6}\right)\cos(\phi), s\,\sin(\phi)\right)\\ \boldsymbol{\tau}_{n,s} &= b\left(\cos\left(\frac{2n\pi}{3}+\frac{\pi}{6}\right)\cos(\phi), \sin\left(\frac{2n\pi}{3}+\frac{\pi}{6}\right)\cos(\phi), -s\,\sin(\phi)\right),\end{aligned} \tag{3.4.5}$$

if we define $b = \sqrt{a^2/3+u^2}$ and $\phi = \arctan\left(\sqrt{3}u/a\right)$.

3.4.2 Tight-Binding Model

We now build our tight-binding Hamiltonian, splitting the Hamiltonian in smaller Hamiltonians that couple only one neighbor,

$$H = H_0 + H_{\text{S-S}}^{interlayer} + \sum_m^6 \left(H_{\text{Mo-Mo}}^{(m)} + H_{\text{S-S}}^{(m)}\right) + \sum_n^3 \left(H_{\text{Mo-S}}^{(n)} + H_{\text{S-Mo}}^{(n)}\right). \tag{3.4.6}$$

In the last equation, H_0 is the Hamiltonian with the information regarding the crystal field, and $H_{\text{S-S}}^{interlayer}$ the hoppings between layers of S. The $H_{\text{Mo-Mo}}^{(m)}$ and $H_{\text{S-S}}^{(m)}$ Hamiltonians couple the m-th same-type neighbor, with vector $\mathbf{d}_m$, and $H_{\text{Mo-S}}^{(n)}$ and $H_{\text{S-Mo}}^{(n)}$ couple the n-th different-type neighbor, with vector δ_n. These last four sum up to 6 (the first two) and 3 (the last two), since these are the number of such neighbors, as we gather from Figure 3.4.1a. To write these explicitly, we do as mentioned above, and take advantage of the system symmetry; it has rotational invariance for the angles given by $2\pi\mathbb{Z}/3$ around z. Analytically, this amounts to defining a rotation, R_θ, and two reference frames, $\mathcal{O}$ and $\mathcal{O}'$, such that $\mathcal{O}' = R_\theta : \mathcal{O}$. Therefore, a creation operator in both frames is related by

$$c_\alpha^{\mathcal{O}'\dagger}(\mathbf{R}) = \sum_\beta (\mathcal{D}_\theta^{-1})^{\beta\alpha}\, c_\beta^{\mathcal{O}\dagger}(R_\theta : \mathbf{R}), \tag{3.4.7}$$

where $\mathbf{R}$ is a position vector and α and β are the orbitals. $\mathcal{D}_\theta$ is a unitary rotation matrix in the angular momentum representation that transforms $|\alpha\rangle_{\mathcal{O}'} = \mathcal{D}_\theta^{-1}|\alpha\rangle_{\mathcal{O}}$, with elements $(\mathcal{D}_\theta^{-1})^{\beta\alpha} = {}_{\mathcal{O}}\langle\beta|\alpha\rangle_{\mathcal{O}'} = {}_{\mathcal{O}}\langle\beta|\mathcal{D}_\theta^{-1}|\alpha\rangle_{\mathcal{O}}$, where the subscript indicates the state ket's frame.

Due to the symmetry, a hopping function is the same, in both frames, for the same vector $\boldsymbol{\zeta}$, $t^{\alpha\beta}_{\mathcal{O}}(\boldsymbol{\zeta}) = t^{\alpha\beta}_{\mathcal{O}'}(\boldsymbol{\zeta})$. Thus, for the generic bond A-B, we can write

$$\begin{aligned} H_{\text{A-B}} &= \sum_{\mathbf{R},\boldsymbol{\zeta}} \sum_{\mu\nu} c^{\mathcal{O}'\dagger}_{\mu}(\mathbf{R}) t^{\mu\nu}_{\mathcal{O}'}(\boldsymbol{\zeta}) c^{\mathcal{O}'}_{\nu}(\mathbf{R}+\boldsymbol{\zeta}) \\ &= \sum_{\mathbf{R},\boldsymbol{\zeta}} \sum_{\alpha\beta} c^{\mathcal{O}\dagger}_{\alpha}(R_\theta : \mathbf{R}) \left(\sum_{\mu,\nu} \left(\mathcal{D}^{-1}_{\theta}\right)^{\alpha\mu} t^{\mu\nu}_{\mathcal{O}}(\boldsymbol{\zeta}) \mathcal{D}^{\nu\beta}_{\theta} \right) c^{\mathcal{O}}_{\beta}(R_\theta : (\mathbf{R}+\boldsymbol{\zeta})) \\ &= \sum_{\mathbf{R},\boldsymbol{\zeta}} \sum_{\alpha\beta} c^{\mathcal{O}\dagger}_{\alpha}(\mathbf{R}) \left(\sum_{\mu,\nu} \left(\mathcal{D}^{-1}_{\theta}\right)^{\alpha\mu} t^{\mu\nu}_{\mathcal{O}}(R^{-1}_\theta : \boldsymbol{\zeta}) \mathcal{D}^{\nu\beta}_{\theta} \right) c^{\mathcal{O}}_{\beta}(\mathbf{R}+\boldsymbol{\zeta}), \end{aligned} \tag{3.4.8}$$

concluding from the last term in parentheses

$$t_{\mathcal{O}}(R_\theta : \boldsymbol{\zeta}) = \mathcal{D}^{-1}_{\theta} t_{\mathcal{O}}(\boldsymbol{\zeta}) \mathcal{D}_{\theta}, \tag{3.4.9}$$

where we discard the superscripts since we are now referring to the whole matrices. Because we are only considering a bond A-B, the sum in $\boldsymbol{\zeta}$ is along vectors of same length. Therefore, we can sum in the angle instead. Fixing a neighbor with vector $\boldsymbol{\zeta}^*$ and using equation (3.4.9) we have,

$$H_{\text{A-B}} = \sum_{\mathbf{R},\theta} \sum_{\alpha,\beta} c^{\mathcal{O}\dagger}_{\alpha}(\mathbf{R}) \left(\mathcal{D}^{-1}_{\theta} t_{\mathcal{O}}(\boldsymbol{\zeta}^*) \mathcal{D}_{\theta} \right)^{\alpha\beta} c^{\mathcal{O}}_{\beta}(\mathbf{R} + R_\theta : \boldsymbol{\zeta}^*). \tag{3.4.10}$$

Therefore, we can build the entire Hamiltonian for the bond A-B using just the hopping from one neighbor. To yield the band structure, we still have to write this Hamiltonian in

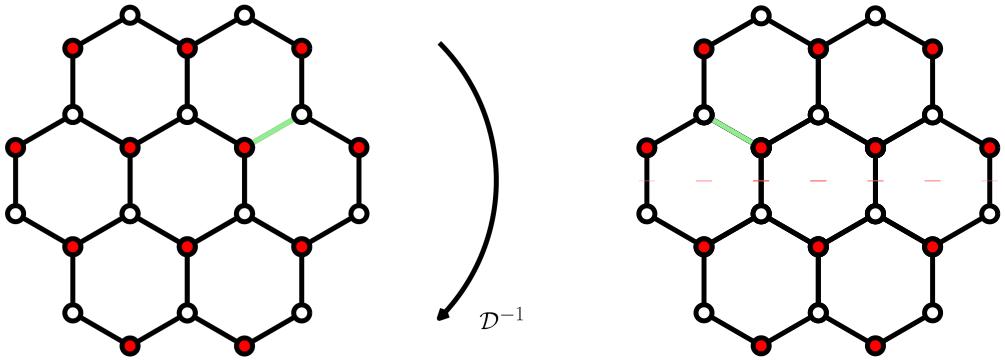

(a) (b)

FIGURE 3.4.2: Reference frame's rotation from $\mathcal{O}$ to $\mathcal{O}'$. In green, we represent a bond between the same two atoms in both frames.

the reciprocal space,

$$H_{\text{A-B}} = \sum_{\mathbf{k}} \sum_{\alpha,\beta} c^{\mathcal{O}\dagger}_{\alpha}(\mathbf{k}) t^{\alpha\beta}_{\mathcal{O}}(\mathbf{k}) c^{\mathcal{O}}_{\beta}(\mathbf{k}), \tag{3.4.11}$$

where

$$t_{\mathcal{O}}^{\alpha\beta}(\mathbf{k}) = e^{-i\mathbf{k}\cdot(\delta_\alpha - \delta_\beta)} \sum_{\theta} e^{i\mathbf{k}\cdot R_\theta : \zeta^*} \left(\mathcal{D}_\theta^{-1} t_{\mathcal{O}}(\zeta^*) \mathcal{D}_\theta \right)^{\alpha\beta} \tag{3.4.12}$$

is the hopping function in $\mathbf{k}$-space in terms of a fixed vector ζ^*.

Before setting all this artillery in motion, we make one last rotation to align the bonds with the z axis of a new locally adapted frame, $\mathcal{O}''$. For this, we use the result in equation (3.4.9), but this time without the symmetry advantages, obtaining the weaker relation,

$$t_{\mathcal{O}}(\zeta^*) = \mathcal{D}_\theta^{-1} t_{\mathcal{O}''}(R_\theta^{-1} : \zeta^*) \mathcal{D}_\theta. \tag{3.4.13}$$

Thus, we write the final hopping matrix as

$$t_{\mathcal{O}}(R_{\theta_z} : \zeta^*) = \mathcal{D}_z(-\theta_z)\mathcal{D}_x(-\theta_x) t_{\mathcal{O}''}(R_{\theta_x}^{-1} : \zeta^*) \mathcal{D}_x(\theta_x)\mathcal{D}_z(\theta_z), \tag{3.4.14}$$

using a slightly more cumbersome notation that, while unnecessary for the general description provided above, is convenient for the following section. With it, we specify the rotation axis in the subscript, and the angle as argument. We also use the fact that $\mathcal{D}^{-1}(\theta) = \mathcal{D}(-\theta)$.

3.4.3 Slater-Koster Approach

The SKp aim to bypass the computation of the difficult integrals one comes across when putting together the Hamiltonian, [59]. In this section, we resort to the parameters in Table 3.4.1, given by [40, 42], to model our Hamiltonians. These SKp aim to describe the covalent bonds between atoms. We consider the σ bonds, represented in Figures 3.4.3b and 3.4.3d, where both orbitals are aligned with each other, the π and the δ bonds, in Figures 3.4.3a, 3.4.3c and 3.4.3e and 3.4.3f respectively, where the coupling is lateral. With the π bonds, the electron wave functions deviate from zero in just one direction from the molecular axis, while with the δ bonds this happens in four directions.

In the next sections, we show the specifics of the Hamiltonian building, based on the rotations described in the previous section. The matrices that follow are expressed in the basis

$$c^\dagger = \{c^\dagger_{p_{x,b}}, c^\dagger_{p_{x,t}}, c^\dagger_{p_{y,b}}, c^\dagger_{p_{y,t}}, c^\dagger_{p_{z,b}}, c^\dagger_{p_{z,t}}, c^\dagger_{d_{xy}}, c^\dagger_{d_{xz}}, c^\dagger_{d_{yz}}, c^\dagger_{d_{x^2-y^2}}, c^\dagger_{d_{z^2}}\}. \tag{3.4.15}$$

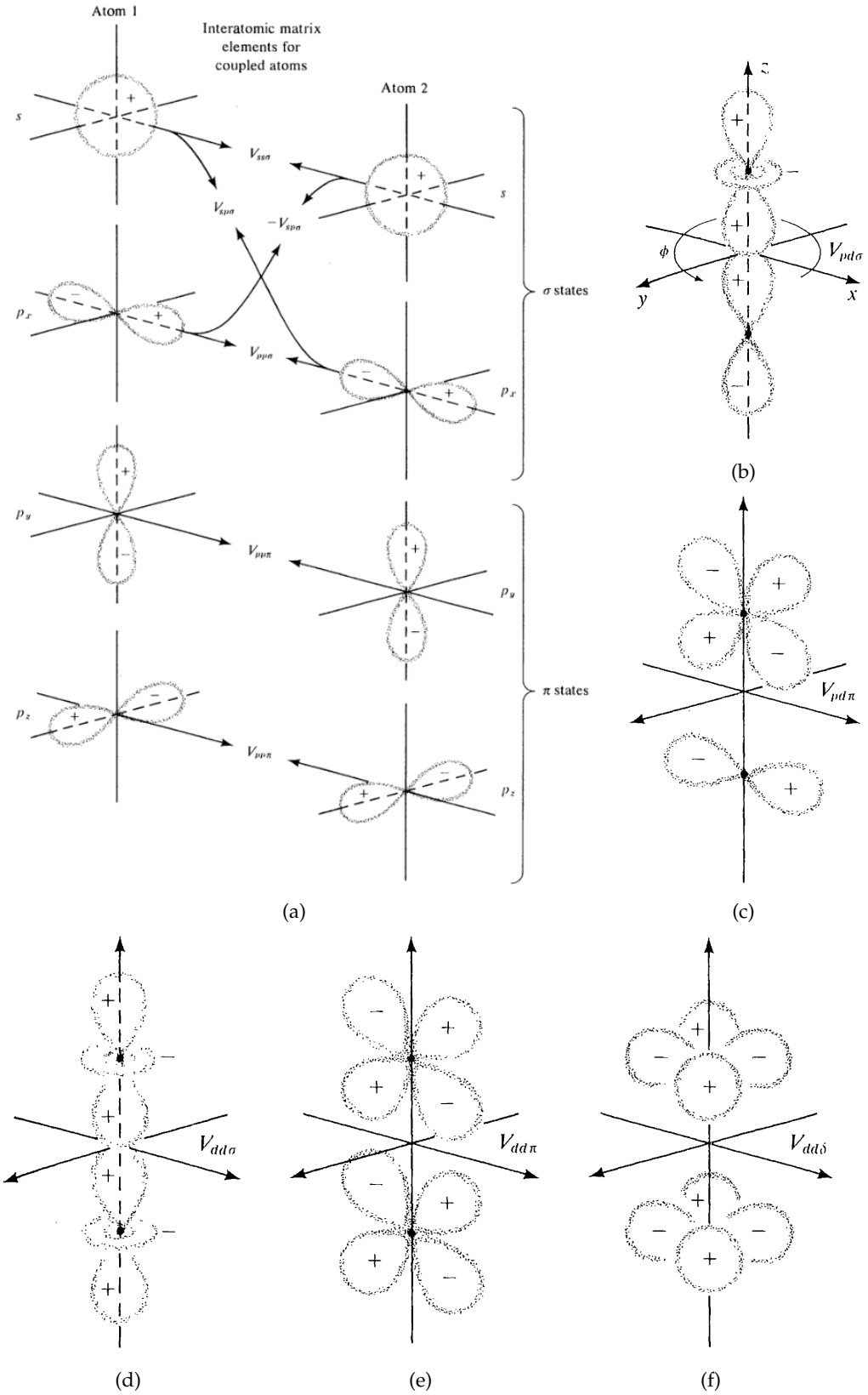

FIGURE 3.4.3: Coupling of atomic orbitals and the respective SKp. In (a) we show the bonds between *s* and *p*-orbitals, and their respective designations. (b) and (c) schematize the bonds formed by a *p*-orbital and a *d*-orbital, depending on the alignment with bond axis. (d), (e), and (f) represent the bonds between *d*-orbitals. These figures are taken from [60].

Crystal Field

The crystal field and interlayer S-S terms matrices are the only ones that do not need rotation. The crystal field matrix is the simplest of the two, given that its only non-null entries are the orbitals self-energy in the main diagonal,

$$H_0 = \text{diagonal}\left[\Delta_{p_{x/y}}, \Delta_{p_{x/y}}, \Delta_{p_{x/y}}, \Delta_{p_{x/y}}, \Delta_{p_z}, \Delta_{p_z}, \Delta_2, \Delta_1, \Delta_1, \Delta_2, \Delta_0\right]. \tag{3.4.16}$$

The second is discussed ahead.

Mo-Mo terms

As said, we write the matrices for each bond in terms of a locally adapted reference frame $\mathcal{O}''$, where its z axis is aligned with the bond in question. The hopping matrix for a Mo-Mo bond in such terms is given by

$$t_{\mathcal{O}''}^{\text{Mo-Mo}}\left(R_x(-\pi/2) : \mathbf{d}_6\right) = \begin{pmatrix} V_{dd\delta} & & & & \\ & V_{dd\pi} & & 0 & \\ & & V_{dd\pi} & & \\ & 0 & & V_{dd\delta} & \\ & & & & V_{dd\sigma} \end{pmatrix}. \tag{3.4.17}$$

For better intuition in the nature of the parameters for each bond, refer to Figures 3.4.3f, 3.4.3e and 3.4.3d, respectively, remembering that the bond axis, in this frame, is z. In the first and second to last, since neither of the lobes are in the bond axis, the orbital is a δ. The π bond has a linear dependence in z and a linear dependence in x or y as the orbitals involved. The σ bond is present in the only term dependent only of z.

To generate the entire matrix, we go from frame $\mathcal{O}''$ to the system frame by rotating the axes by $\theta_m = -m\pi/3 + \pi/2$ around z and by $\pi/2$ around x,

$$t_{\mathcal{O}}^{\text{Mo-Mo}(m)^{\alpha\beta}}(\mathbf{k}) = e^{-i\mathbf{k}\cdot(\boldsymbol{\delta}_\alpha - \boldsymbol{\delta}_\beta - R_{\theta_m}:\mathbf{d}_6)} \times$$
$$\times \left[\mathcal{D}_z^{(2)}\left(\frac{m\pi}{3} - \frac{\pi}{2}\right)\mathcal{D}_x^{(2)}\left(-\frac{\pi}{2}\right) t_{\mathcal{O}''}^{\text{Mo-Mo}}\left(R_x(-\pi/2) : \mathbf{d}_6\right)\mathcal{D}_x^{(2)}\left(\frac{\pi}{2}\right)\mathcal{D}_z^{(2)}\left(-\frac{m\pi}{3} + \frac{\pi}{2}\right)\right]^{\alpha\beta}, \tag{3.4.18}$$

and then sum on $m = 1, 2, ..., 6$,

$$H_{\text{Mo-Mo}} = \sum_{m=1}^{6} H^{(m)}_{\text{Mo-Mo}}, \tag{3.4.19}$$

yielding the full Mo-Mo Hamiltonian. Also, we made a further modification in our notation, writing the rotation angle as argument and the axis as subscript in $R_{\hat{\mathbf{n}}}(\theta)$, and the angular momentum quantum number l as superscript in $\mathcal{D}^{(l)}_{\hat{\mathbf{n}}}(\theta)$. Since we are dealing with d-orbitals, $l = 2$.

S-S terms

Repeating the procedure to the S-S hoppings we write

$$t^{\text{S-S}}_{\mathcal{O}''}\left(R_x(-\pi/2) : \mathbf{d}_6\right) = \begin{pmatrix} V_{pp\pi} & 0 & 0 \\ 0 & V_{pp\pi} & 0 \\ 0 & 0 & V_{pp\sigma} \end{pmatrix} \tag{3.4.20}$$

for each layer. Referring to Figure 3.4.3a, only the bonds with direction along z are δ. The others are parallel, and therefore, π.

To get the m-th hopping matrix, we do as before,

$$t^{\text{S-S}(m)^{\alpha\beta}}_{\mathcal{O}}(\mathbf{k}) = e^{-i\mathbf{k}\cdot(\delta_\alpha - \delta_\beta - R_{\theta_m}:\mathbf{d}_6)} \times$$
$$\times \left[\mathcal{D}^{(1)}_z\left(\frac{m\pi}{3} - \frac{\pi}{2}\right)\mathcal{D}^{(1)}_x\left(-\frac{\pi}{2}\right) t^{\text{S-S}}_{\mathcal{O}''}\left(R_x(-\pi/2) : \mathbf{d}_6\right)\mathcal{D}^{(1)}_x\left(\frac{\pi}{2}\right)\mathcal{D}^{(1)}_z\left(-\frac{m\pi}{3} + \frac{\pi}{2}\right)\right]^{\alpha\beta}, \tag{3.4.21}$$

applying the same rotations as in the Mo-Mo case.

However, the S-S terms count with an interlayer matrix as well. Its elements couple the S site in the bottom layer with the S site directly atop it in the top layer. Because the bonds are oriented in the z direction, only the p_z-orbitals couple head on, by means of a $V_{pp\sigma}$ parameter. The others couple laterally, forming a π bond,

$$H^{interlayer}_{\text{S-S}} = \begin{pmatrix} 0 & V_{pp\pi} & & & & \\ V_{pp\pi} & 0 & & & \mathbf{0} & \\ & & 0 & V_{pp\pi} & & \\ & & V_{pp\pi} & 0 & & \\ & \mathbf{0} & & & 0 & V_{pp\sigma} \\ & & & & V_{pp\sigma} & 0 \end{pmatrix}, \tag{3.4.22}$$

considering only the p-orbitals.

Mo-S terms

The Mo-S bonds are along the $\boldsymbol{\tau}_{n,s}$ vectors defined in equations (3.4.4) and (3.4.5). In the bond aligned frame, its Hamiltonian is

$$t^{\text{Mo-S}}_{\mathcal{O}''}\left(R_x\left(-\frac{\pi}{2}-s\phi\right):\boldsymbol{\tau}_{3,s}\right)=\begin{pmatrix}0 & V_{pd\pi} & 0 & 0 & 0\\ 0 & 0 & V_{pd\pi} & 0 & 0\\ 0 & 0 & 0 & 0 & V_{pd\sigma}\end{pmatrix}. \tag{3.4.23}$$

To get to the system frame, we rotate the main frame around the z axis by $\theta_n = 2n\pi/3 - \pi/2$. Then we pull the z axis an angle $\pi/2 + s\phi$, where ϕ is the angle defined in section 3.4.1 by $\phi = \arctan\left(\sqrt{3}u/a\right)$ and $s = \pm 1$ depending on the layer we are referring to. In total, we have

$$t^{\text{Mo-S}(s)^{\alpha\beta}}_{\mathcal{O}}(\mathbf{k}) = e^{-i\mathbf{k}\cdot(\boldsymbol{\delta}_\alpha-\boldsymbol{\delta}_\beta-R_{\theta_n}:\boldsymbol{\tau}_{3,s})}\times$$
$$\times\left[\mathcal{D}^{(1)}_z(-\theta_n)\,\mathcal{D}^{(1)}_x\left(-\frac{\pi}{2}-s\phi\right)t^{\text{Mo-S}}_{\mathcal{O}''}\left(R_x\left(-\frac{\pi}{2}-s\phi\right):\boldsymbol{\tau}_{3,s}\right)\mathcal{D}^{(2)}_x\left(\frac{\pi}{2}+s\phi\right)\mathcal{D}^{(2)}_z(-\theta_n)\right]^{\alpha\beta}, \tag{3.4.24}$$

with $s = \pm 1$ for the top/bottom layer.

S-Mo terms

The S-Mo bonds lay on the vectors $\boldsymbol{\delta}_{n,s}$, defined in equations (3.4.3) and (3.4.5). In the locally adapted frame, we have

$$t^{\text{S-Mo}}_{\mathcal{O}''}\left(R_x\left(-\frac{\pi}{2}+s\phi\right):\boldsymbol{\tau}_{3,s}\right)=-\begin{pmatrix}0 & 0 & 0\\ V_{pd\pi} & 0 & 0\\ 0 & V_{pd\pi} & 0\\ 0 & 0 & 0\\ 0 & 0 & V_{pd\sigma}\end{pmatrix}, \tag{3.4.25}$$

owing the minus sign to the orientation of the local frames. This is clear in Figure 3.4.4 for the $V_{pd\pi}$ and $V_{dp\pi}$ bonds. Because the orbitals are written as real spherical harmonics, they are proportional to the coordinates in subscript. Therefore, the non-null bonds are

the matrix elements

$$\begin{aligned} \langle d_{xz}| H |p_x\rangle &\propto x^2 z \\ \left\langle d_{yz}\right| H \left|p_y\right\rangle &\propto y^2 z \\ \langle d_{z^2}| H |p_z\rangle &\propto z^3, \end{aligned} \tag{3.4.26}$$

all odd in the inverted axes.

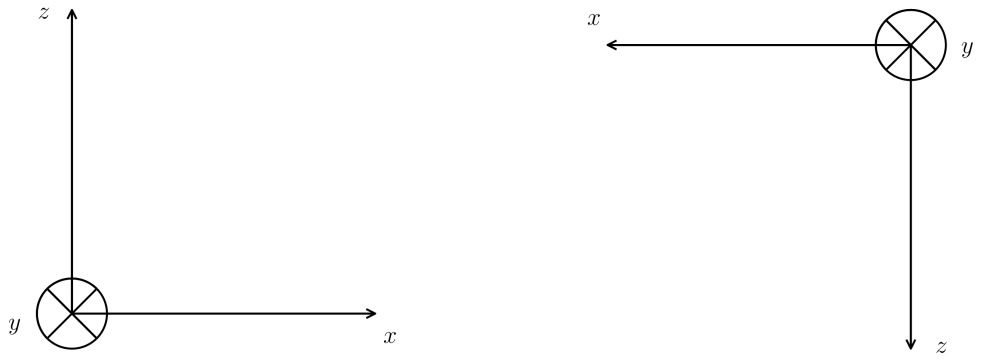

(a) (b)

FIGURE 3.4.4: Locally adapted frame of the Mo-S and S-Mo bonds, respectively, from the perspective of the Mo-S bonds.

As in the above case, we rotate around the z axis $\theta_n = -2n\pi/3 + \pi + \pi/6$ rads and $\pi/2 - s\phi$ around the x axis, yielding

$$t_{\mathcal{O}}^{\text{S-Mo}(n,s)^{\alpha\beta}}(\mathbf{k}) = e^{-i\mathbf{k}\cdot(\delta_\alpha - \delta_\beta - R_{\theta_n}:\delta_{3,s})} \times$$
$$\times \left[\mathcal{D}_z^{(2)}(-\theta_n)\,\mathcal{D}_x^{(2)}\left(-\frac{\pi}{2}+s\phi\right) t_{\mathcal{O}''}^{\text{S-Mo}}\left(R_x\left(-\frac{\pi}{2}+s\phi\right):\boldsymbol{\tau}_{3,s}\right)\mathcal{D}_x^{(1)}\left(\frac{\pi}{2}-s\phi\right)\mathcal{D}_z^{(1)}(\theta_n)\right]^{\alpha\beta}. \tag{3.4.27}$$

3.4.4 Even and odd decoupling

Besides rotational symmetry, our system manifests as well mirror symmetry in the xy plane, as we can see in Figure 3.4.1b, meaning that it stays the same after $z \to -z$. Therefore, the energy eigenbasis is also an eigenbasis to this mirror operator, and the eigenvectors falls into the two categories: symmetric and antisymmetric. Thus, we can study our system in the more appropriate basis

$$c^\dagger = \{c^\dagger_{d_{z2}}, c^\dagger_{d_{x^2-z^2}}, c^\dagger_{d_{xy}}, c^\dagger_{p_{x,S}}, c^\dagger_{p_{y,S}}, c^\dagger_{p_{z,S}}, c^\dagger_{d_{xz}}, c^\dagger_{d_{yz}}, c^\dagger_{p_{x,A}}, c^\dagger_{p_{y,A}}, c^\dagger_{p_{z,A}}\}, \tag{3.4.28}$$

where

$$\begin{aligned} c^{\dagger}_{p_{\alpha S/A}} &= \frac{1}{\sqrt{2}}\left(c^{\dagger}_{p_{\alpha,t}} \pm c^{\dagger}_{p_{\alpha,b}}\right), \ \alpha = x, y \\ c^{\dagger}_{p_{zS/A}} &= \frac{1}{\sqrt{2}}\left(c^{\dagger}_{p_{z,t}} \mp c^{\dagger}_{p_{z,b}}\right). \end{aligned} \tag{3.4.29}$$

To write the Hamiltonian in this basis, we make the transformation

$$UHU^{-1} = \begin{pmatrix} H_S & \mathbf{0} \\ \mathbf{0} & H_A \end{pmatrix}, \tag{3.4.30}$$

with

$$U = \begin{pmatrix} 0 & 0 & 0 & 0 & 0 & 0 & 0 & 0 & 0 & 0 & 1 \\ 0 & 0 & 0 & 0 & 0 & 0 & 0 & 0 & 0 & 1 & 0 \\ 0 & 0 & 0 & 0 & 0 & 0 & 1 & 0 & 0 & 0 & 0 \\ \frac{1}{\sqrt{2}} & \frac{1}{\sqrt{2}} & 0 & 0 & 0 & 0 & 0 & 0 & 0 & 0 & 0 \\ 0 & 0 & \frac{1}{\sqrt{2}} & \frac{1}{\sqrt{2}} & 0 & 0 & 0 & 0 & 0 & 0 & 0 \\ 0 & 0 & 0 & 0 & -\frac{1}{\sqrt{2}} & \frac{1}{\sqrt{2}} & 0 & 0 & 0 & 0 & 0 \\ 0 & 0 & 0 & 0 & 0 & 0 & 0 & 1 & 0 & 0 & 0 \\ 0 & 0 & 0 & 0 & 0 & 0 & 0 & 0 & 1 & 0 & 0 \\ -\frac{1}{\sqrt{2}} & \frac{1}{\sqrt{2}} & 0 & 0 & 0 & 0 & 0 & 0 & 0 & 0 & 0 \\ 0 & 0 & -\frac{1}{\sqrt{2}} & \frac{1}{\sqrt{2}} & 0 & 0 & 0 & 0 & 0 & 0 & 0 \\ 0 & 0 & 0 & 0 & \frac{1}{\sqrt{2}} & \frac{1}{\sqrt{2}} & 0 & 0 & 0 & 0 & 0 \end{pmatrix}, \tag{3.4.31}$$

yielding a block diagonal matrix, each block with a well-defined parity. The resulting band structure, is composed of symmetric and antisymmetric energy bands, plotted in Figure 3.4.5a in blue and red, respectively.

3.4.5 Beyond Slater-Koster Models

In this last section concerning the TMDs, we build the Hamiltonian and compute its band structure for this system obtained for ab initio wannierization. Following reference [41], we present the matrix elements of the Hamiltonian after Fourier transformation to the reciprocal space. Using the notation $t^{s}_{i,j} = \langle \phi_i | H | \phi_j \rangle$, for the hopping matrix element from the state ϕ_j to the state ϕ_i, in the real space, and the basis

$$c^{\dagger} = \{c^{\dagger}_{d_{xz}}, c^{\dagger}_{d_{yz}}, c^{\dagger}_{z,A}, c^{\dagger}_{p_{x,A}}, c^{\dagger}_{p_{y,A}}, c^{\dagger}_{d_{z^2}}, c^{\dagger}_{d_{xy}}, c^{\dagger}_{d_{x^2-y^2}}, c^{\dagger}_{p_{z,S}}, c^{\dagger}_{p_{x,S}}, c^{\dagger}_{p_{y,S}}\}, \tag{3.4.32}$$

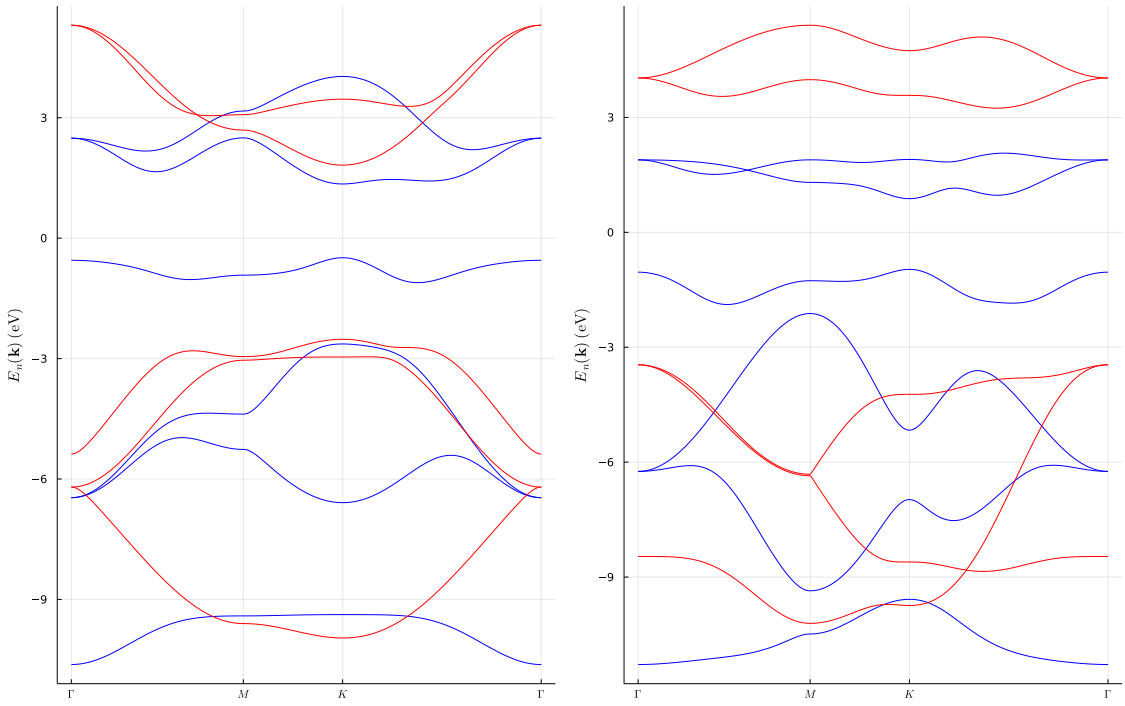

(a) (b)

FIGURE 3.4.5: Band structure for MoS_2, with SKp from [40] in (a) and from [42] in (b), listed both in Table 3.4.1. In blue, we show the bands from the even Hamiltonian, H_S and in red from the odd Hamiltonian, H_A.

Slater-Koster Parameters in eV		
Parameter	Reference [40]	Reference [42]
$\Delta_{p_{x/y}}$	- 0.780	- 3.559
Δ_{p_z}	- 7.740	- 6.886
Δ_2	- 2.529	- 1.511
Δ_1	0	- 0.05
Δ_0	- 1.016	- 1.094
$V_{pp\sigma}$	0.696	1.225
$V_{pp\pi}$	0.278	- 0.467
$V_{dd\sigma}$	- 0.933	- 0.895
$V_{dd\pi}$	- 0.478	0.252
$V_{dd\delta}$	- 0.442	0.228
$V_{pd\sigma}$	- 2.619	3.689
$V_{pd\pi}$	- 1.396	- 1.241

TABLE 3.4.1: SKp for the covalent bonds according to [40, 42].

from the SKp in Table D.0.1 and their relations in equations (3.4.39) and (3.4.40), we write the diagonal terms as

$$H_{i,i}(\mathbf{k}) = \varepsilon_i + 2t^1_{i,i}\cos(\mathbf{k}\cdot\mathbf{d}_6) + 2t^2_{i,i}\left[\cos(\mathbf{k}\cdot\mathbf{d}_1) + \cos(\mathbf{k}\cdot\mathbf{d}_2)\right]. \tag{3.4.33}$$

The off-diagonal hopping matrix elements between same-type neighbors split into two categories depending on the orbitals' mirror symmetry in relation to the yz plane. The symmetric terms are

$$H_{i,j}(\mathbf{k}) = 2t^1_{i,j}\cos(\mathbf{k}\cdot\mathbf{d}_6) + t^2_{i,j}\left(e^{-i\mathbf{k}\cdot\mathbf{d}_1} + e^{-i\mathbf{k}\cdot\mathbf{d}_2}\right) + t^3_{i,j}\left(e^{i\mathbf{k}\cdot\mathbf{d}_1} + e^{i\mathbf{k}\cdot\mathbf{d}_2}\right) \tag{3.4.34}$$

for the pairs $(i,j) = (3,5),(6,8),(9,11)$, and the antisymmetric terms are

$$H_{i,j}(\mathbf{k}) = -2it^1_{i,j}\sin(\mathbf{k}\cdot\mathbf{d}_6) + t^2_{i,j}\left(e^{-i\mathbf{k}\cdot\mathbf{d}_1} - e^{-i\mathbf{k}\cdot\mathbf{d}_2}\right) + t^3_{i,j}\left(-e^{i\mathbf{k}\cdot\mathbf{d}_1} + e^{i\mathbf{k}\cdot\mathbf{d}_2}\right) \tag{3.4.35}$$

for the pairs $(i,j) = (1,2),(3,4),(4,5),(6,7),(7,8),(9,10),(10,11)$. The hoppings between Mo and S are introduced in the Hamiltonian, for the symmetric states, as

$$H_{i,j}(\mathbf{k}) = t^4_{i,j}\left(e^{i\mathbf{k}\cdot\delta_3} - e^{i\mathbf{k}\cdot\delta_2}\right) \tag{3.4.36}$$

for the pairs $(i,j) = (3,1),(5,1),(4,2),(10,6),(9,7),(11,7),(10,8)$, while for the antisymmetric states we have

$$H_{i,j}(\mathbf{k}) = t^4_{i,j}\left(e^{i\mathbf{k}\cdot\delta_3} + e^{i\mathbf{k}\cdot\delta_2}\right) + t^5_{i,j}e^{i\mathbf{k}\cdot\delta_1} \tag{3.4.37}$$

for $(i,j) = (4,1),(3,2),(5,2),(9,6),(11,6),(10,7),(9,8),(11,8)$. Finally, including couplings beyond first neighbors for different-type atoms, we have the Hamiltonian matrix terms

$$\begin{aligned}
H_{9,6}(\mathbf{k}) &= t^6_{9,6}\left(e^{-2i\mathbf{k}\cdot\delta_1} + e^{i\mathbf{k}\cdot(\mathbf{d}_6+\delta_1)} + e^{i\mathbf{k}\cdot(\mathbf{d}_3+\delta_1)}\right)\\
H_{11,6}(\mathbf{k}) &= t^6_{11,6}\left(e^{-2i\mathbf{k}\cdot\delta_1} - \frac{1}{2}e^{i\mathbf{k}\cdot(\mathbf{d}_6+\delta_1)} - \frac{1}{2}e^{i\mathbf{k}\cdot(\mathbf{d}_3+\delta_1)}\right)\\
H_{10,6}(\mathbf{k}) &= \frac{\sqrt{3}}{2}t^6_{11,6}\left(-e^{i\mathbf{k}\cdot(\mathbf{d}_6+\delta_1)} + e^{i\mathbf{k}\cdot(\mathbf{d}_3+\delta_1)}\right)\\
H_{9,8}(\mathbf{k}) &= t^6_{9,8}\left(e^{-2i\mathbf{k}\cdot\delta_1} - \frac{1}{2}e^{i\mathbf{k}\cdot(\mathbf{d}_6+\delta_1)} - \frac{1}{2}e^{i\mathbf{k}\cdot(\mathbf{d}_3+\delta_1)}\right)\\
H_{9,7}(\mathbf{k}) &= \frac{\sqrt{3}}{2}t^6_{9,8}\left(-e^{i\mathbf{k}\cdot(\mathbf{d}_6+\delta_1)} + e^{i\mathbf{k}\cdot(\mathbf{d}_3+\delta_1)}\right)\\
H_{10,7}(\mathbf{k}) &= \frac{3}{4}t^6_{11,8}\left(e^{i\mathbf{k}\cdot(\mathbf{d}_6+\delta_1)} + e^{i\mathbf{k}\cdot(\mathbf{d}_3+\delta_1)}\right)\\
H_{11,7}(\mathbf{k}) &= H_{10,8}(\mathbf{k}) = \frac{\sqrt{3}}{4}t^6_{11,8}\left(e^{i\mathbf{k}\cdot(\mathbf{d}_6+\delta_1)} - e^{i\mathbf{k}\cdot(\mathbf{d}_3+\delta_1)}\right)\\
H_{11,8}(\mathbf{k}) &= t^6_{11,8}\left(e^{-2i\mathbf{k}\cdot\delta_1} + \frac{1}{4}e^{i\mathbf{k}\cdot(\mathbf{d}_6+\delta_1)} + \frac{1}{4}e^{i\mathbf{k}\cdot(\mathbf{d}_3+\delta_1)}\right).
\end{aligned} \tag{3.4.38}$$

Because the Hamiltonian needs to be hermitian, every term $H_{i,j}$ has associated a conjugate term, $H_{j,i} = H^*_{i,j}$.

Most of these hoppings values, based on density function theory calculations, are listed in Table D.0.1. The ones that are not, are related to these by

$$\begin{aligned}
\varepsilon_\alpha &= \varepsilon_\beta \\
t^2_{\alpha,\alpha} &= \frac{1}{4}t^1_{\alpha,\alpha} + \frac{3}{4}t^1_{\beta,\beta} \\
t^2_{\beta,\beta} &= \frac{3}{4}t^1_{\alpha,\alpha} + \frac{1}{4}t^1_{\beta,\beta} \\
t^2_{\gamma,\gamma} &= t^1_{\gamma,\gamma} \\
t^{2,3}_{\gamma,\beta} &= \pm\frac{\sqrt{3}}{2}t^1_{\gamma,\alpha} - \frac{1}{2}t^1_{\gamma,\beta} \\
t^{2,3}_{\alpha,\beta} &= \pm\frac{\sqrt{3}}{4}\left(t^1_{\alpha,\alpha} - t^1_{\beta,\beta}\right) - t^1_{\alpha,\beta} \\
t^{2,3}_{\gamma,\alpha} &= \frac{1}{2}t^2_{\gamma,\alpha} \pm \frac{\sqrt{3}}{2}t^2_{\gamma,\beta}
\end{aligned} \tag{3.4.39}$$

for the pairs ($\alpha = 1$, $\beta = 2$), ($\alpha = 4$, $\beta = 5$, $\gamma = 3$), ($\alpha = 7$, $\beta = 8$, $\gamma = 6$), ($\alpha = 10$, $\beta = 11$, $\gamma = 9$), and

$$\begin{aligned}
t^4_{\alpha',\alpha} &= \frac{1}{4}t^5_{\alpha',\alpha} + \frac{3}{4}t^5_{\beta',\beta} \\
t^4_{\beta',\beta} &= \frac{3}{4}t^5_{\alpha',\alpha} + \frac{1}{4}t^5_{\beta',\beta} \\
t^4_{\beta',\alpha} &= t^4_{\alpha',\beta} = -\frac{\sqrt{3}}{4}t^5_{\alpha',\alpha} + \frac{\sqrt{3}}{4}t^5_{\beta',\beta} \\
t^4_{\gamma',\alpha} &= -\frac{\sqrt{3}}{2}t^5_{\gamma',\beta} \\
t^4_{\gamma',\beta} &= -\frac{1}{2}t^5_{\gamma',\beta} \\
t^4_{9,6} = t^5_{9,6}, t^4_{10,6} &= -\frac{\sqrt{3}}{2}t^5_{11,6}, t^4_{11,6} = -\frac{1}{2}t^5_{11,6}
\end{aligned} \tag{3.4.40}$$

for ($\alpha = 1$, $\beta = 2$, $\alpha' = 4$, $\beta' = 5$, $\gamma' = 3$), ($\alpha = 7$, $\beta = 8$, $\alpha' = 10$, $\beta' = 11$, $\gamma' = 9$).

The resulting band structure is plotted in Figure 3.4.6, where, as before, in blue lines we plot the symmetric bands and in red the antisymmetric.

Comparing the three models, they all agree very well on the valence and conduction bands, and less and less as the energy grows in absolute value.

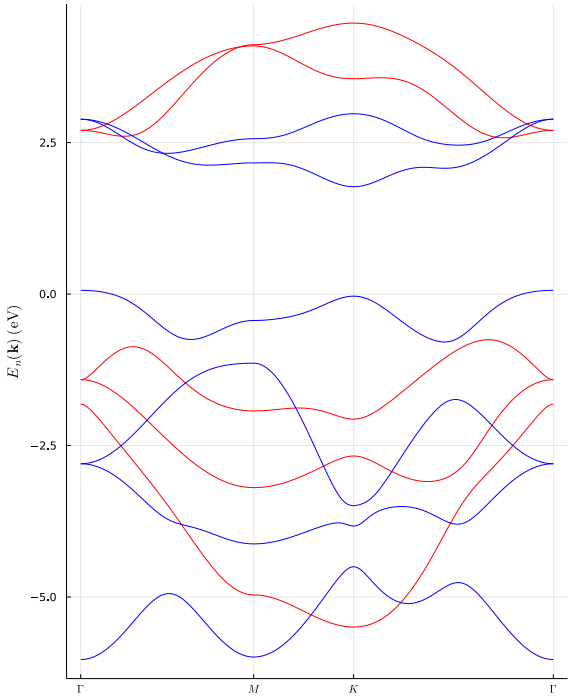

FIGURE 3.4.6: Band structure for MoS_2, with SKp from [41], listed in Table D.0.1. In blue, we show the symmetric bands and in red the antisymmetric.

3.5 Twisted Bilayer Graphene

The rising interest created around the vdW structures has put tBLG in the spotlight. The misalignment of its layers allow the reduction of the Fermi velocity [22–24], and for some very small twist angles, called the magic angles [27, 28], the van Hove singularities coalesce into one, forming a flat band. Because of that, the study of this system is imperative.

In this section, build its tight-binding Hamiltonian and explore the band structure for decreasing angles.

3.5.1 Lattice

The tBLG system we consider in this section builds on the BLG, studied in section 3.2. The difference is that, now, the top layer is rotated relatively to the bottom one. This is shown in Figure 3.5.1. Such a rotation, changes the system periodicity. Letting a single layer Bravais vector be denoted as $\mathbf{a}_i^{(l)}$, where $i = 1, 2$ specifies the vector and $l = 1, 2$ the layer, the top layer's lattice vectors are

$$\mathbf{a}_i^{(2)} = R(\theta) \cdot \mathbf{a}_i^{(1)}, \tag{3.5.1}$$

with $R(\theta)$ being the usual rotation matrix,

$$\mathcal{R}(\theta) = \begin{pmatrix} \cos(\theta) & -\sin(\theta) \\ \sin(\theta) & \cos(\theta) \end{pmatrix}. \tag{3.5.2}$$

Analogously, for the orbitals positions, we write

$$\delta_{\alpha_2} = R(\theta) \cdot \delta_{\alpha_1}, \tag{3.5.3}$$

where α_l denotes the orbital from the layer $l = 1, 2$.

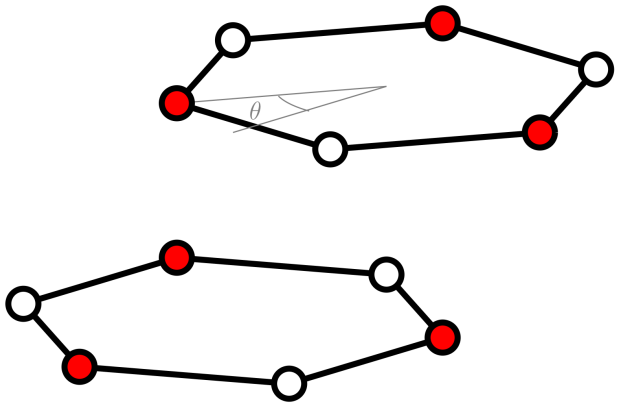

FIGURE 3.5.1: tBLG in a Bernal stacking, rotated an angle θ.

Not only that, but the unit cell is different as well. With the introduced rotation, the system no longer maintains its simple periodicity, losing it altogether to form an incommensurate structure, or keeping a more complex one, that encompasses a larger unit cell. The resulting scenario depends on the rotation.

Commensurate Structures

As mentioned before, if the rotation was of $\pi/3$, the configuration would be equivalent to how it started, the BLG. Thus, the angle of rotation needs to be between 0 and $\pi/3$. Moreover, in order to maintain a commensurate structure, i.e., periodical in space, this angle has to obey the following condition,

$$\cos(\theta) = \frac{3m^2 + 3mr + r^2/2}{3m^2 + 3mr + r^2}, \quad m, r \in \mathbb{N}, \tag{3.5.4}$$

according to [61]. This produces a system where the Bravais vectors are, in terms of the bottom layer's ones,

$$\begin{pmatrix} \mathbf{t}_1 \\ \mathbf{t}_2 \end{pmatrix} = T_c(m,r) \begin{pmatrix} \mathbf{a}_1 \\ \mathbf{a}_2 \end{pmatrix}, \tag{3.5.5}$$

(the layer superscripts were omitted so that the notation is not so cumbersome) where the matrix $T_c(m,r)$ has two conditions, depending on the m and r integers (see Appendix B), [61],

$$T_c(m,r) = \begin{cases} \begin{pmatrix} m & m+r \\ -(m+r) & 2m+r \end{pmatrix} \text{ if } \gcd(r,3) = 1 \\ \\ \begin{pmatrix} m+r/3 & r/3 \\ -r/3 & m+2r/3 \end{pmatrix} \text{ if } \gcd(r,3) = 3 \end{cases}. \tag{3.5.6}$$

The new unit cell, or supercell, represented for $m = r = 1$, i.e., $\theta \simeq 22°$, in Figure 3.5.2, holds $\det(T_c(m,r))$ graphene unit cells in each layer, where, by $\det(T_c(m,r))$, we mean the $T_c(m,r)$ matrix's determinant.

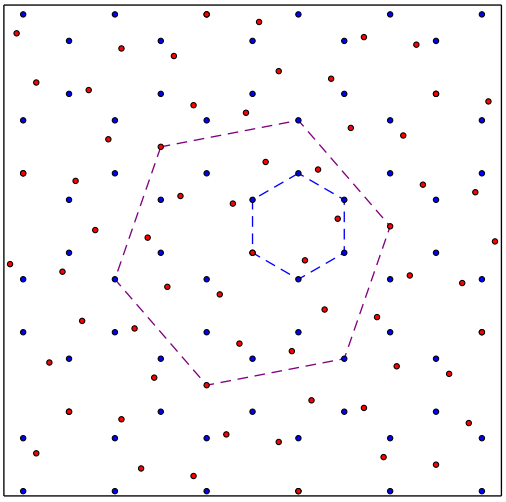

FIGURE 3.5.2: Commensurate unit cell for two honeycomb lattices with a rotation. The blue dots represent the bottom layer's honeycomb lattice, with unit cell drawn in the blue dashed lines, and the red dots are the same for the top layer. These, however, are rotated by the commensurate angle $\theta \simeq 22°$. The resulting commensurate supercell is shown in the purple dashed lines.

3.5.2 Tight-Binding Model

As our stacked systems until here, the tBLG Hamiltonian is split in two smaller operators. One accounts for the hoppings in the same layer, and other to couple both layers,

$$H_{tBLG} = H_{intra} + H_{inter}. \tag{3.5.7}$$

The intralayer still is the SLG's Hamiltonian, $H_{intra} = H_{SLG}$, and the interlayer has the same general form,

$$H_{inter} = \sum_{\mathbf{R},\boldsymbol{\zeta}_\perp} \sum_{\alpha,\beta} c_\alpha^\dagger(\mathbf{R}) t_\perp^{\alpha\beta}(\boldsymbol{\zeta}_\perp) c_\beta(\mathbf{R}+\boldsymbol{\zeta}_\perp), \tag{3.5.8}$$

as the systems before.

However, the matrices in reciprocal space are much larger than the ones for the systems without rotation, the smallest being 28×28, for $\theta \simeq 22°$. Therefore, we write them generally as

$$H_{inter} = \sum_{\mathbf{k}} \sum_{\alpha,\beta} c_\alpha^\dagger(\mathbf{k}) t_\perp^{\alpha\beta}(\mathbf{k}) c_\beta(\mathbf{k}) \tag{3.5.9}$$

with $t_\perp^{\alpha\beta}(\mathbf{k}) = e^{-i\mathbf{k}\cdot(\delta_\alpha - \delta_\beta)} \sum_{\boldsymbol{\zeta}_\perp} t_\perp(\boldsymbol{\zeta}_\perp) e^{i\mathbf{k}\cdot\boldsymbol{\zeta}_\perp}$, where the α and β are now summed over $2\det(T_c(m,r))$ sites.

Large Angles And Intermediate Angles

Let us say we have two uncoupled stacked layers. Overall, the band structure is the same, but since we rotated our top layer, the points in the reciprocal space of each layer do not, in general, coincide; the reciprocal space is rotated as well by the same angle. This way, in the region between the Dirac points of the bottom and top layers, $\mathbf{K}_1$ and $\mathbf{K}_2$ respectively, the bands emerging from these intersect at energy

$$E_n\left(\mathbf{K}_1 + \frac{\Delta\mathbf{K}}{2}\right) \simeq \pm\hbar v_F \frac{|\Delta\mathbf{K}|}{2}, \tag{3.5.10}$$

with $\Delta\mathbf{K} \equiv \mathbf{K}_2 - \mathbf{K}_1$ and v_F being the graphene velocity absolute value, computed in equation (3.1.14).

For smaller rotation angles, the K points deviate less from each other, and the converse if the rotation angle is larger, i.e., $|\Delta\mathbf{K}|$ is larger for bigger angles. The bands then meet closer or farther, according to the rotation.

Turning on the coupling, $t_\perp$, instead of intersecting each other, the bands open a gap of the order of the interlayer coupling. This is seen in Figures 3.5.3a and 3.5.3b, where in

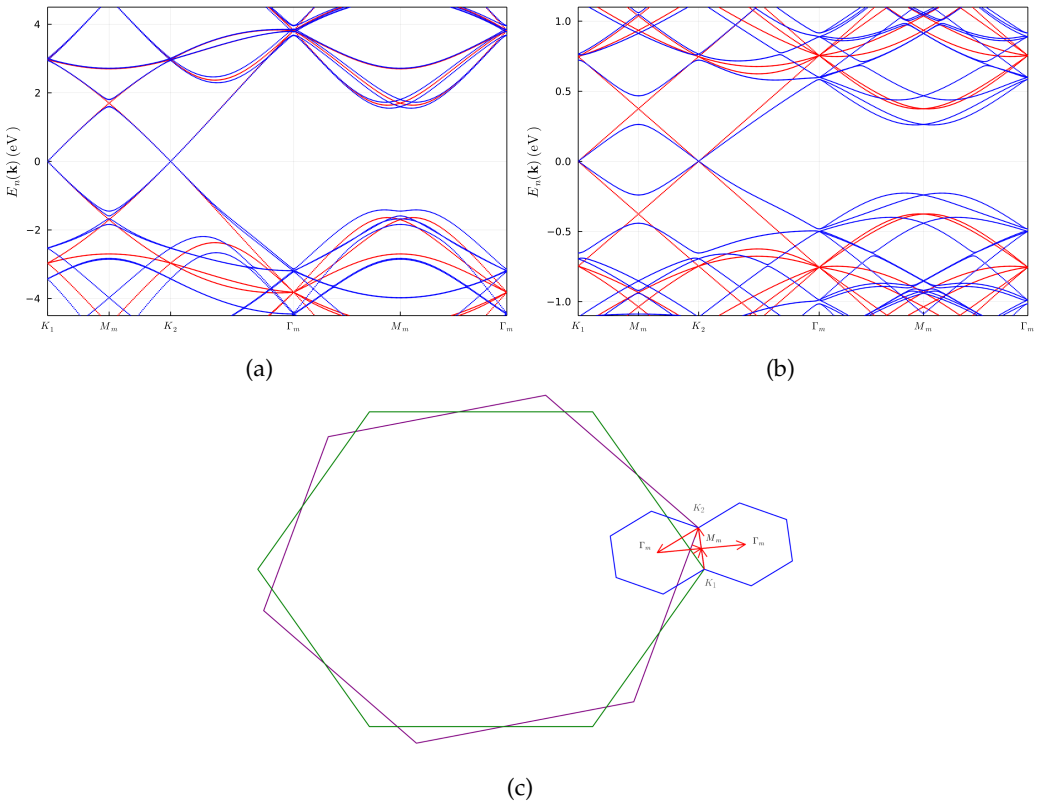

FIGURE 3.5.3: tBLG's (in blue) and decoupled system (in red) band structure for the angles $\theta \simeq 22°$ in (a) and $\theta \simeq 4°$, along the path in (b). In (c) we show a scheme of the path taken for the plots in (a) and (b)).

blue, we plot the tBLG's band structures for $\theta \simeq 22°$, and $\theta \simeq 4°$, respectively. In red, we plot the correspondent decoupled system. From one figure to the other, we see that the mentioned (and apparent*) gap grows, leaving in the midst of the separated bands the intersection of the decoupled cones.

Small Angles

With the decreasing of the angle, more interesting phenomena begins to appear. As the gap continues to grow, the valence and conduction bands slowly approach each other. The band flattens completely when

$$\mathbf{v}_F = \frac{1}{\hbar}\nabla_{\mathbf{k}} E_n(\mathbf{k}) = \mathbf{0}, \tag{3.5.11}$$

yielding a condition for the angles where it happens, [27, 44]. These are called the magic angles, and in tBLG, the largest of them is $\theta \simeq 1°$. In Figures 3.5.4a and 3.5.4b, we observe as this develops. When already at a small angle $\theta \simeq 1.8°$, with a band structure

*It is a consequence of the chosen path.

looking very differently than the ones in Figure 3.5.3, having the bands above and below the conduction and valence band strayed away from the others, and the cones continued to flatten, the angle keeps being decreased, and we reach in Figure 3.5.4b the flat band regime.

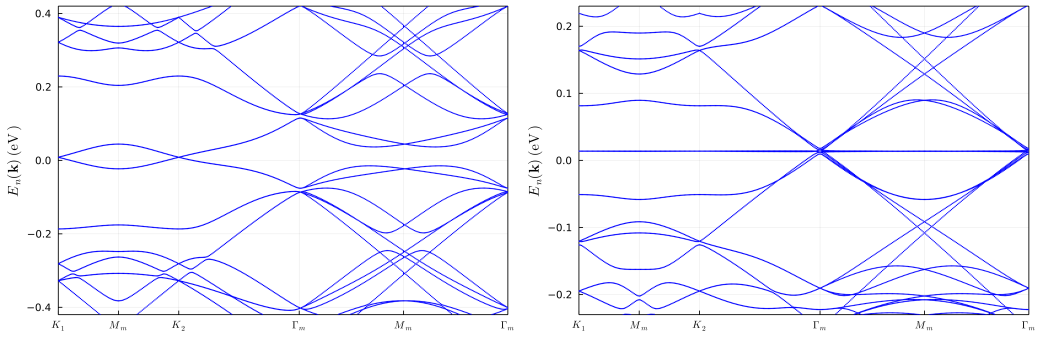

(a) (b)

FIGURE 3.5.4: tBLG's band structure for the angles $\theta \simeq 1.8°$ in (a), $\theta \simeq 1°$ in (b), along the path in Figure 3.5.3c.

3.6 Twisted Trilayer Graphene

The tTLG displays some characteristics of the tBLG, namely the flat band regime. However, in tTLG this happens for an angle larger by a factor of $\sqrt{2}$, that is an experimental advantage, [37].

In the next section, the tight-binding Hamiltonian of the tTLG is built, and the band structure considered for large, intermediate and small angles.

3.6.1 Lattice

If the tBLG system builds on the BLG, then the tTLG builds on the TLG, in section 3.3. We consider the mirror symmetric tTLG, where the middle layer is rotated an angle θ, as schematized in Figure 3.6.1. Its vectors are as in tBLG

$$\mathbf{a}_i^{(2)} = R(\theta) \cdot \mathbf{a}_i^{(1)}, \quad \delta_{\alpha_2} = R(\theta) \cdot \delta_{\alpha_1}, \tag{3.6.1}$$

for $i = 1, 2$. However, since the outer layers remain aligned, the top layer's vectors are equal to the ones of the bottom layer,

$$\mathbf{a}_i^{(3)} = \mathbf{a}_i^{(1)}, \quad \delta_{\alpha_3} = \delta_{\alpha_1}. \tag{3.6.2}$$

3.6.2 Tight-Binding Model

Once again, the tight-binding Hamiltonian is divided into intralayer and interlayer parts, where the intralayer is the SLG Hamiltonian and the interlayer, in reciprocal space, is the same as in equation (3.2.15), where the orbitals sum over $3\det(T_c(m,r))$ sites.

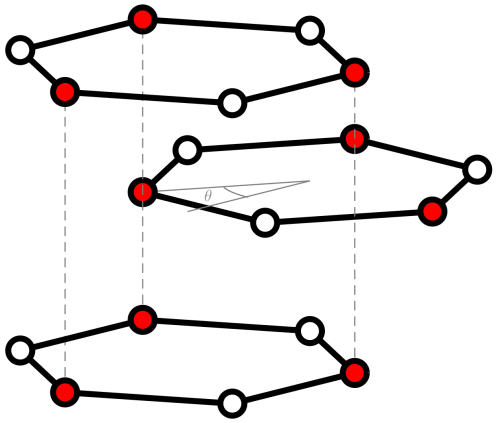

FIGURE 3.6.1: tTLG in a Bernal stacking, rotated an angle θ.

Large Angles And Intermediate Angles

Jumping right into the band structure, looking at Figure 3.6.2, we see that the decoupled system, in red, is not so noticeable as in Figure 3.5.3, for the tBLG. The reason for this is that there are another blue bands exactly atop it.

The tTLG, more specifically, the mirror tTLG, that we study here, is symmetric under z inversions. As a consequence, its Hamiltonian may be separated into independent symmetric and antisymmetric parts, that do not couple with each other. Thus, the eigenstates of the first are a combination of the states

$$|+\rangle = \frac{1}{\sqrt{2}}\left(|1\rangle + |3\rangle\right), \quad |2\rangle\,, \tag{3.6.3}$$

and those of the second are

$$|-\rangle = \frac{1}{\sqrt{2}}\left(|1\rangle - |3\rangle\right), \tag{3.6.4}$$

where $|n\rangle$ is a wave function of the n-th layer, [37]. The energy bands, are also either due to the symmetric or the antisymmetric part. The Dirac cones we see superimposing the decoupled system is a consequence of the last. Since it is decoupled from the middle band (and the outer bands are supposed to be decoupled as well), the cone is seen, for every angle, exactly as two SLG bands.

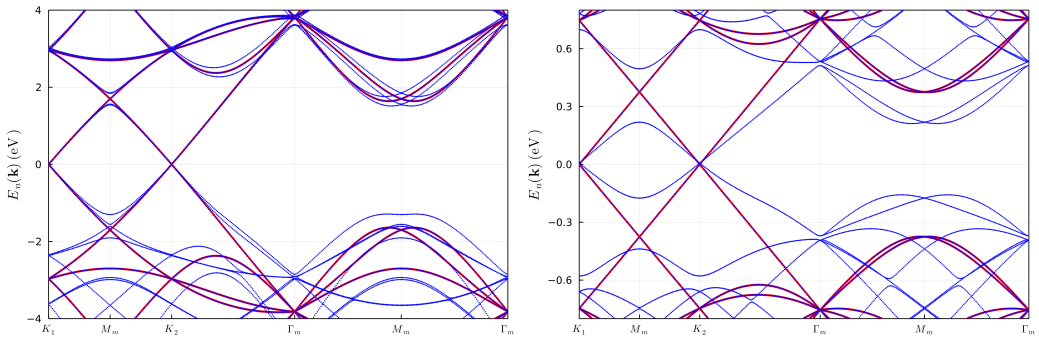

(a) (b)

FIGURE 3.6.2: tTLG's (in blue) and decoupled system (in red) band structure for the angles $\theta \simeq 22°$ in (a) and $\theta \simeq 4°$ in (b), along the path in Figure 3.5.3c.

As for the remaining bands, they behave similarly to the ones in the tBLG, opening a gap at the band crossing that grows as the angle decreases.

Small Angles

Concerning small angles, the tTLG has flatter bands sooner than the tBLG, as one may conclude comparing the Figures 3.6.3a and 3.5.4a. Additionally, in tTLG the flat band is reached at an angle $\sqrt{2}$ larger than the tBLG's magic angle, moving from $\theta \simeq 1°$ to $\theta \simeq 1.5°$, [36], as seen in Figure 3.6.3b. This is due to the fact that the coupling between the even combination, $|+\rangle$, and the middle layer is in turn stronger than the interlayer coupling of the tBLG by a factor of $\sqrt{2}$, [37].

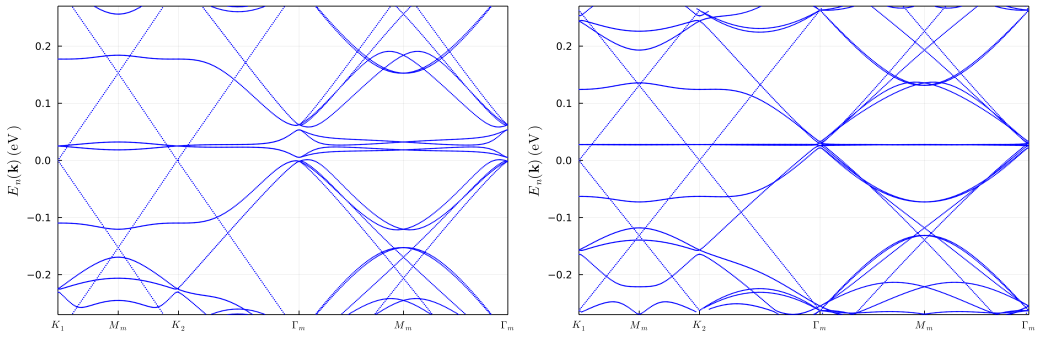

(a) (b)

FIGURE 3.6.3: tTLG's band structure for the angles $\theta \simeq 1.8°$ in (a), $\theta \simeq 1.5°$ in (b), along the path in Figure 3.5.3c.

3.7 Numerical Methods

The graphs presented throughout this and next section were made numerically, using Julia [62] as programming language. In general, to make these plots, one has to build a Hamiltonian function that takes a $\mathbf{k}$ vector for argument, create a path or a grid in the reciprocal space, and compute the eigenvalues and eigenvectors for each point. The eigenvalues yield the energy bands, while the eigenvectors are used to compute the ARPES visibility. For this, we do as explained in the previous chapter, summing the eigenvectors coefficients $a_\alpha(\mathbf{k})$ with respective phases, and compute the sum's squared absolute value. With this information, we are able to produce graphs showing the band structure along a path and constant energy plots, with their visibilities and DoS plots.

In what follows, to tackle more specific points, we separate our discussion into Hamiltonians for the TMDs and layered graphene systems, and energy plots.

3.7.1 Hamiltonian

Transition Metal Dichalcogenide Monolayers

Throughout this thesis, the need to build somewhat complex Hamiltonian matrices arose. The first time we met this difficulty was in the TMDs Hamiltonian. Here, as explained in section 3.4.2, we write explicitly the matrix referring to a neighbor and then rotate it to account for the symmetrical equivalent neighbors.

Layered Graphene

For the systems with layers of graphene, since twisted systems give too large unit cells, we started by developing a code capable of receiving Hamiltonians for supercells of SLG. The code is slow (see Appendix C). This function took as input a $\mathbf{k}$ point, the considered hoppings and their vectors, and the number of graphene unit cells we want our supercell to encompass. When running, it pivoted around each orbital to establish the specified hoppings (we considered only nearest-neighbors in its implementation), and saved this information in the Hamiltonian matrix.

Due to the ever-growing complexity of our systems, we found it better to take another route. Therefore, for the layered graphene, either twisted or without a twist, the Hamiltonians were built using the Julia's package Quantica.jl, [63]. In it, to build the Hamiltonians, as input, we define the lattice and sublattice positions by means of tuples

and vectors, and feed the sublattice to the `sublat()` function, and in turn this and the lattice tuples to the `lattice()` function. Next, we specify amongst what orbitals we want hoppings and their values in `hopping()`, and use this function and the `lattice()` outputs as arguments for the `hamiltonian()` function, that creates the Hamiltonian meeting these criteria.

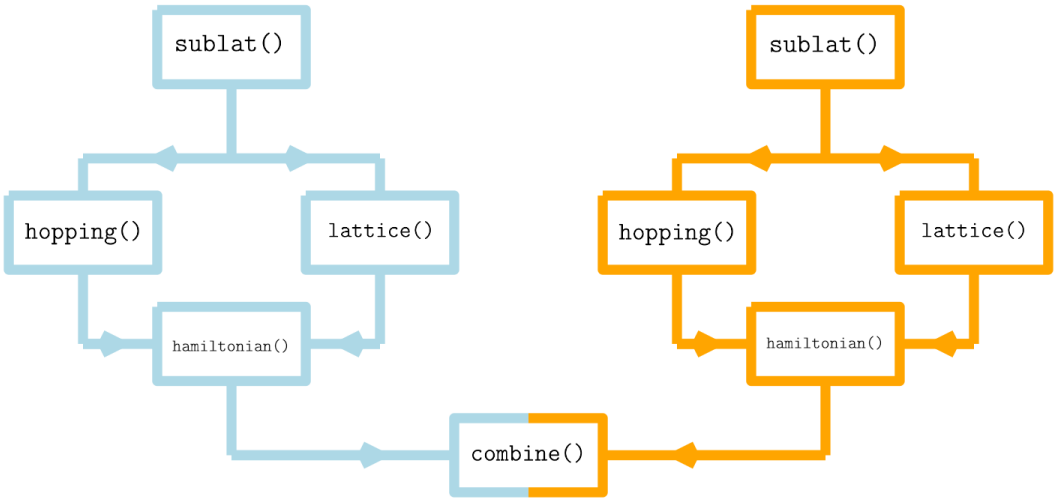

FIGURE 3.7.1: Scheme of the used Quantica functions to create the Hamiltonian for two layers, without twist.

Finally:

- **for layers without twist:** we simply couple both Hamiltonians in the `combine()` function; a scheme of this is in Figure 3.7.1.
- **for layers with twist:** we first need to build a bigger unit cell (with `unitcell()`), that is commensurate with the other layer's cell, also expanded, and only then couple the Hamiltonians with the `combine()` function; a hierarchy graph for this is shown in Figure 3.7.2.

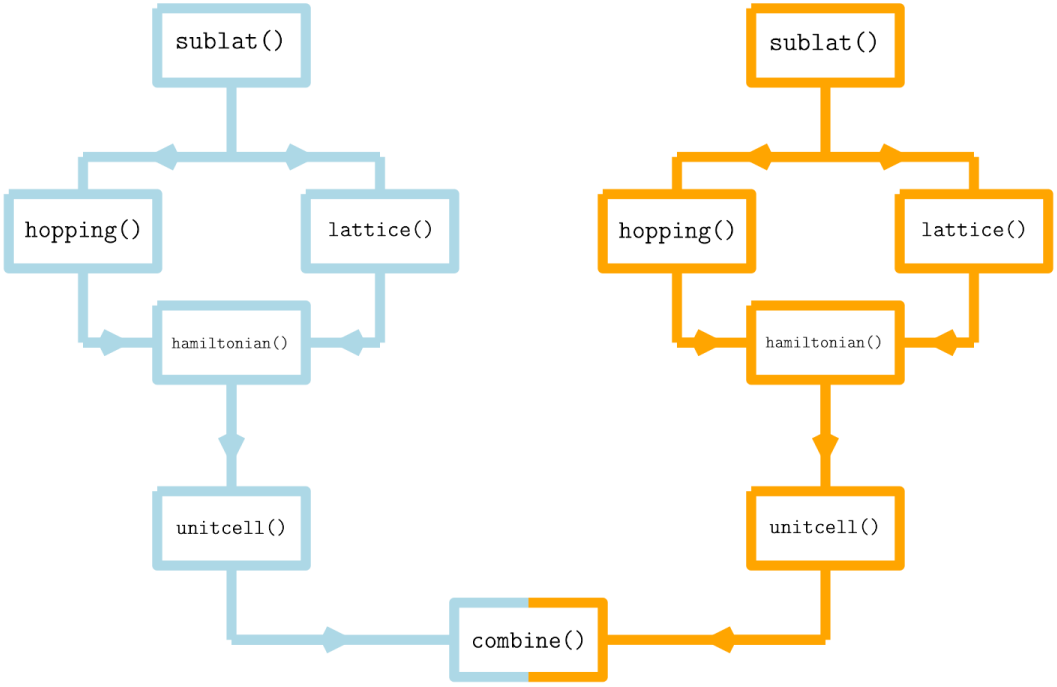

FIGURE 3.7.2: Scheme of the used Quantica functions to create the Hamiltonian for two twisted layers.

3.7.2 Energy Plots

Once the Quantica Hamiltonian is created, we need to study it for some set of **k** points. To ready its matrix for a given **k**, we use the `bloch()` function, which creates a sparse matrix with the non-null entries for the Bloch Hamiltonian.

The next step would be to define a function that generates these reciprocal space points, either in the form of a path, or in a two-dimensional grid, and another that computes the eigenvalues and eigenvectors of our Hamiltonian for each **k** (see Appendix C). The first is easily accomplished. For the second, we start by taking advantages of the Julia's multi-threading options, and send our **k** points to be diagonalized in different processors, so that we can save time when running heavy code. The diagonalization of sparse matrices is performed with the KrylovKit.jl, package for Julia, [64], and its function `eigsolve()`. This last function outputs a set number of eigenvalues, closest to a α of our choosing, and a subset of a Krylov subspace composed of their respective eigenvectors, via Arnoldi iteration. We demand the original subspace to have twice the number of desired eigenvalues. In the same function, we compute the bands visibilities for every considered **k**.

Finally, we plot the bands, along a path and superimpose in them the same band structure with line width controlled by the visibility, or in a constant energy plot, using the `heatmap()` function from Julia's package Plots.jl, [65].

Chapter 4

Results

We arrive at our final destination, the energy bands' visibilities. In this chapter, we present our results and discuss them.

We show the ARPES visibility in terms of the $Q_\perp$ parameter, in the first BZ and along extended paths, for the first graphene based systems, the SLG, BLG and TLG. We also show CEPs, for these.

In the TMDs, the two models [40, 41], using the parameters from [40–42] are plotted and the ARPES visibility compared.

Finally, we discuss the tBLG and tTLG's visibility for large, intermediate and low angles of twist.

Before we proceed, let us recap some fundamental results.

We have established that the intensity of the ARPES electronic beam is given by

$$\boxed{I_{ARPES}(E_f, \mathbf{x}) \propto \sum_{n' \in \Lambda} f(E_{n'} - \mu) |M_{fn'}|^2 \delta(E_f - E_{n'} - \hbar\omega)} \tag{2.27}$$

where E_f, $E_{n'}$ and ω are the photoemitted electron energy, the electronic energy of the crystal bound state n' and the photon frequency, respectively, Λ represents the crystal bound states set, $f(E)$ is the Fermi-Dirac distribution, and $|M_{fn'}|$ is a matrix element proportional to

$$\boxed{|M_{fn'}|^2 \propto \sum_{\mathbf{G}} \left| \sum_{\alpha} e^{-i(\mathbf{p}^\perp - \mathbf{q}^\perp)\cdot\delta_\alpha} a_\alpha^n (\mathbf{p}^\parallel - \mathbf{q}^\parallel) f_\alpha(\mathbf{p} - \mathbf{q}) \right|^2 \delta_{\mathbf{p}^\parallel - \mathbf{q}^\parallel, \mathbf{k}+\mathbf{G}}} \tag{2.34}$$

$\mathbf{p}$ and $\mathbf{q}$ being the photoemitted electron momentum and incident photon momentum, respectively, $\mathbf{G}$ a reciprocal lattice vector, α the orbitals, n the band, and $f_\alpha(\mathbf{p})$ the atomic

form factor. The $\perp$ and $\parallel$ superscripts denote the momenta orientation with respect to the crystal surface.

We have also mentioned that, for a periodic lattice with N sites at $\mathbf{R}$, a Bloch state given by the linear combination of the atomic orbitals,

$$|\psi_{\mathbf{k},n}\rangle = \frac{1}{\sqrt{N}} \sum_{\mathbf{R},\alpha} e^{i\mathbf{k}\cdot(\mathbf{R}+\delta_\alpha)} a_\alpha^n(\mathbf{k}) \, |\mathbf{R},\alpha\rangle \,, \tag{2.28}$$

has coefficients $a_\alpha^n(\mathbf{k})$ that satisfy the property,

$$\boxed{a_\alpha^n(\mathbf{k}) = e^{i\mathbf{G}\cdot\delta_\alpha} a_\alpha^n(\mathbf{k}+\mathbf{G})} \tag{2.45}$$

meaning that the matrix element (2.34) is periodic. Its periodicity, however, depends on the system.

Furthermore, we note that what is plotted as visibility in the sections that follow, is not actually what is seen when the experiment takes place. In our graphs, we show the bands that can be seen, i.e., we plot the $|M_{fn'}|^2$. For a state to be seen in the experiment, one still has to take in consideration the remaining functions in equation (2.27), namely the Fermi-Dirac distribution.

4.1 Single Layer Graphene

We start off with the simplest system, the SLG. For graphene based systems, we compute the ARPES visibility for a p_z orbital, so the atomic form factor is given approximately by a Dirac delta, neglecting the radial and azimuthal parts.

The bands' visibility for a path in the first BZ is shown in Figure 4.1.1a. In it, we express the ARPES visibility through the thickness of the yellow line superimposing the energy bands. The more visible a band is, the thicker is the yellow line drew in it. If this line is absent, then the band is not visible in those points.

This is easier understood discussing the present example. Along this path, we observe that the majority of band visibility is in the valence band. The positive energy band can be somewhat seen near Γ and between M and K but, from the apparent thickness of these lines, the lower band is much more prevalent, and can be observed in its entirety for this path.

However, remembering equation (2.45), we know this is not the whole story. Following a path along a direction in the reciprocal space, one may see that $a_\alpha^n(\mathbf{k}) = a_\alpha^n(\mathbf{k}+\mathbf{G})$ is

achieved only for a $\mathbf{G}$ that satisfies, $\mathbf{G} \cdot \delta_\alpha = 2\pi m$, for $m \in \mathbb{Z}$ and all α. Since, the contributions of these coefficients are all being summed inside an absolute value, the visibility completes its cycle only when this condition is met for every coefficient. Although this can bring long visibility periodicities (or even not be periodic for other form factors that do not neglect the radial part), in the SLG it depends only on the δ sublattice vector, since $\delta_A = \mathbf{0}$.

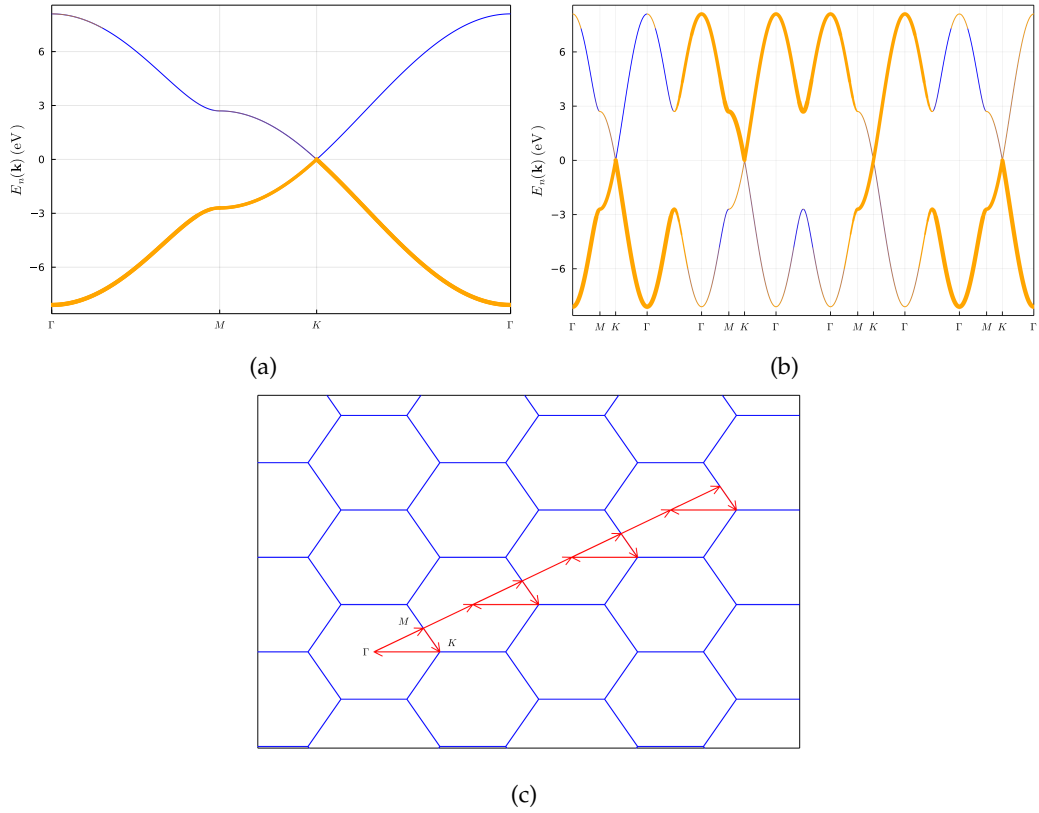

FIGURE 4.1.1: SLG band structure (in blue) and visibility (in yellow) along the path $\Gamma - M - K - \Gamma$ in the first BZ in (a) and along the path drew in (c), in (b). In (c) we show the path in reciprocal space taken in (b).

Consider the path in Figure 4.1.1c. It repeats the path in Figure 4.1.1a over four unit cells. On the last cell, we are at $\mathbf{G} = 3\mathbf{b}_1$, which under the dot product with δ is $3\mathbf{b}_1 \cdot \delta = 2\pi$. Therefore, on this point, the $a^n_\alpha(\mathbf{k}) = a^n_\alpha(\mathbf{k} + \mathbf{G})$ is satisfied for both $\alpha = A, B$, and the visibility ends where it started. This is evident in Figure 4.1.1b. On the first $\Gamma - M - K - \Gamma$, on the left, we have the same as in Figure 4.1.1a. However, along the remaining plot, the band structure is repeated, but every time with a different visibility. Eventually every point is seen.

This periodicity in the ARPES signal is only dependent on the lattice, thus, for graphene based systems, that share the same unit cell, all have the same behavior.

4.2 Bilayer Graphene

The BLG shows an ARPES visibility similar to the SLG, as can be seen from Figure 4.2.1a, focusing on the inner bands. The valence band is evident in every point, however, the outer bands are mostly hidden, showing only the upper band some visibility near K.

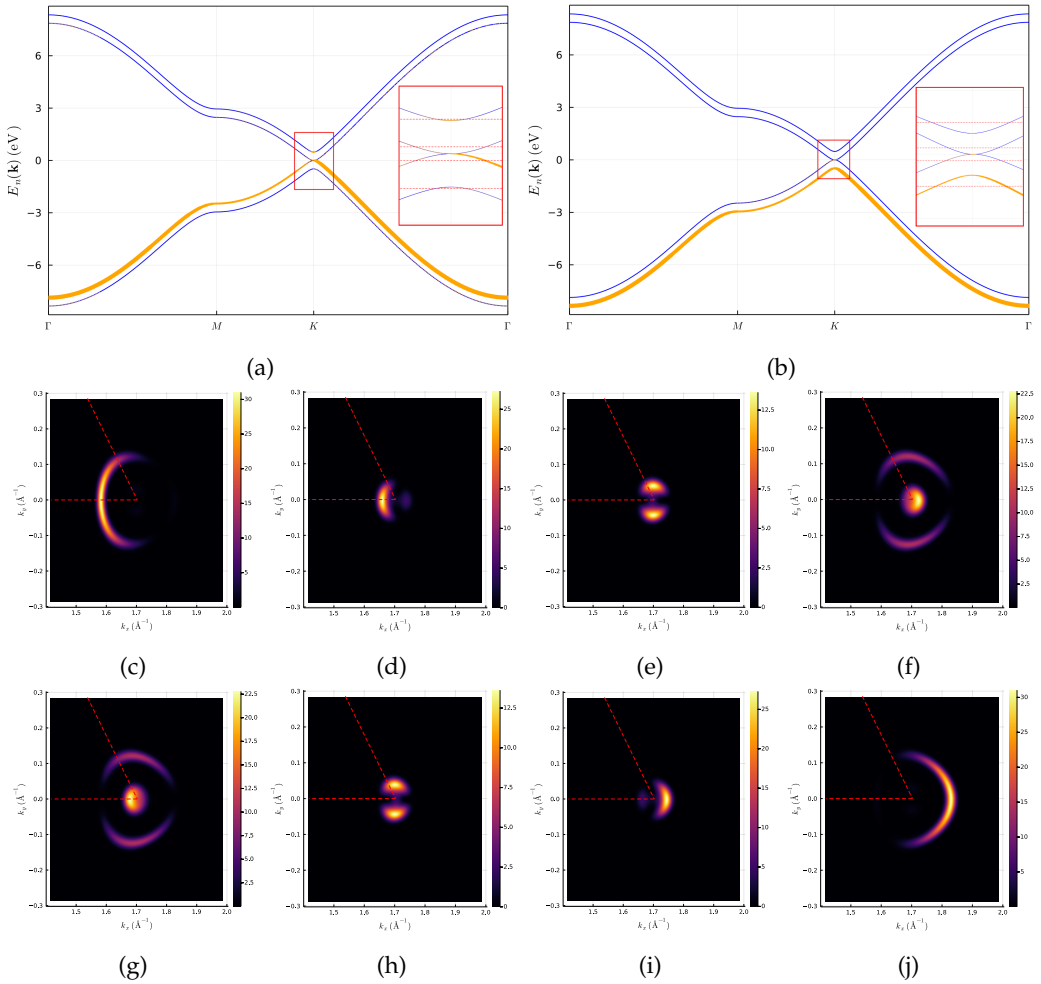

FIGURE 4.2.1: BLG band structures (in blue) and visibilities (in yellow) along the path $\Gamma - M - K - \Gamma$ for $Q_\perp = 0$ in (a) and $Q_\perp = \pi/d_\perp$ in (b). A plot zooming on the dispersion near K is shown in both. In these, we draw four constant energies red dashed lines, and show, in (c-f) for $Q_\perp = 0$, and in (g-j) for $Q_\perp = \pi/d_\perp$, the CEPs. The (c) and (g) plots are for energy $\varepsilon = -0.5$ eV, the (d) and (h) $\varepsilon = -0.1$ eV, (e) and (i) for $\varepsilon = 0.1$ eV and $\varepsilon = 0.5$ eV for (f) and (j). Here, the red dashed lines mark the path taken in plots (a) and (b).

Furthermore, inside this figure is a zoomed plot of the dispersion near the Dirac point. In it, we confirm the accessibility of these bands, and mark in red four constant energies, $\varepsilon = -0.5$ eV, $\varepsilon = -0.1$ eV, $\varepsilon = 0.1$ eV and $\varepsilon = 0.5$ eV. Each of these slices is shown in the CEPs from Figures 4.2.1c, 4.2.1d, 4.2.1e and 4.2.1f, respectively, for further insight. Figures 4.2.1c and 4.2.1d show that the valence band is well seen around the Dirac point, and from Figure 4.2.1e we notice that the conduction band is hidden only for $k_y = 0$. Nevertheless,

it loses its intensity, as we can gather from Figure 4.2.1f, where only a tiny dot is shown due to the emergence of the upper band. These results are consistent with [66].

The rest of the spectrum is seen in Figure 4.2.2a. This profile is again alike to the SLG, but notice that the lower and conduction bands are never visible, even though it completes a period at the last Γ. The reason why these bands appear hidden from the experiment is because, with the stacking of another layer, we have vectors with a non-null component perpendicular to the material surface, $d_\perp$. Looking at equation (2.34), we see that $\mathbf{p}^\perp - \mathbf{q}^\perp$, which we will denote as $\mathbf{Q}^\perp = \mathbf{p}^\perp - \mathbf{q}^\perp$, can no longer be ignored. Because it is in an exponential, it introduces another periodicity. Vectors distanced from $\mathbf{Q}^\perp = 2\pi m/d_\perp \hat{\mathbf{z}}$, for $m \in \mathbb{Z}$, have the same visibility.

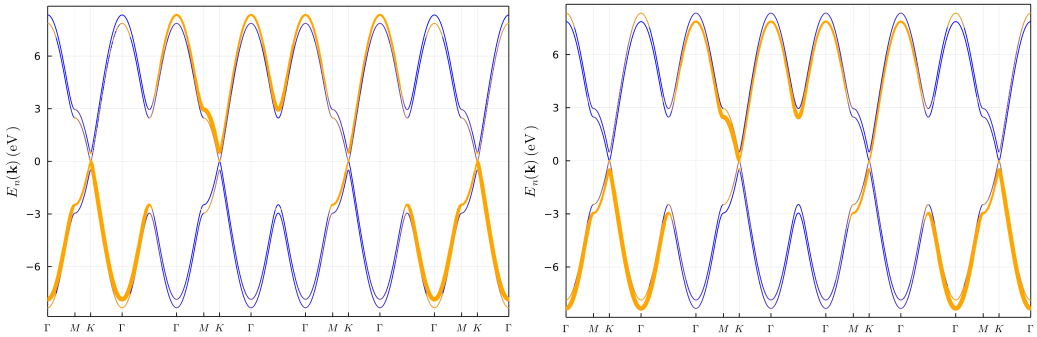

(a) (b)

FIGURE 4.2.2: BLG band structures (in blue) and visibilities (in yellow) along the path in Figure 4.1.1c, for $Q_\perp = 0$ in (a) and $Q_\perp = \pi/d_\perp$ in (b).

In Figure 4.2.1b, the non-null $Q_\perp$ (z component of $\mathbf{Q}^\perp$) becomes apparent. The plot has $Q_\perp = \pi/d_\perp$, i.e., is in the opposite phase of Figure 4.2.1a. The prevalent band is now the lower one, and the conduction and upper bands are mostly hidden, except for a small region near K in the valence band. Moreover, in the CEPs for $Q_\perp = \pi/d_\perp$ in Figures 4.2.1g, 4.2.1h, 4.2.1i and 4.2.1j, the bands seem almost inverted compared to $Q_\perp = 0$, evidencing that they are in fact in an opposite phase between layers.

From Figure 4.2.2b the bands until here hidden are the ones showing, while the valence and upper bands disappear altogether.

Considering a distance dependent hopping slightly modifies the electronic band structure, breaking electron-hole symmetry, but the ARPES physics is the same. As discussed previously, the positive energy bands tend to merge while the negative ones grow apart. Nevertheless, the most visible bands are the same, for each $Q_\perp$, as seen in Figures 4.2.3a and 4.2.3b. This band behavior is observed in the CEPs as well. For the positive bands in Figures 4.2.3f, 4.2.3j, one may observe the conduction band appears for energies closer

to zero. This is also shown in Figures 4.2.3c, 4.2.3g, from where we see that the bands actually move closer before diverging.

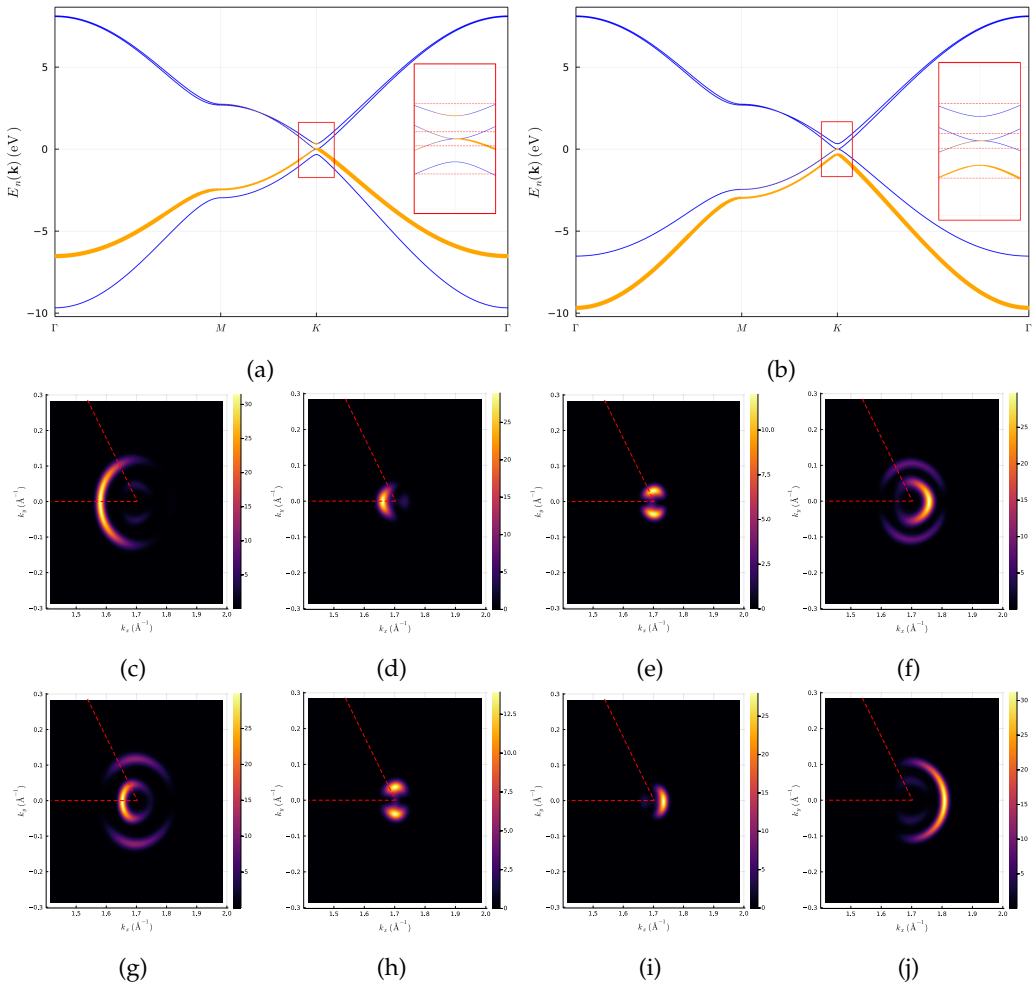

FIGURE 4.2.3: BLG band structures (in blue), for a distance dependent hopping, and visibilities (in yellow) along the path $\Gamma - M - K - \Gamma$ for $Q_\perp = 0$ in (a) and $Q_\perp = \pi/d_\perp$ in (b). A plot zooming on the dispersion near K is shown in both. In these, we draw four constant energies red dashed lines, and show, in (c-f) for $Q_\perp = 0$, and in (g-j) for $Q_\perp = \pi/d_\perp$, the CEPs. The (c) and (g) plots are for energy $\varepsilon = -0.5$ eV, the (d) and (h) $\varepsilon = -0.1$ eV, (e) and (i) for $\varepsilon = 0.1$ eV and $\varepsilon = 0.5$ eV for (f) and (j). Here, the red dashed lines mark the path taken in plots (a) and (b).

4.3 Trilayer Graphene

The mirror TLG band structure is can be understood as a superposition of both the SLG and BLG dispersions. Two of its bands have the linear slope, characteristic of the SLG, and four of them show the BLG's parabolic behavior. Therefore, it does not come as a total surprise that the visibilities follow the same trend as before.

The visibility is shown in Figures 4.3.1a, 4.3.1b and 4.3.1c. We observe that, depending on the $Q_\perp$, the visibility oscillates between these two systems' visibilities. In Figure 4.3.1a, for $Q_\perp = 0$, the seen bands are the same as in Figure 4.2.1a, for the BLG. Increasing this parameter, the negative middle band starts to show, and the highest valence band to fade. Reaching $Q_\perp = \pi/2d_\perp$, the latter disappears, and the only prevalent energies are those of the negative middle band, or the SLG band. This is shown in Figure 4.3.1b. If we keep increasing this parameter, now the SLG-like band is seen less and less, and the lower band gets gradually more intense. We reach $Q_\perp = \pi/d_\perp$ in Figure 4.3.1c, the BLG's opposite phase. The only visible band is the lower band, as we have seen in the BLG, in Figure 4.2.1b.

The same picture emerges from the CEPs, where the plots with $Q_\perp = 0$ and $Q_\perp = \pi/2d_\perp$ have identical visibilities. For $Q_\perp = \pi/d_\perp$, the dominant band is the SLG-like band, confirming our discussion. The initial configuration is regained when $Q_\perp = 2\pi/d_\perp$.

This means that, despite having an extra layer, the periodicity is still the same. That owes its reason to the exponential in equation (2.34). To complete the cycle, every dot product must come to an integer of 2π. Since the third layer's sites have twice the frequency than the middle layer's sites have, the overall period is unchanged, ruled by the separation between layers, $d_\perp$.

As in the BLG, the plots resultant of a distance dependent hopping have slightly different dispersions but, regarding the ARPES band information, the results are qualitatively the same. This is shown in Figure 4.3.2, where, despite the merging of the positive bands and diverging of the negative, the visibility agrees with the simpler nearest-neighbor case.

The CEPs provide the same insight, and in Figures 4.3.2h and 4.3.2h it is evident the merging of the bands, for lower and upper bands appear for energies closer to zero.

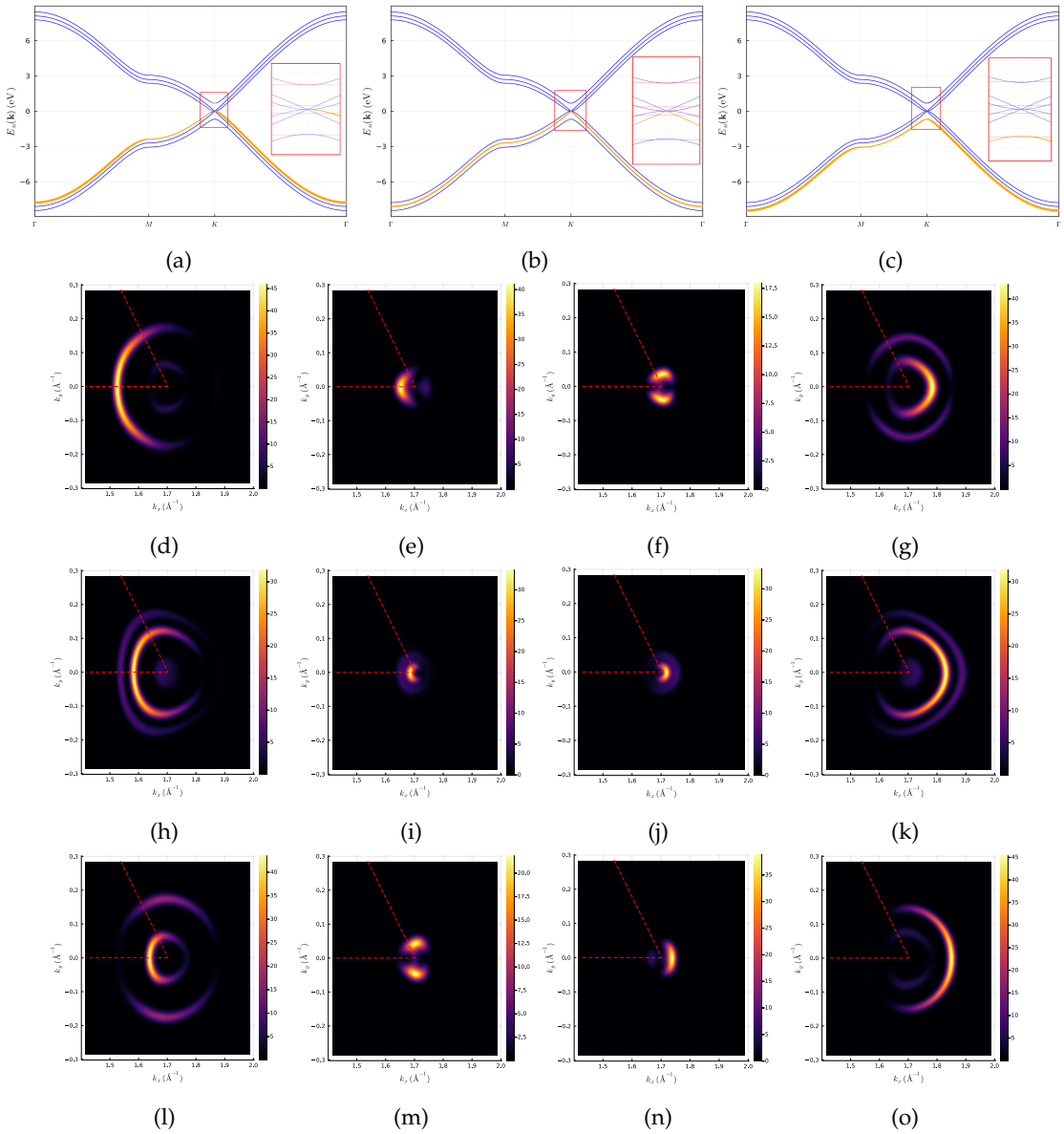

FIGURE 4.3.1: TLG band structure (in blue) and visibility (in yellow) along the path $\Gamma - M - K - \Gamma$ for $Q_\perp = 0$, in (a), $Q_\perp = \pi/2d_\perp$ in (b) and $Q_\perp = \pi/d_\perp$ in (c). A plot zooming on the dispersion near K is also shown, where four red dashed lines are drawn. These lines show the energies for which the CEPs are made, in (d-o).These are $\varepsilon = -0.7$ eV in (d), (h) and (l), $\varepsilon = -0.1$ eV in (e), (i) and (m), $\varepsilon = 0.1$ eV in (f), (j) and (n) and $\varepsilon = 0.7$ eV in (g), (k) and (o). Here, the red dashed lines mark the path taken in (a-c).

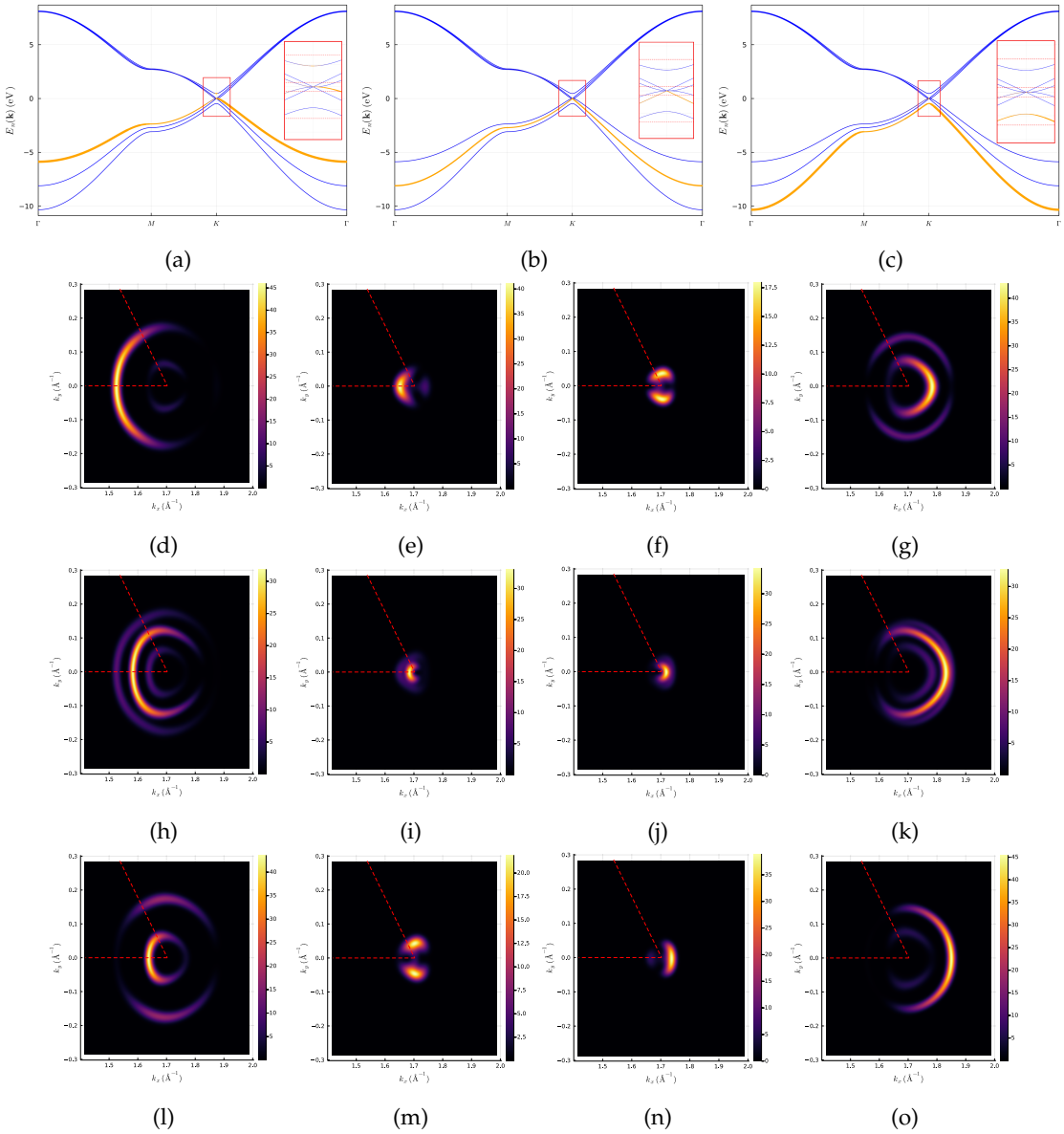

FIGURE 4.3.2: TLG band structure (in blue), for a distance dependent hopping, and visibility (in yellow) along the path $\Gamma - M - K - \Gamma$ for $Q_\perp = 0$, in (a), $Q_\perp = \pi/2d_\perp$ in (b) and $Q_\perp = \pi/d_\perp$ in (c). A plot zooming on the dispersion near K is also shown, where four red dashed lines are drawn. These lines show the energies for which the CEPs are made, in (d-o).These are $\varepsilon = -0.7$ eV in (d), (h) and (l), $\varepsilon = -0.1$ eV in (e), (i) and (m), $\varepsilon = 0.1$ eV in (f), (j) and (n) and $\varepsilon = 0.7$ eV in (g), (k) and (o). Here, the red dashed lines mark the path taken in (a-c).

4.4 Transition Metal Dichalcogenide Monolayers

As in the models section 3.4, we present three band structures for the same system. Two of them built from the same Cappelluti model studied in [40], but with different parameters [40, 42], Figures 4.4.1a, 4.4.1b, 4.4.1d and 4.4.1e, and the other using the Kaxiras model [41], shown in Figures 4.4.1c and 4.4.1f for $Q_\perp = 0$, $Q_\perp = 2\pi/u$, respectively.

As explained, the MoS_2 lattice has three sublattices, two with p_x, p_y and p_z p-orbitals, and one with d_{z^2}, $d_{x^2-z^2}$, d_{xy}, d_{xz} and d_{yz} d-orbitals. To model these, we no longer consider the simple Dirac delta, as in graphene. There, since the orbitals are all p_z orbitals, we could safely neglect the latitudinal part, since it only introduced a constant in the visibility. The azimuthal part we did not neglect, but for graphene it is 1. However, here we have the contribution of orbitals dependent of x, y and z, so dispensing these parts would produce wrong results. The orbitals are modeled by the correspondent real spherical harmonics. Thus, neglecting the radial part and letting it absorb the spherical harmonic constants, the atomic form factor may be written as the product between a latitudinal and an azimuthal function,

$$f_\alpha(\mathbf{p}) = f_\alpha^\theta(\mathbf{p}) f_\alpha^\phi(\mathbf{p}), \tag{4.4.1}$$

where

$$\begin{gathered} f^\theta_{p_{x/y}}(\mathbf{k}, Q_\perp) = \frac{|\mathbf{k}|}{\sqrt{|\mathbf{k}|^2 + Q_\perp^2}}, \quad f^\theta_{p_z}(\mathbf{k}, Q_\perp) = \frac{Q_\perp}{\sqrt{|\mathbf{k}|^2 + Q_\perp^2}}, \\ f^\theta_{d_{xy}}(\mathbf{k}, Q_\perp) = \frac{|\mathbf{k}|^2}{|\mathbf{k}|^2 + Q_\perp^2}, \quad f^\theta_{d_{xz}}(\mathbf{k}, Q_\perp) = \frac{|\mathbf{k}| Q_\perp}{|\mathbf{k}|^2 + Q_\perp^2}, \quad f^\theta_{d_{yz}}(\mathbf{k}, Q_\perp) = f^\theta_{d_{xz}}(\mathbf{k}, Q_\perp) \\ f^\theta_{d_{x^2}}(\mathbf{k}, Q_\perp) = f^\theta_{d_{xy}}(\mathbf{k}, Q_\perp), \quad f^\theta_{d_{z^2}}(\mathbf{k}, Q_\perp) = \frac{3Q_\perp^2}{|\mathbf{k}|^2 + Q_\perp^2} - 1, \end{gathered} \tag{4.4.2}$$

and

$$\begin{gathered} f^\phi_{p_x}(\mathbf{k}, Q_\perp) = \frac{k_x}{|\mathbf{k}|} \quad f^\phi_{p_y}(\mathbf{k}, Q_\perp) = \frac{k_y}{|\mathbf{k}|} \quad f^\phi_{p_z}(\mathbf{k}, Q_\perp) = 1 \\ f^\phi_{d_{xy}}(\mathbf{k}, Q_\perp) = \frac{2k_x k_y}{|\mathbf{k}|^2} \quad f^\phi_{d_{xz}}(\mathbf{k}, Q_\perp) = f^\phi_{p_x}(\mathbf{k}, Q_\perp) \quad f^\phi_{d_{yz}}(\mathbf{k}, Q_\perp) = f^\phi_{p_y}(\mathbf{k}, Q_\perp) \\ f^\phi_{d_{x^2}}(\mathbf{k}, Q_\perp) = \frac{k_x^2 - k_y^2}{|\mathbf{k}|^2} \quad f^\phi_{d_{z^2}}(\mathbf{k}, Q_\perp) = 1. \end{gathered} \tag{4.4.3}$$

The plots in Figures 4.4.1a and 4.4.1b are in better agreement with each other than with the one in Figure 4.4.1c, as the valence and conduction bands show similar ARPES visibility. Still, they all agree in the visibility for the K point in these two bands. This is

expected, since the models from [40] are optimized for the highest valence band and lowest conduction band. However, the other bands are not so well described. The plot from the parameters [42] is, even so, closer to the reality, being a refined model of the original. On the other hand, the Kaxiras model is more trustworthy overall since its parameters are come from density function theory methods.

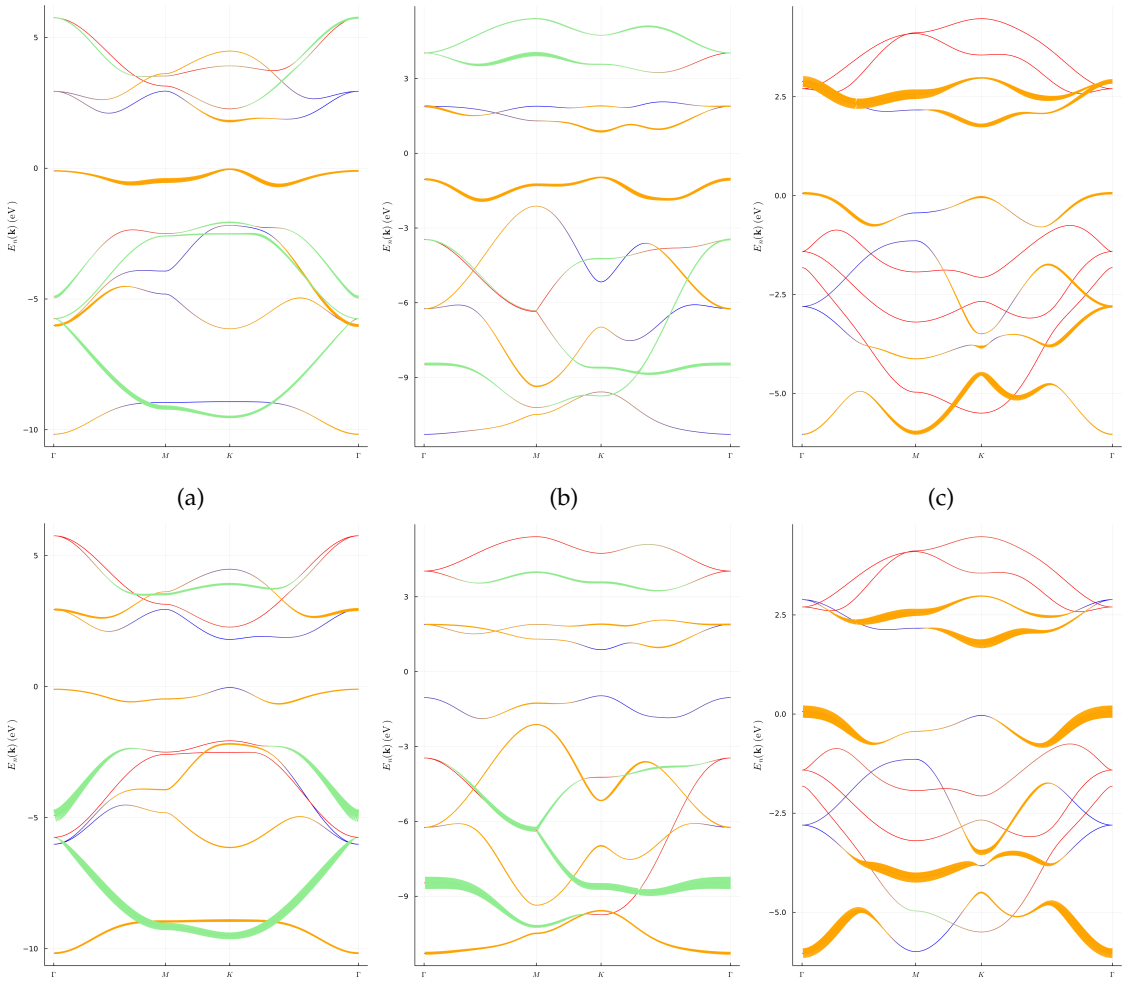

FIGURE 4.4.1: TMDs band structures and visibilities for the parameters listed in Table 3.4.1 for (a), (b), (d) and (e), and in Table D.0.1 for (c) and (f). In blue, we plot the even bands and in red the odd. To better distinguish the band visibilities plotted for $Q_\perp = 0$ in (a-c) and $Q_\perp = 2\pi/u$ in (d-f), these are colored yellow for the even bands and green for the odd.

Regarding the three subsequent graphs in Figures 4.4.1d, 4.4.1e and 4.4.1f, according to our prior discussion concerning the periodicity of $Q_\perp$, once they are plotted for $Q_\perp = 2\pi/u$, and the separation between layers is u, the band visibilities should agree with the visibilities for $Q_\perp = 0$. The reason for such not happening lies in the atomic form factor, that is not so simple here.

The bands are modulated by these factors, making it harder to predict the periodicity of these systems.

In Figures 4.4.1d and 4.4.1e, the odd bands are much more visible than for $Q_\perp = 0$, and the even bands seem hidden comparing to the prior case. However, the model in Figure 4.4.1f seems more agreeable with its phase at $Q_\perp = 0$. The intensity of the even bands varies, particularly at the corners of the valence and the band above the conduction bands, and in the lower band, where the visibility shifted from near the K point to near the Γ point.

4.5 Twisted Bilayer Graphene

In this section, we begin our discussion of the ARPES visibility in twisted graphene, namely, in tBLG.

4.5.1 Large and Intermediate Angles

We ease in our study of the ARPES visibility for the tBLG by starting with the largest possible commensurate angle, $\theta \simeq 22°$, according to equation (3.5.4). Letting $Q_\perp$ take the values $Q_\perp = 0$, $Q_\perp = \pi/2d_\perp$ and $Q_\perp = \pi/d_\perp$, and taking the path in Figure 3.5.3c, we produce the plots in Figures 4.5.1a, 4.5.1b and 4.5.1c. The results seem to indicate that the cones are amongst the features of the bands most consistently observed, despite the variation of $Q_\perp$. Actually, they are so well seen, that the ARPES signal for $\theta \simeq 22°$ is identical to the visibility shown for the system with decoupled layers. From Figure 4.5.2b we confirm that this is true. In blue and green, we signalize the visibilities of each band, that are seen independently in each cone and superimpose with each other in the $\Gamma_m - M_m - \Gamma$ path. (It actually seems from our plots that the top layer is the only visible band in this path. However, this is an artifact of how the visibilities were plotted. Since they are passing through a path equidistant to both cones, there is no reason for one layer to be more visible than the other.) Furthermore, noticing Figure 4.5.2a and comparing it to 4.5.2b, we see again what we saw before for the simpler system of the diatomic chain, in section 2.3. For the same decoupled system, the visible bands are the same, despite the band structure, that depends on the choice of the unit cell. However, being the ARPES signal an experimental quantity, it can not vary accordingly to the chosen parametrization.

The resemblance of these decoupled systems with the ones with larger angle indicates that for these angles, the interlayer coupling is weaker.

Moreover, the visible bands oscillate over the same energies, showing a somewhat resemblance to the opposite phase effect between $Q_\perp = 0$ and $Q_\perp = \pi/d_\perp$, like we found in our systems without twist. The scenario with $Q_\perp = \pi/2d_\perp$ seems to be a hybrid state between the two more definitive ones. However, the remaining bands seem inaccessible, at least in this path. Even so, once there is a very large number of orbitals contributing, it is difficult to predict every output, and a more extensive search might prove the contrary.

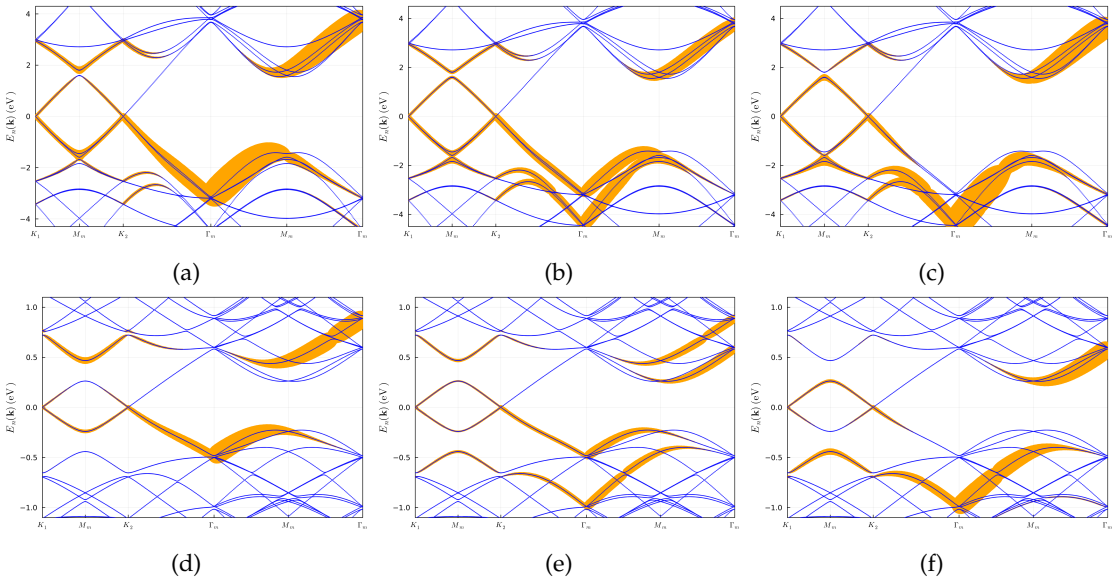

FIGURE 4.5.1: tBLG band structure (in blue) and visibility (in yellow) for $\theta \simeq 22°$in (a-c) and 4°in (d-f), along the path 3.5.3c. The $Q_\perp$ is $Q_\perp = 0$ in (a) and (d), $Q_\perp = \pi/2d_\perp$ in (b) and (e), and $Q_\perp = \pi/d_\perp$ in (c) and (f).

The intermediate angle $\theta \simeq 4°$ shows that the visibility of the cones, near the now more developed gaps, begins to fade. The fading is not the same for all $Q_\perp$ though. In Figure 4.5.1d, for $Q_\perp = 0$, the conduction band starts to lose visibility, while it is the valence band that starts to disappear at $Q_\perp = 2\pi/d_\perp$, in Figure 4.5.1f. When $Q_\perp = \pi/2d_\perp$, however, both the valence and conduction bands seem less visible near the gaps.

4.5.2 Small Angles

For the small angles, we study $\theta \simeq 1.8°$ and $\theta \simeq 1.08°$. In Figures 4.5.3a, 4.5.3b and 4.5.3c the band structure and visibility are represented, as usual, to increasing values of $Q_\perp$. In all of them, the bands descendant from the Dirac cones are very near to be completely hidden.

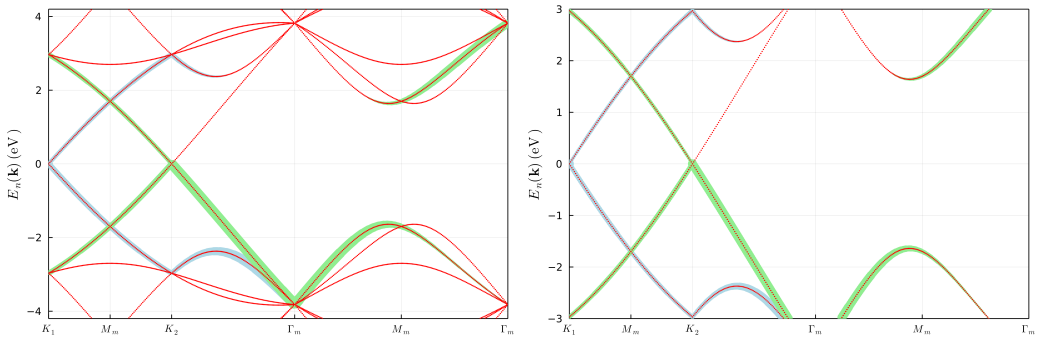

(a) (b)

FIGURE 4.5.2: Decoupled system band structure (in red) and visibility for $\theta \simeq 22°$, along the path 3.5.3c. In (a) the system considers the same supercell as the tBLG for this angle, and in (b) the usual graphene unit cell is used.

The flat bands are finally obtained in Figures 4.5.3d, 4.5.3e and 4.5.3f. The plot is laid in the same way, with $Q_\perp$ increasing to the right. From it, it may be observed that the plot with $Q_\perp = 0$ appears to favor the positive bands, while the plot with $Q_\perp = \pi/d_\perp$ favors the negative. Besides that, each of them has a very visible band near the first and second Γ_m, respectively. The plot with $Q_\perp = \pi/2d_\perp$, once again, seems a hybrid of these two, not showing any band so evidently, but showing the bands from both cases nonetheless. However, apart from the points near Γ_m and the bands at the top/bottom, the band structure is mostly hidden in these plots. Even the flat bands seem to disappear.

For more insight on why this is happening, we plot, in Figure 4.5.4, various band structures modeled by the gradual turning off of the interlayer coupling. This is achieved by expressing the interlayer hopping in terms of an additional constant, $t_\perp \to \lambda t_\perp$. Therefore, when we consider full coupling, we have $\lambda = 1$, and as λ goes to zero, the bands decouple.

Comparing these results with the other band structures and visibilities, the plots with varying interlayer coupling have similar profiles with those for larger angles. This further confirms our assessment that bands with larger angles have weaker coupling. Moreover, we have the chance to observe the effects the coupling has in the flat band visibility. For $\lambda = 0.1$, the plots are very alike to the ones found in section 4.5.1, for $\theta \simeq 22°$. But as we turn it on, the cones begin to fade, leaving for $\lambda = 1$ the flat unseen. Nevertheless, the valence band for $Q_\perp = 0$ looks like is going against this demise, but in the flat band regime, it connects with the band above the conduction band, contributing to the flat band only at their intersection at the first Γ_m. For $Q_\perp = \pi/2d_\perp$ and $Q_\perp = \pi/d_\perp$, the flat band

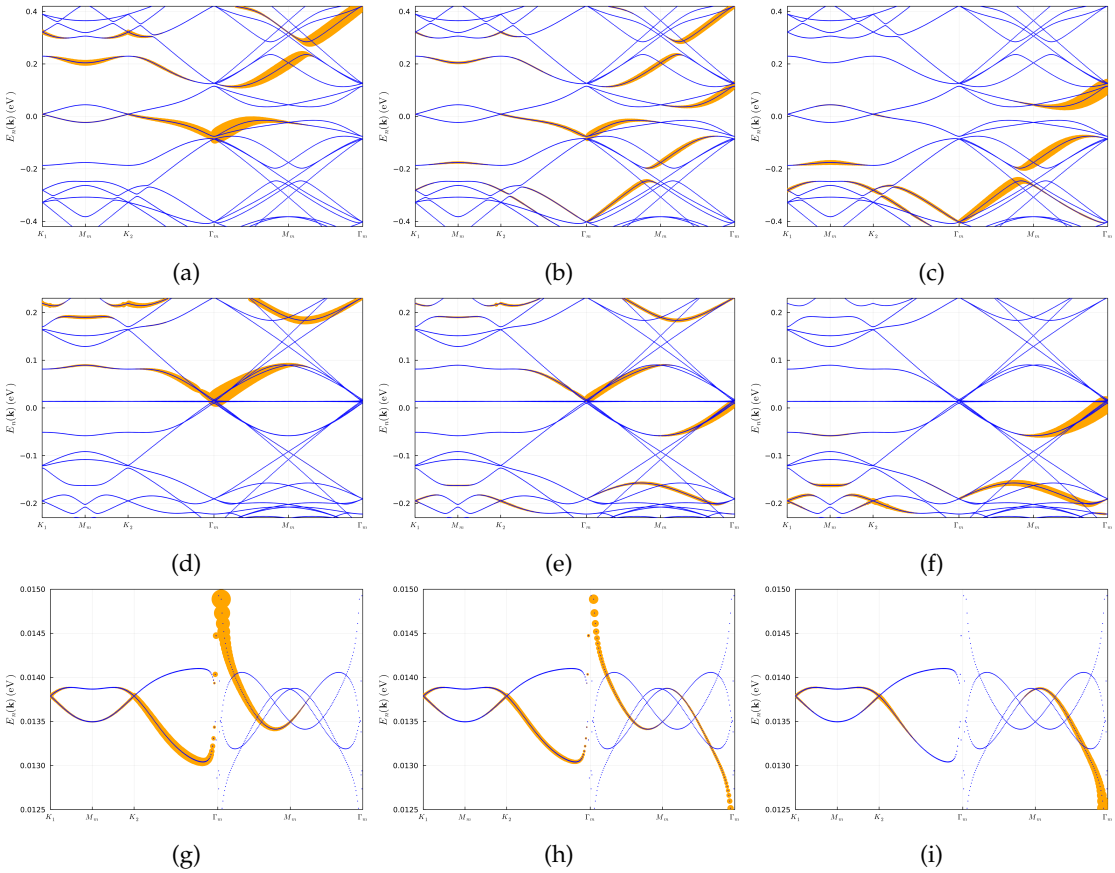

FIGURE 4.5.3: tBLG band structure (in blue) and visibility (in yellow) for $\theta \simeq 1.8°$ in (a-c) and $\theta \simeq 1°$ in (d-f), along the path 3.5.3c. In (g-i), we zoom in on the flat band, increasing its visibility by a factor of 10. The $Q_\perp$ is $Q_\perp = 0$ in (a), (d), (g), $Q_\perp = \pi/2d_\perp$ in (b), (e), (h), and $Q_\perp = \pi/d_\perp$ in (c), (f) and (i).

is joined at the second Γ_m by the other prominent band, but their superposition is only at that point as well.

This means that, in the sum of equation (2.34), the eigenvectors coefficients for this band interfere destructively, for the vast majority of $\mathbf{k}$ points and for the measured values of $Q_\perp$.

However, from Figures 4.5.3g, 4.5.3h and 4.5.3i, we gather that destructive interference is not total. Increasing the output of the visibility by a factor of 10, we manage to observe a very small visibility in comparison to the other bands. Furthermore, even with this boost in the ARPES intensity, there are branches that remain to be seen. They may be reached for other configurations of the parameter $Q_\perp$, though most of them are unlikely, or by taking in consideration another path in reciprocal space.

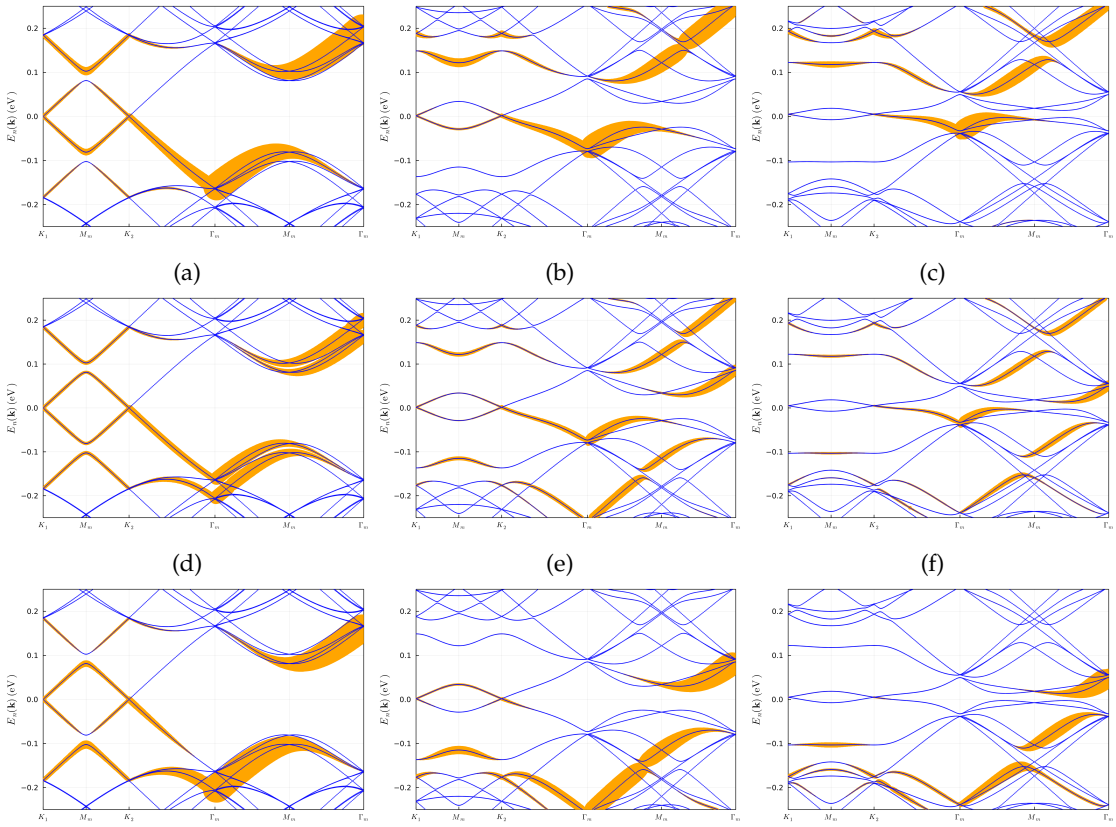

FIGURE 4.5.4: tBLG band structure (in blue) and visibility (in yellow) for $\theta \simeq 1°$along the path 3.5.3c, for varying interlayer coupling. For (a-c) we have $\mathbf{Q}_\perp = 0$, $\mathbf{Q}_\perp = \pi/2d_\perp$ in (d-f) and $\mathbf{Q}_\perp = \pi/d_\perp$ for (g-i). The coupling parameter, λ, is $\lambda = 0.1$ in (a), (d) and (g), $\lambda = 0.5$ in (b), (e) and (h), and $\lambda = 0.7$ in (c), (f) and (i).

4.6 Twisted Trilayer Graphene

We switch our discussion to the tTLG. Just like the TLG shows properties of the SLG and the BLG, the tTLG demonstrates an ARPES signal remembering of both, as we see now.

4.6.1 Large and Intermediate Angles

Returning to the large angles, we consider again $\theta \simeq 22°$, now for the tTLG. This time, as well, we notice that this system shows some resemblance with the decoupled system. Actually, looking at the plots for $Q_\perp = \pi/2d_\perp$ in Figure 4.6.1 one may see the complete SLG band, from the bottom layer, visible as in the decoupled system of Figure 4.5.2. The reason for this is that the Dirac cones are consequent of the antisymmetric combination of the first and third layers that is decoupled from the middle layer [37], as explained in

section 3.6. Since these layers are aligned, without rotation, the signal they produce in the cone of the rotated layer is weak, and possibly non-existent.

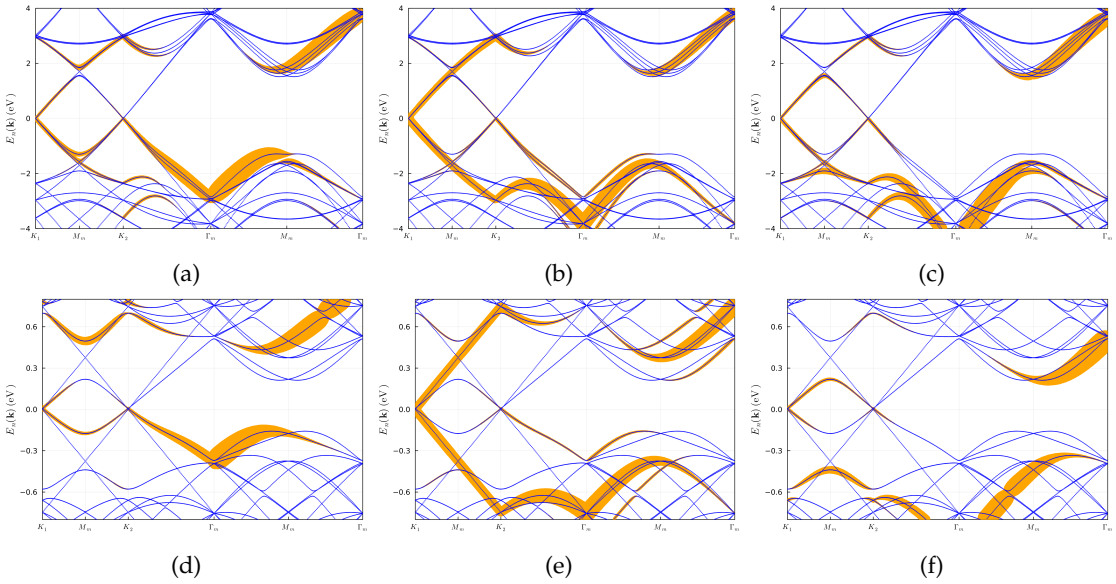

FIGURE 4.6.1: tTLG band structure (in blue) and visibility (in yellow) for $\theta \simeq 22°$in (a-c) and 4°in (d-f), along the path 3.5.3c. The $Q_\perp$ is $Q_\perp = 0$ in (a) and (d), $Q_\perp = \pi/2d_\perp$ in (b) and (e), and $Q_\perp = \pi/d_\perp$ in (c) and (f).

As for the others values of $Q_\perp$, $Q_\perp = 0$ and $Q_\perp = \pi/d_\perp$ still seem like opposite phases, which is understandable given that $Q_\perp = 2\pi/d_\perp$ remains as the period in which the bands return to the visibility they had at $Q_\perp = 0$. Similarly to the tBLG, there are two bands diverging from each Γ_m carrying a lot of visibility, one for positive and the other for negative energies, and the cones start to disappear near the gaps, one for positive energies and the other in negative energies as well.

Picking the same middle angle as well as in tBLG, $\theta \simeq 4°$, we plot its band structure and visibility in Figure 4.5.1. For $Q_\perp = 0$ and $Q_\perp = \pi/d_\perp$, it shows the disappearing of the cones and the prevalence of the same positive and negative energy bands.

However, for $Q_\perp = \pi/2d_\perp$, the most visible Dirac cone seems unaffected by the decreasing of the angle. This is expected, as the cones are produced by a combination of states that are decoupled from the middle layer and the bottom and top layers share a very weak coupling, [37].

4.6.2 Small Angles

In this section, we study the tTLG for the small angles $\theta \simeq 1.8°$ and $\theta \simeq 1.5°$.

In concern to the system with $\theta \simeq 1.8°$, its band structure and visibility is shown in Figures 4.6.2a, 4.6.2b and 4.6.2c. In these plots, the bands are very near to the flat band regime, being the central bands already very flat, showing no visibility apart from in the points Γ_m in Figures 4.6.2a and 4.6.2c, and in the cone in Figure 4.6.2b.

The plots shown in Figure 4.6.2 share some similarities with the tBLG case. Actually, if not for the Dirac cones, both plots would be practically the same. For $Q_\perp = \pi/2d_\perp$, they are, however, very noticeable, manifesting the same spectrum and visibility as they would in the decoupled system. Regarding the remaining energies, at $Q_\perp = 0$, positive bands are prevalent and, for $Q_\perp = \pi/d_\perp$, the negative are in turn more visible. For $Q_\perp = \pi/2d_\perp$, a hybrid of both takes place, and the positive bands of $Q_\perp = 0$ and negative bands of $Q_\perp = \pi/d_\perp$ are seen, less intensely than the original cases, however. Nevertheless, in general, apart from pristine SLG cone, most bands are hidden. This is particularly interesting for the flat band.

As explained in the models, the tTLG dispersion may be decomposed in symmetric and antisymmetric bands, because of the z mirror symmetry, [37]. In such combination, the states are categorized into the two effective band states,

$$|\pm\rangle = \frac{1}{\sqrt{2}}\left(|1\rangle \pm |3\rangle\right), \quad |2\rangle\,, \tag{4.6.1}$$

where $|n\rangle$ is a wave function of the n-th layer. The $|+\rangle$ state shares the same parity with $|2\rangle$, having $|-\rangle$ the opposite behavior. The Hamiltonian is block diagonal, and some bands are due to the $|+\rangle$ and $|2\rangle$ coupling, while others are produced by $|-\rangle$.

In the bands due to the $|+\rangle$ and $|2\rangle$ coupling, the coefficients from layer 1 and 3 have the same value,

$$a_1^+(\mathbf{k}) = a_3^+(\mathbf{k}). \tag{4.6.2}$$

Thus, it is expected that in equation (2.34), for $Q_\perp = 0$, they interfere constructively, and for $Q_\perp = \pi/2d_\perp$ destructively. The opposite can be said for the $|-\rangle$ bands,

$$a_1^-(\mathbf{k}) = -a_3^-(\mathbf{k}). \tag{4.6.3}$$

Since the eigenvector coefficients from layer 1 and 3 have the same magnitude but different signs, at $Q_\perp = 0$ there should be destructive interference, and for $Q_\perp = \pi/2d_\perp$ the interference should be positive.

The positive interference is seen in Figures 4.6.2d and 4.6.2e. In the first, for $Q_\perp = 0$, the SLG-like cone, product of the $|-\rangle$ states, [37], does not show, having its coefficients

cancelled, and in the second, at $Q_\perp = \pi/2d_\perp$, it is well visible.

The flat band, however, is due to the $|+\rangle$ and $|2\rangle$ coupling. Therefore, it is expected to be seen for $Q_\perp = 0$ and unseen for $Q_\perp = \pi/2d_\perp$. What we observe from Figures 4.6.2d and 4.6.2e is that it is unseen in both cases.

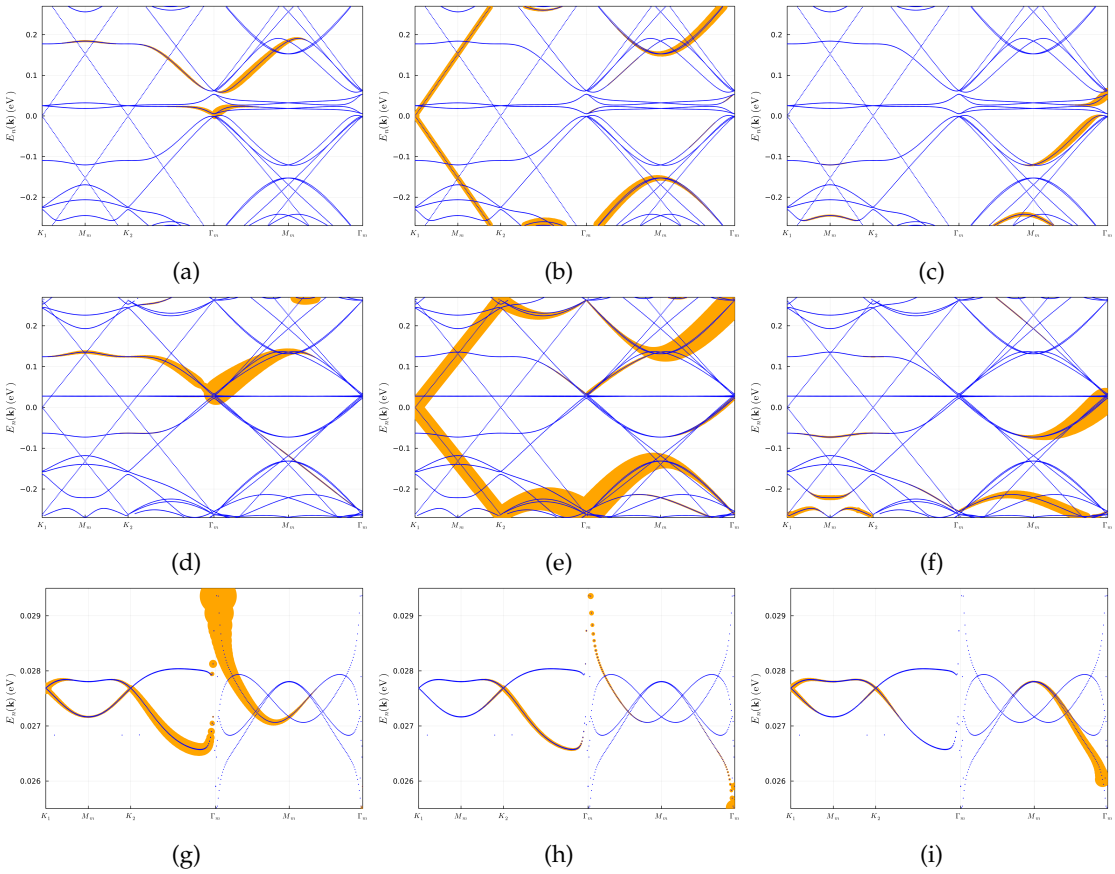

FIGURE 4.6.2: tTLG band structure (in blue) and visibility (in yellow) for $\theta \simeq 1.8°$ in (a-c) and $\theta \simeq 1.5°$ in (d-f), along the path 3.5.3c. In (g-i), we zoom in on the flat band, increasing its visibility by a factor of 10. The $Q_\perp$ is $Q_\perp = 0$ in (a), (d), (g), $Q_\perp = \pi/2d_\perp$ in (b), (e), (h), and $Q_\perp = \pi/d_\perp$ in (c), (f) and (i).

For further insight, we take the same approach as before and introduce the λ parameter in the interlayer coupling, in Figure 4.6.3. As it increases, the valence band seems to be on its way to integrate the flat band, with all its visibility, but it merges with a positive energy band, ending up intersecting with the flat band only in the first and second Γ_m, for $Q_\perp = 0$ and $Q_\perp = \pi/d_\perp$, respectively. The plot with $Q_\perp = \pi/2d_\perp$ deals with the same issue, having a less intense version of the last visible layers, and maintains an unaffected SLG Dirac cone. The Dirac cone is not influenced by the variation of the λ because, as mentioned, is decoupled from the middle layer.

It seems that the coefficients $a_\alpha^n(\mathbf{k})$ interfere destructively with one another to yield an unseen flat band, despite our predictions. Increasing the ARPES signal, one may observe in Figures 4.6.2g, 4.6.2h and 4.6.2i that it is not null and that it is roughly the same as in tBLG, having branches possibly only reached by tweaking $Q_\perp$ or by choosing a more appropriate path in the reciprocal scheme.

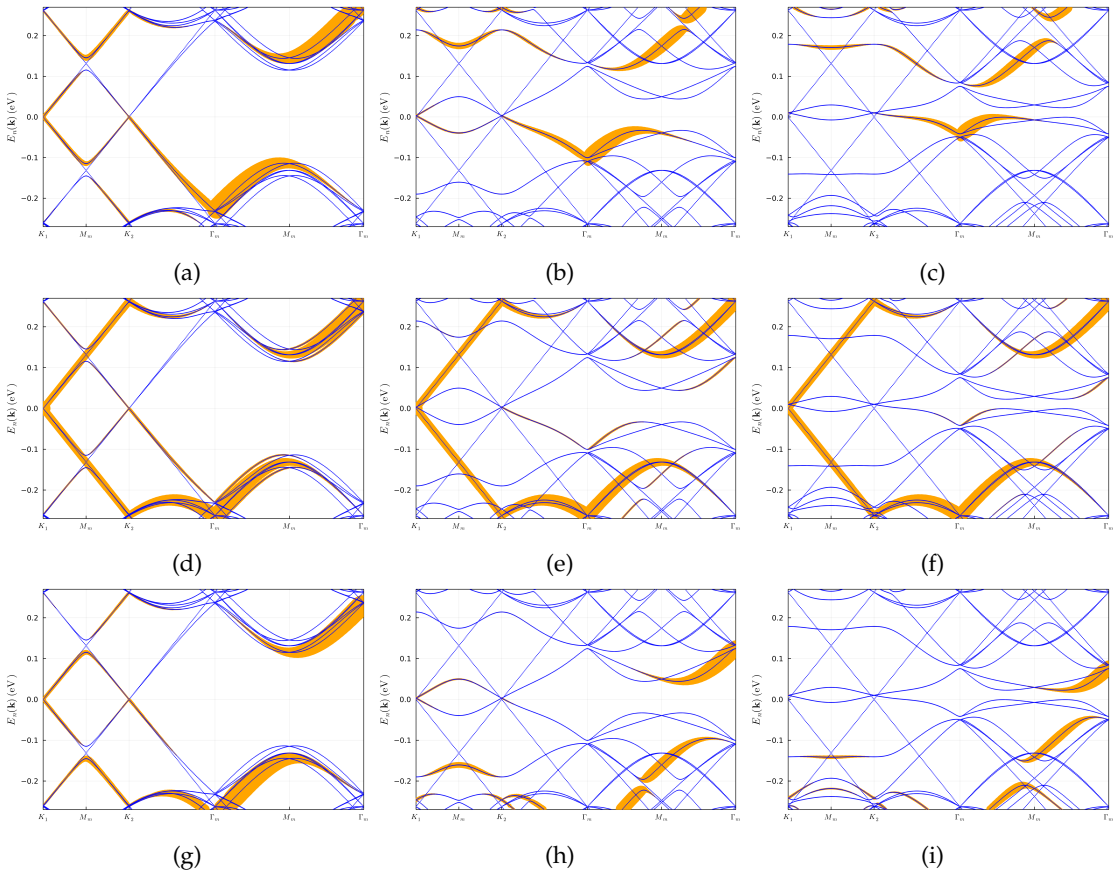

FIGURE 4.6.3: tTLG band structure (in blue) and visibility (in yellow) for $\theta \simeq 1.5°$along the path 3.5.3c, for varying interlayer coupling. For (a-c) we have $Q_\perp = 0$, $Q_\perp = \pi/2d_\perp$ in (d-f) and $Q_\perp = \pi/d_\perp$ for (g-i). The coupling parameter, λ, is $\lambda = 0.1$ in (a), (d) and (g), $\lambda = 0.5$ in (b), (e) and (h), and $\lambda = 0.7$ in (c), (f) and (i).

Applied Electric Field

In this brief section, we study the effects of an applied external electric field in the band structure and ARPES signal. For that, we apply a voltage of $V = 57,20125$ mV between the layers and study its results. These are shown in Figure 4.6.4.

Regarding the band structure, the bands are seen to hybridize with the flat band near the Fermi level. This is consistent with [37]. Furthermore, even though the bands seem

deformed when compared to the original energies, the ARPES signal is very alike to the case without field, showing practically the same results as in Figure 4.6.2.

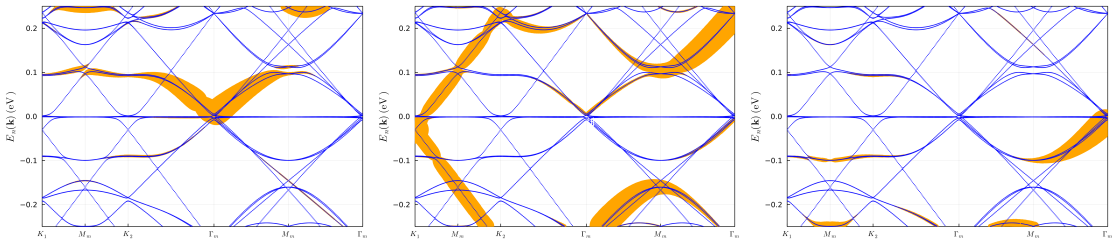

(a) (b) (c)

FIGURE 4.6.4: tTLG band structure (in blue) and visibility (in yellow) for $\theta \simeq 1.5$ °under applied electric field, along the path 3.5.3c. The $Q_\perp$ is $Q_\perp = 0$ in (a), $Q_\perp = \pi/2d_\perp$ in (b), and $Q_\perp = \pi/d_\perp$ in (c).

Chapter 5

Conclusion

In this thesis, we provided our theoretically prediction of the results of the ARPES experimental technique for simple graphene based systems, TMDs and the tBLG and tTLG, for large, intermediate and low twist angles, in the flat band regime.

In order to achieve this, we derived in chapter 2 the ARPES electronic signal expression and saw that it depended on these M matrix elements, to which we also derived an expression. From this we concluded that the ARPES signal depended on the interference between the eigenvectors coefficients and on the direction of the absorbed photon and emitted electron, as well as on the atomic form factor, that we neglect for the graphene based systems, and saw that it is independent of the system parameterization.

In chapter 3, we developed, the studied models that would be the target of our predictions, specifying its geometry, building its tight-binding Hamiltonian and discussing their band structure and DoS.

Finally, in our results chapter, we presented what we predict to be the results of an ARPES experiment, alternating between experimental parameters to fully demonstrate its properties.

The smaller systems showed a periodicity when travelling through the reciprocal space that allowed the positive bands to be seen, and in general, every system showed a cyclic behavior when varying $Q_\perp$, except the TMDs. With these, we concluded how detrimental is the atomic form factor form the ARPES signal.

We made some considerations about the visibilities for the tBLG and tTLG, namely their ARPES evolution with the decreasing of the angle, from a resemblance to a decoupled system to the disappearance of the ARPES signal in the flat bands. In order to have a better insight, the artificial scenario of slowly turning on the interlayer coupling was

executed, from which we concluded that the visibility mostly migrated to the considered Γ_m points in the path.

We also saw, particularly for the tTLG, that of the decoupled Dirac cones, the one due to the antisymmetric combination of the bottom and top layers is much more prevalent in terms of visibility because of the decoupling between the middle layer and these states.

Finally, concerning the flat bands of both tBLG and tTLG, we concluded that it is not seen in ARPES, despite our theoretical predictions.

Appendix A

Eigenvectors Invariance Under Reciprocal Lattice Translation

There are two conventions in condensed matter physics, one that writes a Bloch state as

$$\psi_{\mathbf{k},n}(\mathbf{x}) = \frac{1}{\sqrt{N}} \sum_{\mathbf{R},\alpha} e^{i\mathbf{k}\cdot(\mathbf{R}+\delta_\alpha)} a_\alpha^n(\mathbf{k}) \phi_\alpha(\mathbf{x} - (\mathbf{R}_n + \delta_\alpha)) \tag{A.0.1}$$

and other that writes it as

$$\psi_{\mathbf{k},n}(\mathbf{x}) = \frac{1}{\sqrt{N}} \sum_{\mathbf{R},\alpha} e^{i\mathbf{k}\cdot\mathbf{R}} a_\alpha^n(\mathbf{k}) \phi_\alpha(\mathbf{x} - (\mathbf{R}_n + \delta_\alpha)). \tag{A.0.2}$$

This amounts to writing the state coefficient as $e^{i\mathbf{k}\cdot\delta} a_\alpha^n(\mathbf{k})$ or as $a_\alpha^n(\mathbf{k})$. Both agree that

$$\psi_{\mathbf{k}+\mathbf{G},n} = \psi_{\mathbf{k}n}. \tag{A.0.3}$$

So, since $e^{i\mathbf{G}\cdot\mathbf{R}} = 1$, for the first we have

$$\begin{aligned} \psi_{\mathbf{k},n}(\mathbf{x}) &= \frac{1}{\sqrt{N}} \sum_{\mathbf{R}_n,\alpha} e^{i\mathbf{k}\cdot(\mathbf{R}_n+\delta_\alpha)} a_\alpha^n(\mathbf{k}) \phi_\alpha(\mathbf{x} - (\mathbf{R}_n + \delta_\alpha)) \\ &= \psi_{\mathbf{k}+\mathbf{G},n}(\mathbf{x}) = \frac{1}{\sqrt{N}} \sum_{\mathbf{R}_n,\alpha} e^{i\mathbf{k}\cdot(\mathbf{R}_n+\delta_\alpha)} e^{i\mathbf{G}\cdot\delta_\alpha} a_\alpha^n(\mathbf{k}+\mathbf{G}) \phi_\alpha(\mathbf{x} - (\mathbf{R}_n + \delta_\alpha)) \end{aligned} \tag{A.0.4}$$

and hence,

$$a_\alpha^n(\mathbf{k}) = e^{i\mathbf{G}\cdot\delta_\alpha} a_\alpha^n(\mathbf{k}+\mathbf{G}), \tag{A.0.5}$$

and for the other

$$a_\alpha^n(\mathbf{k}) = a_\alpha^n(\mathbf{k}+\mathbf{G}). \tag{A.0.6}$$

Appendix B

Commensurability Condition

As mentioned in section 3.1, graphene has Bravais vectors given by

$$\begin{aligned} \mathbf{a}_1 &= \frac{a}{2}\left(1, \sqrt{3}\right) \\ \mathbf{a}_2 &= \frac{a}{2}\left(-1, \sqrt{3}\right), \end{aligned} \tag{B.0.1}$$

and its lattice is invariant under $2\pi/3$ rotations and reflections in the planes connecting nearest-neighbors, taking a site A as the origin. Ignoring sites B, this symmetry increases to an angle $\pi/3$. If we stack a layer on top of this, so that the B orbitals are atop the A sites, forming a A_1B_2 pair (1 stands for the bottom layer and 2 for the top), neglecting A_2 sites, we keep a system invariant under rotations of $\pi/3$. Not only that but a generic point is at position

$$\mathbf{P}_1 = n\mathbf{a}_1 + m\mathbf{a}_2, \tag{B.0.2}$$

and at distance

$$a\sqrt{m^2 + n^2 + mn} = a\rho_a \tag{B.0.3}$$

for m, n integers and ρ_a a non-negative integer. Since, due to this rotational symmetry, if we rotate our lattice by $\pi/3$, we get an equivalent system, we can say that there are at least six atoms, for each layer, that satisfy the condition in equation B.0.3. Actually, we can check that there are always at least six (m, n) pairs that solve it.

Furthermore, as mentioned, this lattice also manifests mirror symmetry on the lines traced in Figure B.0.1b, meaning that a point at $\mathbf{P}_1$ involves the existence of six other $\{\mathbf{Q}\}$ points. An example of one such point is

$$\mathbf{Q}_1 = m\mathbf{a}_1 + n\mathbf{a}_2. \tag{B.0.4}$$

Another is

$$\mathbf{Q}_6 = (m+n)\mathbf{a}_1 - m\mathbf{a}_2. \tag{B.0.5}$$

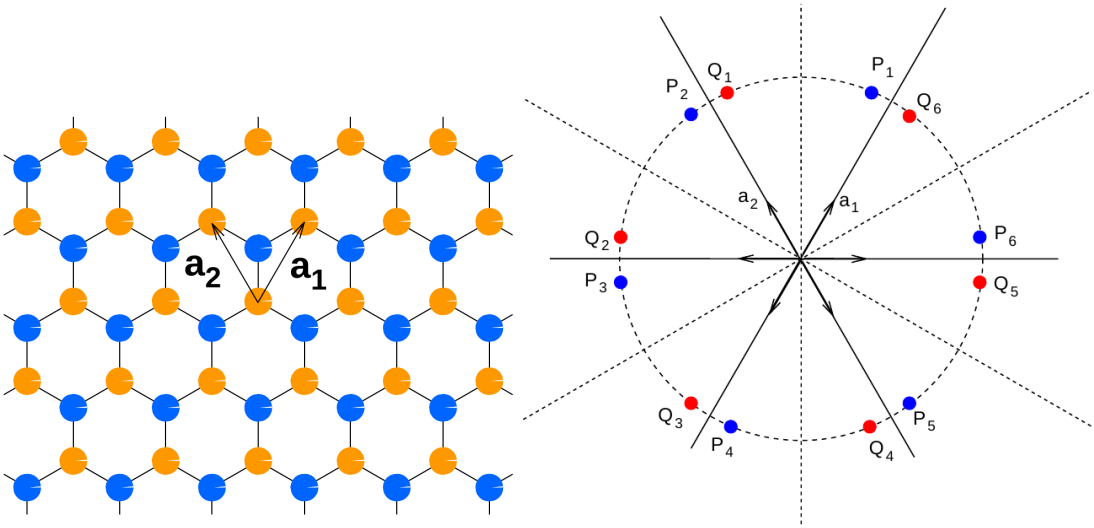

(a) (b)

FIGURE B.0.1: Geometry of the honeycomb lattice in (A) and shell of twelve identical lattice sites in (B). Figures taken from [61].

What we're saying is, that at any of these points, we have a A_1B_2 pair, so, if we bring the B_1 orbital at $\mathbf{P}_1$ to $\mathbf{Q}_1$, we get a system with a much larger periodicity, but a periodic structure nonetheless. The same applies if we bring this site to point $\mathbf{Q}_6$. We see, that by rotating one of the layers by these angles, we arrive at another commensurate structure. Computing the dot product between these points, we reach two conditions for them,

$$\mathbf{P}_1 \cdot \mathbf{Q}_1 \Rightarrow \cos(\theta) = \frac{3m^2 + 3mr + r^2/2}{3m^2 + 3mr + r^2} \tag{B.0.6a}$$

$$= \frac{3(m + r/2)^2 - (r/2)^2}{3(m + r/2)^2 + (r/2)^2} \tag{B.0.6b}$$

and

$$\mathbf{P}_1 \cdot \mathbf{Q}_6 \Rightarrow \cos(\theta) = \frac{3p^2/2 + 3ps + s^2}{3p^2 + 3ps + s^2} \tag{B.0.7a}$$

$$= \frac{3(3p/2 + s)^2 - (3p/2)^2}{3(3p/2 + s)^2 + (3p/2)^2}, \tag{B.0.7b}$$

where we've made $r = n - m$ in the first and $(m, n) \to (q, p) = (s + p, p)$ in the second. From equations B.0.6b and B.0.7b we promptly see that the families define the same set of angles if $m/r = s/3p$, so equation B.0.6a includes the rotations in equation B.0.7a.

Considering the first, at a distance given by B.0.3, or $a\sqrt{3m^2 + 3mr + r^2}$, in terms of the positive integers m and r, its position $\mathbf{Q}_1$ defines a super-lattice Bravais vector if there are no other smaller vectors for the same angle. Let's say that the pair (p, q) generates such a vector. Then, they have the same rotation,

$$\frac{3m^2 + 3mr + r^2/2}{3m^2 + 3mr + r^2} = \frac{3p^2 + 3pq + q^2/2}{3p^2 + 3pq + q^2} \tag{B.0.8}$$

and a smaller size, which yields

$$3m^2 + 3mr + r^2/2 = s^2(3p^2 + 3pq + q^2/2) \tag{B.0.9a}$$

$$3m^2 + 3mr + r^2 = s^2(3p^2 + 3pq + q^2) \tag{B.0.9b}$$

for a positive integer s^2. Subtracting these equations, one gets $r/s = q$ and, solving equation B.0.9b for m/s, yields the result $m/s = p$, meaning that s divides both m and r. Therefore, if they are co-prime to begin with, $s = 1$ and the smaller vector for this angle is $\mathbf{Q}_1$. One can obtain the same results for the angle in equation B.0.7a, where the smaller vector is seen to be $\mathbf{Q}_6$.

Summing our results, a commensurate angle is determined by

$$\cos(\theta) = \frac{3m^2 + 3mr + r^2/2}{3m^2 + 3mr + r^2} \tag{B.0.10}$$

and its Bravais vectors are

$$\begin{pmatrix} \mathbf{t}_1 \\ \mathbf{t}_2 \end{pmatrix} = \begin{pmatrix} m & m + r \\ -(m + r) & 2m + r \end{pmatrix} \begin{pmatrix} \mathbf{a}_1 \\ \mathbf{a}_2 \end{pmatrix} \tag{B.0.11}$$

if $\gcd(r, 3) = 1$ and

$$\begin{pmatrix} \mathbf{t}_1 \\ \mathbf{t}_2 \end{pmatrix} = \begin{pmatrix} m + r/3 & r/3 \\ -r/3 & m + 2r/3 \end{pmatrix} \begin{pmatrix} \mathbf{a}_1 \\ \mathbf{a}_2 \end{pmatrix} \tag{B.0.12}$$

for $\gcd(r, 3) = 3$, where we obtained the $\mathbf{t}_2$ vector by rotating $\mathbf{t}_1$ $\pi/3$.

We can also write them in terms of the rotated layer primitive vectors, $\mathbf{a}'_1$ and $\mathbf{a}'_2$, noticing that

$$\begin{pmatrix} \mathbf{a}_1 \\ \mathbf{a}_2 \end{pmatrix} = \begin{pmatrix} \cos(\theta) + \sin(\theta)/\sqrt{3} & -2\sin(\theta)/\sqrt{3} \\ 2\sin(\theta)/\sqrt{3} & \cos(\theta) - \sin(\theta)/\sqrt{3} \end{pmatrix} \begin{pmatrix} \mathbf{a}'_1 \\ \mathbf{a}'_2 \end{pmatrix}, \tag{B.0.13}$$

for $\gcd(r, 3) = 1$ we have

$$\begin{pmatrix} \mathbf{t}_1 \\ \mathbf{t}_2 \end{pmatrix} = \begin{pmatrix} m + r & m \\ -m & 2m + r \end{pmatrix} \begin{pmatrix} \mathbf{a}'_1 \\ \mathbf{a}'_2 \end{pmatrix} \tag{B.0.14}$$

and, for $\gcd(r, 3) = 3$,

$$\begin{pmatrix} \mathbf{t}_1 \\ \mathbf{t}_2 \end{pmatrix} = \begin{pmatrix} m + 2r/3 & -r/3 \\ r/3 & m + r/3 \end{pmatrix} \begin{pmatrix} \mathbf{a}'_1 \\ \mathbf{a}'_2 \end{pmatrix}. \tag{B.0.15}$$

Appendix C

Relevant Codes

In this appendix, we show some functions we find relevant example codes. Firstly, we show the Hamiltonian function for the SLG supercell. This function takes as input a reciprocal vector `q`, the considered hoppings, `h`, and its orbitals' positions, `v`, and the number of graphene unit cells, `A1` and `A2`. It then pivots around each orbital to establish the Hamiltonian matrix elements.

```
function Ham(q,t,v,A1,A2)

    orbs = length(t[:,1,1])

    torbs = A1*A2*orbs

    lt = length(t[1,1,:])

    dim = torbs

    h = zeros(Complex{Float64},dim,dim)

    for m in 1:A1

        ma1 = (m-1)*a1

        for n in 1:A2

            na2 = (n-1)*a2

            cell = (n-1)*A1 + m

            for alphap in 1:orbs

                alpha = (cell-1)*orbs + alphap
```

```
for k in 1:(2*lt+1)

    s = k - (lt+1)

    sa1 = s*a1

    for l in 1:(2*lt+1)

        p = l - (lt+1)

        pa2 = p*a2

        cell2 = cell + p*A1 + s

        for betap in 1:orbs

            beta = (cell2-1)*orbs + betap

            vec = sa1 + pa2 + delta[betap,:] - delta[alphap,:]

            r = round(sqrt(dot(vec,vec)),digits=4)

            for (i,d) in enumerate(v)

                dd = round(d, digits=4)

                if dd == r

                    if m + s > A1

                        betao = beta - A1*orbs

                        if n + p > A2

                            betao = betao - A1*A2*orbs

                            h[alpha,betao] = h[alpha,betao] +
                            t[alphap,betap,i]*exp(im*dot(q,vec))

                        elseif n + p < 1

                            betao = A1*A2*orbs + betao

                            h[alpha,betao] = h[alpha,betao] +
                            t[alphap,betap,i]*exp(im*dot(q,vec))
```

```
        else

            h[alpha,betao] = h[alpha,betao] +
            t[alphap,betap,i]*exp(im*dot(q,vec))

        end

    elseif m + s < 1

        betao = beta + A1*orbs

        if n + p > A2

            betao = betao - A1*A2*orbs

            h[alpha,betao] = h[alpha,betao] +
            t[alphap,betap,i]*exp(im*dot(q,vec))

        elseif n + p < 1

            betao = A1*A2*orbs + betao

            h[alpha,betao] = h[alpha,betao] +
            t[alphap,betap,i]*exp(im*dot(q,vec))

        else

            h[alpha,betao] = h[alpha,betao] +
            t[alphap,betap,i]*exp(im*dot(q,vec))

        end

    elseif n + p > A2

        betao = beta - A1*A2*orbs

        h[alpha,betao] = h[alpha,betao] +
        t[alphap,betap,i]*exp(im*dot(q,vec))

    elseif n + p < 1

        betao = A1*A2*orbs + beta

        h[alpha,betao] = h[alpha,betao] +
        t[alphap,betap,i]*exp(im*dot(q,vec))

    else
```

```
                                        h[alpha,beta] = h[alpha,beta] +
                                        t[alphap,betap,i]*exp(im*dot(q,vec))

                                    end

                                end

                            end

                        end

                    end

                end

            end

        end

    end

    return h

end
```

We also show the code we use to create a path in reciprocal space. As its arguments, we write the set of vectors in reciprocal space we want our bands to go through (for instance, in Figure 3.1.2a we would input $\Gamma - M - K - \Gamma$), and a parameter `N` controlling the number of $\mathbf{k}$ points taken into account. Then it generates the reciprocal vectors between the edges specified in the `kpts`.

```
function piecewisepath(kpts...; N)

    nverts = length(kpts)

    edges = nverts - 1

    Ns = []

    NN = 0

    for i in 1:edges

        Nsi = trunc(Int, norm(kpts[i+1]-kpts[i])/norm(kpts[2]-kpts[1]) * N)
```

```
        push!(Ns, Nsi)
        NN += Nsi
    end
    m = edges
    patharc = zeros(2)
    s = zeros(NN)
    kpath = zeros(3,NN)
    spts = zeros(nverts)
    NNi = 0
    for i in 1:edges
        for j in 1:2
            kpath[j,NNi + 1:NNi + Ns[i]] = collect(range(kpts[i][j],kpts[i+1][j],length = Ns[i]))
        end
        patharc[2] = patharc[1] + sqrt(dot(kpts[i+1]-kpts[i],kpts[i+1]-kpts[i]))
        s[NNi + 1:NNi + Ns[i]] = collect(range(patharc[1],patharc[2],length = Ns[i]))
        patharc[1] = patharc[2]
        spts[i+1] = s[NNi + Ns[i]]
        NNi = sum(Ns[1:i])
    end
    return kpath, s, nverts, spts
end
```

Finally, we show the function we use to diagonalize the sparse Hamiltonian with the Arnoldi method. In line 21 we use the macro `@threads` to parallelize the process, and compute separately the eigenvectors and eigenvalues for each $\mathbf{k}$. In line 33 we perform the sum to be squared in line 37 to obtain the band visibility in that point.

```
function bandas(kpath, nvals, H, Qz)

    phi2s = zeros(2)

    nks = length(kpath[1,:])

    Ham(phi2s) = bloch(H, phi2s)

    tt1 = bravais(H)[:,1]

    tt2 = bravais(H)[:,2]

    Bandas = zeros(nvals,nks)

    Mspath = zeros(nvals,nks)

    num_bandas = length(Ham(phi2s)[1,:])

    sites = [site for site in sitepositions(H)]

    @threads for k in 1:nks

        lambda, phi = eigsolve(Ham([dot(kpath[:,k], tt1), dot(kpath[:,k], tt2)]), nvals,
        EigSorter(abs; rev = false), tol = 10^(-4), krylovdim = 2*nvals, maxiter = 2000)

        for bb in 1:nvals

            Bandas[bb,k] = real(lambda[bb])

            soma = 0

            for (b, sp) in enumerate(sites)

                soma += phi[bb][b] * exp(-im * dot(kpath[:,k] + [0,0,Qz],sp))

            end

            Mspath[bb,k] = abs2(soma)

        end

    end

    return num_bandas, Bandas, Mspath

end
```

Appendix D

Tables

In this appendix, we show Table D.0.1, used to build the Kaxiras tight-binding Hamiltonian in section 3.4.

Slater-Koster Parameters in eV	
Parameter	Reference [41]
ε_1	1.0688
ε_2	1.0688
ε_3	- 0.7755
ε_4	- 1.2902
ε_5	- 1.2902
ε_6	- 0.138
ε_7	0.0874
ε_8	0.0874
ε_9	- 2.8949
ε_{10}	- 1.9065
ε_{11}	- 1.9065
$t^1_{1,1}$	- 0.2069
$t^1_{2,2}$	0.0323
$t^1_{3,3}$	- 0.1739
$t^1_{4,4}$	0.8651
$t^1_{5,5}$	- 0.1872
$t^1_{6,6}$	- 0.2979
$t^1_{7,7}$	0.2747
$t^1_{8,8}$	- 0.5581
$t^1_{9,9}$	- 0.1916
$t^1_{10,10}$	0.9122
$t^1_{11,11}$	0.0059
$t^1_{3,5}$	- 0.0679
$t^1_{6,8}$	0.4096
$t^1_{9,11}$	0.0075
$t^1_{1,2}$	- 0.2562
$t^1_{3,4}$	- 0.0995
$t^1_{4,5}$	- 0.0705
$t^1_{6,7}$	- 0.1145
$t^1_{7,8}$	- 0.2487
$t^1_{9,10}$	0.1063
$t^1_{10,11}$	- 0.0385
$t^5_{4,1}$	- 0.7883
$t^5_{3,2}$	- 1.3790
$t^5_{5,2}$	2.1584
$t^5_{9,6}$	- 0.8836
$t^5_{11,6}$	- 0.9402
$t^5_{10,7}$	1.4114
$t^5_{9,8}$	- 0.9535
$t^5_{11,8}$	0.6517
$t^6_{11,6}$	- 0.0686
$t^6_{9,8}$	- 0.1498
$t^6_{11,8}$	- 0.2205
$t^6_{9,6}$	- 0.2451

TABLE D.0.1: SKp for the Hamiltonian hoppings according to [41].

Bibliography

[1] B. Amorim, "General theoretical description of angle-resolved photoemission spectroscopy of van der waals structures," *Physical Review B*, vol. 97, no. 16, Apr 2018. [Online]. Available: http://dx.doi.org/10.1103/PhysRevB.97.165414 [Cited on pages v, vii, xi, xii, 2, 3, 17, 20, 21, 22, 24, 25, 27, 30, and 31.]

[2] A. K. Geim, "Graphene prehistory," *Physica Scripta*, vol. T146, p. 014003, jan 2012. [Online]. Available: https://doi.org/10.1088/0031-8949/2012/t146/014003 [Cited on page 1.]

[3] A. K. Geim and K. S. Novoselov, "The rise of graphene." *Nature materials*, vol. 6 3, pp. 183–91, 2007. [Cited on page 1.]

[4] R. Peierls, "Quelques propriétés typiques des corps solides," *Annales de l'institut Henri Poincaré*, vol. 5, no. 3, pp. 177–222, 1935. [Online]. Available: http://eudml.org/doc/78996

[5] L. D. Landau, "Zur theorie der phasenumwandlungen ii," *Phys. Z. Sowjetunion*, vol. 11, no. 545, pp. 26–35, 1937. [Cited on page 1.]

[6] K. S. Novoselov, D. Jiang, F. Schedin, T. J. Booth, V. V. Khotkevich, S. V. Morozov, and A. K. Geim, "Two-dimensional atomic crystals," *Proceedings of the National Academy of Sciences*, vol. 102, no. 30, p. 10451–10453, Jul 2005. [Online]. Available: http://dx.doi.org/10.1073/pnas.0502848102 [Cited on page 1.]

[7] K. S. Novoselov, A. Mishchenko, A. Carvalho, and A. H. Castro Neto, "2d materials and van der waals heterostructures," *Science*, vol. 353, no. 6298, p. aac9439, Jul 2016. [Online]. Available: http://dx.doi.org/10.1126/science.aac9439 [Cited on page 1.]

[8] K. S. Kim, Y. Zhao, H. Jang, S. Y. Lee, J. M. Kim, K. S. Kim, J.-H. Ahn, P. Kim, J. Choi, and B. H. Hong, "Large-scale pattern growth of graphene films for stretchable transparent electrodes," *Nature*, vol. 457, pp. 706–710, 2009. [Cited on page 1.]

[9] K. Novoselov and A. Castro Neto, "Two-dimensional crystals-based heterostructures: Materials with tailored properties," *Physica Scripta*, vol. 2012, p. 014006, 01 2012. [Cited on pages 1 and 2.]

[10] A. K. Geim and I. V. Grigorieva, "Van der waals heterostructures," *Nature*, vol. 499, no. 7459, p. 419–425, Jul 2013. [Online]. Available: http://dx.doi.org/10.1038/nature12385 [Cited on page 1.]

[11] L. Britnell, R. V. Gorbachev, R. Jalil, B. D. Belle, F. Schedin, A. Mishchenko, T. Georgiou, M. I. Katsnelson, L. Eaves, S. V. Morozov, and et al., "Field-effect tunneling transistor based on vertical graphene heterostructures," *Science*, vol. 335, no. 6071, p. 947–950, Feb 2012. [Online]. Available: http://dx.doi.org/10.1126/science.1218461 [Cited on page 2.]

[12] T. Georgiou, R. Jalil, B. D. Belle, L. Britnell, R. V. Gorbachev, S. V. Morozov, Y.-J. Kim, A. Gholinia, S. J. Haigh, O. Makarovsky, and et al., "Vertical field-effect transistor based on graphene–ws2 heterostructures for flexible and transparent electronics," *Nature Nanotechnology*, vol. 8, no. 2, p. 100–103, Dec 2012. [Online]. Available: http://dx.doi.org/10.1038/nnano.2012.224 [Cited on page 2.]

[13] L. Britnell, R. Ribeiro, A. Eckmann, R. Jalil, B. Belle, A. Mishchenko, Y.-J. Kim, R. Gorbachev, T. Georgiou, S. Morozov, A. Grigorenko, A. Geim, C. Casiraghi, A. Castro Neto, and K. Novoselov, "Strong light-matter interactions in heterostructures of atomically thin films," *Science (New York, N.Y.)*, vol. 340, 05 2013. [Cited on page 2.]

[14] M. Massicotte, P. Schmidt, F. Vialla, K. G. Schädler, A. Reserbat-Plantey, K. Watanabe, T. Taniguchi, K. J. Tielrooij, and F. H. L. Koppens, "Picosecond photoresponse in van der waals heterostructures," *Nature Nanotechnology*, vol. 11, no. 1, p. 42–46, Oct 2015. [Online]. Available: http://dx.doi.org/10.1038/nnano.2015.227 [Cited on page 2.]

[15] A. Damascelli, Z. Hussain, and Z.-X. Shen, "Angle-resolved photoemission studies of the cuprate superconductors," *Reviews of Modern Physics*, vol. 75, no. 2, p. 473–541, Apr 2003. [Online]. Available: http://dx.doi.org/10.1103/RevModPhys.75.473 [Cited on page 2.]

[16] A. A. Kordyuk, "Arpes experiment in fermiology of quasi-2d metals (review article)," *Low Temperature Physics*, vol. 40, no. 4, p. 286–296, Apr 2014. [Online]. Available: http://dx.doi.org/10.1063/1.4871745

[17] E. L. Shirley, L. J. Terminello, A. Santoni, and F. J. Himpsel, "Brillouin-zone-selection effects in graphite photoelectron angular distributions," *Phys. Rev. B*, vol. 51, pp. 13 614–13 622, May 1995. [Online]. Available: https://link.aps.org/doi/10.1103/PhysRevB.51.13614

[18] S. Moser, "An experimentalist's guide to the matrix element in angle resolved photoemission," *Journal of Electron Spectroscopy and Related Phenomena*, vol. 214, pp. 29–52, 2017. [Cited on page 2.]

[19] M. Mucha-Kruczyński, J. R. Wallbank, and V. I. Fal'ko, "Moiré miniband features in the angle-resolved photoemission spectra of graphene/*h*BN heterostructures," *Phys. Rev. B*, vol. 93, p. 085409, Feb 2016. [Online]. Available: https://link.aps.org/doi/10.1103/PhysRevB.93.085409 [Cited on page 2.]

[20] A. Pal and E. J. Mele, "Nodal surfaces in photoemission from twisted bilayer graphene," *Phys. Rev. B*, vol. 87, p. 205444, May 2013. [Online]. Available: https://link.aps.org/doi/10.1103/PhysRevB.87.205444

[21] M. Mucha-Kruczyński, O. Tsyplyatyev, A. Grishin, E. McCann, V. I. Fal'ko, A. Bostwick, and E. Rotenberg, "Characterization of graphene through anisotropy of constant-energy maps in angle-resolved photoemission," *Physical Review B*, vol. 77, no. 19, May 2008. [Online]. Available: http://dx.doi.org/10.1103/PhysRevB.77.195403 [Cited on page 2.]

[22] J. M. B. Lopes dos Santos, N. M. R. Peres, and A. H. Castro Neto, "Graphene bilayer with a twist: Electronic structure," *Physical Review Letters*, vol. 99, no. 25, Dec 2007. [Online]. Available: http://dx.doi.org/10.1103/PhysRevLett.99.256802 [Cited on pages 2 and 45.]

[23] G. Trambly de Laissardière, D. Mayou, and L. Magaud, "Localization of dirac electrons in rotated graphene bilayers," *Nano Letters*, vol. 10, no. 3, pp. 804–808, Mar 2010. [Online]. Available: https://doi.org/10.1021/nl902948m

[24] A. Luican, G. Li, A. Reina, J. Kong, R. R. Nair, K. S. Novoselov, A. K. Geim, and E. Y. Andrei, "Single-layer behavior and its breakdown in twisted graphene layers," *Phys. Rev. Lett.*, vol. 106, p. 126802, Mar 2011. [Online]. Available: https://link.aps.org/doi/10.1103/PhysRevLett.106.126802 [Cited on pages 2 and 45.]

[25] G. Li, A. Luican, J. M. B. Lopes dos Santos, A. H. Castro Neto, A. Reina, J. Kong, and E. Y. Andrei, "Observation of van hove singularities in twisted graphene layers," *Nature Physics*, vol. 6, no. 2, pp. 109–113, Feb 2010. [Online]. Available: https://doi.org/10.1038/nphys1463 [Cited on page 2.]

[26] H. Z. Olyaei, B. Amorim, P. Ribeiro, and E. V. Castro, "Ballistic charge transport in twisted bilayer graphene," 2020. [Cited on page 2.]

[27] G. Tarnopolsky, A. J. Kruchkov, and A. Vishwanath, "Origin of magic angles in twisted bilayer graphene," *Physical Review Letters*, vol. 122, no. 10, Mar 2019. [Online]. Available: http://dx.doi.org/10.1103/PhysRevLett.122.106405 [Cited on pages 2, 45, and 49.]

[28] R. Bistritzer and A. H. MacDonald, "Moire bands in twisted double-layer graphene," *Proceedings of the National Academy of Sciences*, vol. 108, no. 30, p. 12233–12237, Jul 2011. [Online]. Available: http://dx.doi.org/10.1073/pnas.1108174108 [Cited on pages 2 and 45.]

[29] Y. Cao, V. Fatemi, A. Demir, S. Fang, S. L. Tomarken, J. Y. Luo, J. D. Sanchez-Yamagishi, K. Watanabe, T. Taniguchi, E. Kaxiras, R. C. Ashoori, and P. Jarillo-Herrero, "Correlated insulator behaviour at half-filling in magic-angle graphene superlattices," *Nature*, vol. 556, no. 7699, pp. 80–84, Apr 2018. [Online]. Available: https://doi.org/10.1038/nature26154 [Cited on page 2.]

[30] A. L. Sharpe, E. J. Fox, A. W. Barnard, J. Finney, K. Watanabe, T. Taniguchi, M. A. Kastner, and D. Goldhaber-Gordon, "Emergent ferromagnetism near three-quarters filling in twisted bilayer graphene," *Science*, vol. 365, no. 6453, p. 605–608, Jul 2019. [Online]. Available: http://dx.doi.org/10.1126/science.aaw3780

[31] M. Serlin, C. L. Tschirhart, H. Polshyn, Y. Zhang, J. Zhu, K. Watanabe, T. Taniguchi, L. Balents, and A. F. Young, "Intrinsic quantized anomalous hall effect in a moiré

heterostructure," *Science*, vol. 367, no. 6480, p. 900–903, Dec 2019. [Online]. Available: http://dx.doi.org/10.1126/science.aay5533 [Cited on page 2.]

[32] M. Yankowitz, S. Chen, H. Polshyn, Y. Zhang, K. Watanabe, T. Taniguchi, D. Graf, A. F. Young, and C. R. Dean, "Tuning superconductivity in twisted bilayer graphene," *Science*, vol. 363, no. 6431, p. 1059–1064, Jan 2019. [Online]. Available: http://dx.doi.org/10.1126/science.aav1910 [Cited on page 2.]

[33] X. Lu, P. Stepanov, W. Yang, M. Xie, M. A. Aamir, I. Das, C. Urgell, K. Watanabe, T. Taniguchi, G. Zhang, A. Bachtold, A. H. MacDonald, and D. K. Efetov, "Superconductors, orbital magnets and correlated states in magic-angle bilayer graphene," *Nature*, vol. 574, no. 7780, pp. 653–657, Oct 2019. [Online]. Available: https://doi.org/10.1038/s41586-019-1695-0

[34] Y. Cao, V. Fatemi, S. Fang, K. Watanabe, T. Taniguchi, E. Kaxiras, and P. Jarillo-Herrero, "Unconventional superconductivity in magic-angle graphene superlattices," *Nature*, vol. 556, no. 7699, pp. 43–50, Apr 2018. [Online]. Available: https://doi.org/10.1038/nature26160 [Cited on page 2.]

[35] A. Fischer, Z. A. H. Goodwin, A. A. Mostofi, J. Lischner, D. M. Kennes, and L. Klebl, "Unconventional superconductivity in magic-angle twisted trilayer graphene," 2021. [Cited on page 3.]

[36] E. Khalaf, A. J. Kruchkov, G. Tarnopolsky, and A. Vishwanath, "Magic angle hierarchy in twisted graphene multilayers," *Physical Review B*, vol. 100, no. 8, Aug 2019. [Online]. Available: http://dx.doi.org/10.1103/PhysRevB.100.085109 [Cited on page 52.]

[37] S. Carr, C. Li, Z. Zhu, E. Kaxiras, S. Sachdev, and A. Kruchkov, "Ultraheavy and ultra-relativistic dirac quasiparticles in sandwiched graphenes," *Nano Letters*, vol. XXXX, 03 2020. [Cited on pages 3, 50, 51, 52, 72, 73, 74, and 76.]

[38] J. Zhu, J. Shi, and A. H. MacDonald, "Theory of angle-resolved photoemission spectroscopy in graphene-based moiré superlattices," *Physical Review B*, vol. 103, no. 23, Jun 2021. [Online]. Available: http://dx.doi.org/10.1103/PhysRevB.103.235146 [Cited on page 3.]

[39] J. A. Sobota, Y. He, and Z.-X. Shen, "Angle-resolved photoemission studies of quantum materials," *Reviews of Modern Physics*, vol. 93, no. 2, May 2021. [Online]. Available: http://dx.doi.org/10.1103/RevModPhys.93.025006 [Cited on pages xi and 6.]

[40] E. Cappelluti, R. Roldán, J. A. Silva-Guillén, P. Ordejón, and F. Guinea, "Tight-binding model and direct-gap/indirect-gap transition in single-layer and multilayer mos2," *Physical Review B*, vol. 88, no. 7, Aug 2013. [Online]. Available: http://dx.doi.org/10.1103/PhysRevB.88.075409 [Cited on pages xii, 17, 35, 42, 57, 66, and 67.]

[41] S. Fang, R. Kuate Defo, S. N. Shirodkar, S. Lieu, G. A. Tritsaris, and E. Kaxiras, "Ab initio tight-binding hamiltonian for transition metal dichalcogenides," *Phys. Rev. B*, vol. 92, p. 205108, Nov 2015. [Online]. Available: https://link.aps.org/doi/10.1103/PhysRevB.92.205108 [Cited on pages xii, 17, 31, 41, 45, 57, 66, and 94.]

[42] J. Silva-Guillén, P. San-Jose, and R. Roldán, "Electronic band structure of transition metal dichalcogenides from ab initio and slater–koster tight-binding model," *Applied Sciences*, vol. 6, no. 10, p. 284, Oct 2016. [Online]. Available: http://dx.doi.org/10.3390/app6100284 [Cited on pages xii, 17, 35, 42, 57, 66, and 67.]

[43] S. K. Tiwari, S. Sahoo, N. Wang, and A. Huczko, "Graphene research and their outputs: Status and prospect," *Journal of Science: Advanced Materials and Devices*, vol. 5, no. 1, pp. 10–29, Mar. 2020. [Online]. Available: https://doi.org/10.1016/j.jsamd.2020.01.006 [Cited on pages 17 and 19.]

[44] G. Catarina, B. Amorim, E. V. Castro, E. V. Castro, E. V. Castro, J. M. V. P. Lopes, J. M. V. P. Lopes, and N. Peres, "Twisted bilayer graphene: Low-energy physics, electronic and optical properties," *Handbook of Graphene*, p. 177–231, Jun 2019. [Online]. Available: http://dx.doi.org/10.1002/9781119468455.ch44 [Cited on pages xi, xii, 17, 18, 19, 21, 22, 23, 25, 26, 27, 30, 31, and 49.]

[45] M. Gonçalves, H. Z. Olyaei, B. Amorim, R. Mondaini, P. Ribeiro, and E. V. Castro, "Incommensurability-induced sub-ballistic narrow-band-states in twisted bilayer graphene," *2D Materials*, vol. 9, no. 1, p. 011001, Nov 2021. [Online]. Available: http://dx.doi.org/10.1088/2053-1583/ac3259 [Cited on pages xi, xii, 17, 20, 21, 22, 24, 25, 27, 30, and 31.]

[46] D. Tong, "Solid state physics," 2017. [Cited on pages 19 and 22.]

[47] N. W. Ashcroft and N. D. Mermin, *Solid State Physics*. Holt-Saunders, 1976. [Cited on pages 20 and 22.]

[48] A. H. Castro Neto, F. Guinea, N. M. R. Peres, K. S. Novoselov, and A. K. Geim, "The electronic properties of graphene," *Reviews of Modern Physics*, vol. 81, no. 1, p. 109–162, Jan 2009. [Online]. Available: http://dx.doi.org/10.1103/RevModPhys.81.109 [Cited on page 22.]

[49] G. Trambly de Laissardière, D. Mayou, and L. Magaud, "Numerical studies of confined states in rotated bilayers of graphene," *Physical Review B*, vol. 86, no. 12, Sep 2012. [Online]. Available: http://dx.doi.org/10.1103/PhysRevB.86.125413 [Cited on page 26.]

[50] A. Kretinin, G. L. Yu, R. Jalil, Y. Cao, F. Withers, A. Mishchenko, M. I. Katsnelson, K. S. Novoselov, A. K. Geim, and F. Guinea, "Quantum capacitance measurements of electron-hole asymmetry and next-nearest-neighbor hopping in graphene," *Phys. Rev. B*, vol. 88, p. 165427, Oct 2013. [Online]. Available: https://link.aps.org/doi/10.1103/PhysRevB.88.165427 [Cited on page 26.]

[51] J. T. Ye, Y. J. Zhang, R. Akashi, M. S. Bahramy, R. Arita, and Y. Iwasa@articleZhang2007, doi = 10.1021/nl071016r, url = https://doi.org/10.1021/nl071016r, year = 2007, month = jul, publisher = American Chemical Society (ACS), volume = 7, number = 8, pages = 2370–2376, author = Jia Zhang and Jia Mei Soon and Kian Ping Loh and Jianhua Yin and Jun Ding and Michael B. Sullivian and Ping Wu, title = Magnetic Molybdenum Disulfide Nanosheet Films, journal = Nano Letters , "Superconducting dome in a gate-tuned band insulator," *Science*, vol. 338, no. 6111, pp. 1193–1196, Nov. 2012. [Online]. Available: https://doi.org/10.1126/science.1228006 [Cited on page 31.]

[52] J. Zhang, J. M. Soon, K. P. Loh, J. Yin, J. Ding, M. B. Sullivian, and P. Wu@article2015, title=Orbital textures and charge density waves in transition metal dichalcogenides, volume=11, ISSN=1745-2481, url=http://dx.doi.org/10.1038/nphys3267, DOI=10.1038/nphys3267, number=4, journal=Nature Physics, publisher=Springer Science and Business Media LLC, author=Ritschel, T. and Trinckauf, J. and Koepernik, K. and Büchner, B. and Zimmermann, M. v. and Berger, H. and Joe,

Y. I. and Abbamonte, P. and Geck, J., year=2015, month=Mar, pages=328–331 , "Magnetic molybdenum disulfide nanosheet films," *Nano Letters*, vol. 7, no. 8, pp. 2370–2376, Jul. 2007. [Online]. Available: https://doi.org/10.1021/nl071016r [Cited on page 31.]

[53] T. Ritschel, J. Trinckauf, K. Koepernik, B. Büchner, M. v. Zimmermann, H. Berger, Y. I. Joe, P. Abbamonte, and J. Geck, "Orbital textures and charge density waves in transition metal dichalcogenides," *Nature Physics*, vol. 11, no. 4, p. 328–331, Mar 2015. [Online]. Available: http://dx.doi.org/10.1038/nphys3267 [Cited on page 31.]

[54] A. W. Tsen, R. Hovden, D. Wang, Y. D. Kim, J. Okamoto, K. A. Spoth, Y. Liu, W. Lu, Y. Sun, J. C. Hone, and et al., "Structure and control of charge density waves in two-dimensional 1t-tas2," *Proceedings of the National Academy of Sciences*, vol. 112, no. 49, p. 15054–15059, Nov 2015. [Online]. Available: http://dx.doi.org/10.1073/pnas.1512092112 [Cited on page 31.]

[55] X. Qian, J. Liu, L. Fu, and J. Li, "Quantum spin hall effect in two-dimensional transition metal dichalcogenides," *Science*, vol. 346, no. 6215, p. 1344–1347, Dec 2014. [Online]. Available: http://dx.doi.org/10.1126/science.1256815 [Cited on page 31.]

[56] M. Cazalilla, H. Ochoa, and F. Guinea, "Quantum spin hall effect in two-dimensional crystals of transition-metal dichalcogenides," *Physical Review Letters*, vol. 113, no. 7, Aug 2014. [Online]. Available: http://dx.doi.org/10.1103/PhysRevLett.113.077201 [Cited on page 31.]

[57] H. Zeng, J. Dai, W. Yao, D. Xiao, and X. Cui, "Valley polarization in MoS2 monolayers by optical pumping," *Nature Nanotechnology*, vol. 7, no. 8, pp. 490–493, Jun. 2012. [Online]. Available: https://doi.org/10.1038/nnano.2012.95 [Cited on page 31.]

[58] Y. Gong, J. Lin, X. Wang, G. Shi, S. Lei, Z. Lin, X. Zou, G. Ye, R. Vajtai, B. I. Yakobson, H. Terrones, M. Terrones, B. K. Tay, J. Lou, S. T. Pantelides, Z. Liu, W. Zhou, and P. M. Ajayan, "Vertical and in-plane heterostructures from WS2/MoS2 monolayers," *Nature Materials*, vol. 13, no. 12, pp. 1135–1142, Sep. 2014. [Online]. Available: https://doi.org/10.1038/nmat4091 [Cited on page 31.]

[59] J. C. Slater and G. F. Koster, "Simplified lcao method for the periodic potential problem," *Phys. Rev.*, vol. 94, pp. 1498–1524, Jun 1954. [Online]. Available: https://link.aps.org/doi/10.1103/PhysRev.94.1498 [Cited on page 35.]

[60] W. Harrison, *Electronic Structure and the Properties of Solids: The Physics of the Chemical Bond*, ser. Dover Books on Physics. Dover Publications, 1989. [Online]. Available: https://books.google.pt/books?id=R2VqQgAACAAJ [Cited on pages xii and 36.]

[61] J. M. B. Lopes dos Santos, N. M. R. Peres, and A. H. Castro Neto, "Continuum model of the twisted graphene bilayer," *Physical Review B*, vol. 86, no. 15, Oct 2012. [Online]. Available: http://dx.doi.org/10.1103/PhysRevB.86.155449 [Cited on pages xiv, 47, and 84.]

[62] J. Bezanson, A. Edelman, S. Karpinski, and V. B. Shah, "Julia: A fresh approach to numerical computing," *SIAM Review*, vol. 59, no. 1, pp. 65–98, 2017. [Online]. Available: https://epubs.siam.org/doi/10.1137/141000671 [Cited on page 53.]

[63] P. San-Jose, "Quantica.jl: a quantum lattice simulation library in the julia language," 2021. [Online]. Available: https://zenodo.org/record/4762964 [Cited on page 53.]

[64] "Krylovkit.jl," https://github.com/Jutho/KrylovKit.jl. [Online]. Available: https://github.com/Jutho/KrylovKit.jl [Cited on page 55.]

[65] T. Breloff, "Plots.jl," Dec. 2021. [Online]. Available: https://doi.org/10.5281/zenodo.5809248 [Cited on page 56.]

[66] M. Mucha-Kruczyński, O. Tsyplyatyev, A. Grishin, E. McCann, V. I. Fal'ko, A. Bostwick, and E. Rotenberg, "Characterization of graphene through anisotropy of constant-energy maps in angle-resolved photoemission," *Physical Review B*, vol. 77, no. 19, May 2008. [Online]. Available: https://doi.org/10.1103/physrevb.77.195403 [Cited on page 61.]

[67] J. J. Sakurai, *Modern quantum mechanics; rev. ed.* Reading, MA: Addison-Wesley, 1994. [Online]. Available: https://cds.cern.ch/record/1167961

[68] M. I. Katsnelson, *The Physics of Graphene*, 2nd ed. Cambridge University Press, 2020.

[69] S. H. Simon, *The Oxford solid state basics*. Oxford, UK: Oxford Univ. Press, 2013. [Online]. Available: https://cds.cern.ch/record/1581455

[70] A. K. Geim, "Graphene: Status and prospects," *Science*, vol. 324, no. 5934, p. 1530–1534, Jun 2009. [Online]. Available: http://dx.doi.org/10.1126/science.1158877

[71] K. Zou, F. Zhang, C. Clapp, A. H. MacDonald, and J. Zhu, "Transport studies of dual-gated ABC and ABA trilayer graphene: Band gap opening and band structure tuning in very large perpendicular electric fields," *Nano Letters*, vol. 13, no. 2, pp. 369–373, Jan. 2013. [Online]. Available: https://doi.org/10.1021/nl303375a